5-2023

Fluorescence Multiplexing with Combination Probes for Biological and Diagnostic Applications

Madeline McCarthy
memccrt@clemson.edu

FLUORESCENCE MULTIPLEXING WITH COMBINATION PROBES FOR BIOLOGICAL AND DIAGNOSTIC APPLICATIONS

A Dissertation
Presented to
the Graduate School of
Clemson University

In Partial Fulfillment
of the Requirements for the Degree
Doctor of Philosophy
Chemical Engineering

---

by
Madeline McCarthy
May 2023

Accepted by:
Dr. Marc Birtwistle, Committee Chair
Dr. Jessica Larsen
Dr. Scott Husson
Dr. Hugo Sanabria

ABSTRACT

Cancer refers to a group of diseases containing more than 200 different subtypes. Cancer is a heterogeneous disease by nature, meaning that there are differences among tumors of the same type in different patients, and there are differences among cancer cells within a single tumor of one patient. Since cancer is not a single disease, nor does it have a single cause, it proves to be incredibly hard to diagnose and treat. The ability to study cellular markers, cell and tissue spatial arrangement, and gene function are all integral parts of cancer diagnostic and treatment efforts.

Here, I first present a review of current techniques for quantitative tissue imaging at cellular resolution. I broadly divide current imaging techniques into three categories: fluorescence-based, mass spectrometry-based, and sequencing-based. In this work, I primarily concentrate on fluorescence-based methods, with the focus being on our recently developed theory Multiplexing using Spectral Imaging and Combinatorics (MuSIC). The basis for MuSIC is to create combinations of fluorescent molecules (whether it be small molecule fluorophores or fluorescent proteins) to create unique spectral signatures.

I then present a protocol for labeling antibodies with combinations of small molecule fluorophores, which I refer to as MuSIC probes. I use fluorescent oligonucleotides (oligos) to arrange the fluorophores at specified distances and orientations from one another in order to produce complex fluorescence spectra when the probe is excited. This labeling protocol is demonstrated using a 3-probe

experimental setup, bound to Protein A beads, and analyzed via spectral flow cytometry. When translating this method to staining human cells, our staining intensity was not comparable to that of a conventional antibody labeling kit. Therefore, next I present an improved method to label antibodies with MuSIC probes with increased signal intensity. I re-arrange the oligo-fluorophore arrangement of the MuSIC probe to emit an increased fluorescent signal. Then I validate this approach by comparing the staining intensity of MuSIC probe-labeled antibodies to a conventional antibody labeling kit using human peripheral blood mononuclear cells.

Lastly, I present simulation theories for the multiplexing capabilities of MuSIC probes for various biological and diagnostic applications. First, I present a theory for high-throughput genetic interaction screening using MuSIC probes generated from 18 currently available fluorescent proteins. Simulation studies based on constraints of current spectral flow cytometry equipment suggest our ability to perform genetic interaction screens at the human genome-scale. Finally, I adapt this simulation protocol to generate MuSIC probes from 30 currently available small-molecule fluorophores. Using the same constraints as before, I predict that I can perform cell-type profiling of 200+ analytes.

I hope that the work presented here provides a foundation for the use of combination probes for various biological and disease applications and ultimately help to better diagnose and treat different types of cancer.

DEDICATION

I would like to dedicate this dissertation to my best friend Luna. Thank you for all of the love and support that you've given me.

ACKNOWLEDGMENTS

I would like to first thank my parents Laura and Daniel McCarthy and my brother Alex McCarthy. I am extremely grateful for all of the love, support, and guidance that they have given me throughout this journey. I would also like to thank all my friends, that have turned into my family, here at Clemson.

Thank you to my past and current colleagues in the Birtwistle lab- Dr. Cemal Erdem, Dr. Xioaming Lu, Caitlin Anglin, Deepraj Sarmah, and Arnab Mutsuddy. Thanks to all the amazing undergraduates who have worked with me over the years. A special thank you to Charlotte Haskell and Nishi Patel who have been working with me for the entirety of my Ph.D. I have loved having the pleasure of watching you two grow as both scientists and women.

A great thanks to my advisor Dr. Marc Birtwistle for all the guidance and support that he has given me throughout this journey. I have learned so much from him these past few years and thank him for being the researcher that I am today. I will be forever grateful for his support and friendship.

A final thank you to my dissertation committee – Dr. Jessica Larsen, Dr. Scott Husson, anmd Dr. Hugo Sanabria.

TABLE OF CONTENTS

LIST OF TABLES

Table Page

LIST OF FIGURES

CHAPTER ONE

INTRODUCTION

Diagnosing and Treating Cancer

Cancer is a genetic disease that is caused by changes to genes, causing cells to grow uncontrollably[1]. There are more than 200 types of cancer[2]. Additionally, cancer is a heterogeneous disease by nature, meaning that tumors can differ between patients (inter-patient heterogeneity), between different metastatic tumors from a single patient (inter-tumor heterogeneity), and between individual cancer cells within a single tumor (intra-tumor heterogeneity)[3]. Furthermore, cancer is a dynamic disease, causing it to become more heterogenous as the disease progresses[4]. This inherent heterogeneity causes significant challenges for diagnosis and treatment[5]. Consequently, cancer is the second leading cause of death worldwide (8.97 million deaths annually)[6]. For this reason, the ability to study cell types along with cell and tissue architecture (i.e., the spatial organization of cellular and extracellular components) at a single-cell level is crucial to our understanding of the disease and ability to detect and treat it[7].

How Do We Visualize and Study Cells?

There are hundreds of different cell types containing thousands of cell markers in the human body[8]. Researchers have found many ways to study cells and cellular function. Fluorescence-based methods, including cellular imaging and

flow cytometry, involve staining the cell/tissue sample with fluorescently labeled antibodies and analyzing by collecting emission light from the sample when excited at various wavelengths[9]. Non-fluorescence-based methods include mass cytometry and single-cell sequencing. In mass cytometry, cell/tissue samples are stained with isotopically pure rare-earth metal-labeled antibodies, and the sample is ablated with a laser or ion beam to collect the composition of the sample[10]. Single-cell RNA sequencing (sc-RNA seq) can analyze the entire transcriptome of single cells in a population/tissue sample. Sc-RNA seq has been combined with spatial transcriptomics to maintain spatial information of RNA analytes, typically lost during sc-RNA seq analysis[11]. Both of these methods have been instrumental in cellular studies; however, mass cytometry and sc-RNA seq are more expensive compared to flow cytometry and require the destruction of the acquired sample, preventing the use for follow-up studies[12–141–13]. For this reason, fluorescence-based methods have become an attractive candidate for high throughput, cost-effective, and non-destructive analysis of cell/tissue samples.

What Are the Challenges with Fluorescent Multiplexing?

Central to fluorescence imaging and flow cytometry are fluorescent dyes conjugated to antibodies, which enable measurement of target analytes such as cell surface or intracellular markers[9]. Each fluorophore has a distinct excitation and emission spectra, corresponding to the range of wavelengths at which it absorbs and emits light. So, when the fluorochrome is excited, detectors and filters can be used to detect signals from the specific fluorophore. When designing fluorescent

antibody panels, it is critical to choose fluorophores with distinct excitation and emission peaks from one another in order to minimize spectral overlap. Spectral overlap occurs when fluorescence from more than one fluorochrome is detected, making it difficult to distinguish individual fluorophores (Figure 1.1). For this reason, the use of fluorescent antibodies for conventional filter-based flow cytometry is typically limited to only 4-5 fluorescent dyes that can be used simultaneously in a panel for cell staining, however up to ~10-15 have been reported, as the dyes need to have distinct emission peaks from one another[15–17]. One method that scientists have used to overcome this is using repeated rounds of 4-color staining, imaging, and bleaching, in methods such as MxIF, CyCIF, and 4i. By using rounds of staining, up to 60 analytes can be visualized per sample. However, repeated rounds of staining and bleaching become time-consuming and can lead to sample degradation over time.

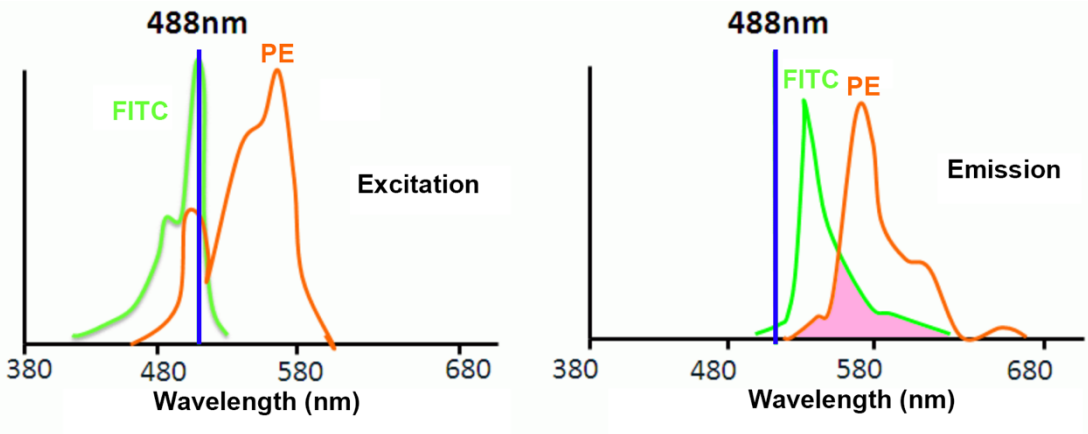

Figure 1.1. Spectral Overlap Between Two Fluorophores

Benefits of Spectral Data Collection

Recent technological advancements have led to spectral imaging/flow cytometry. Here, the entire emission spectrum of each fluorochrome is collected using a series of detectors, generating an entire spectral profile for each fluorophore, rather than only identifying the peak of emission (Figure 1.2)[18].

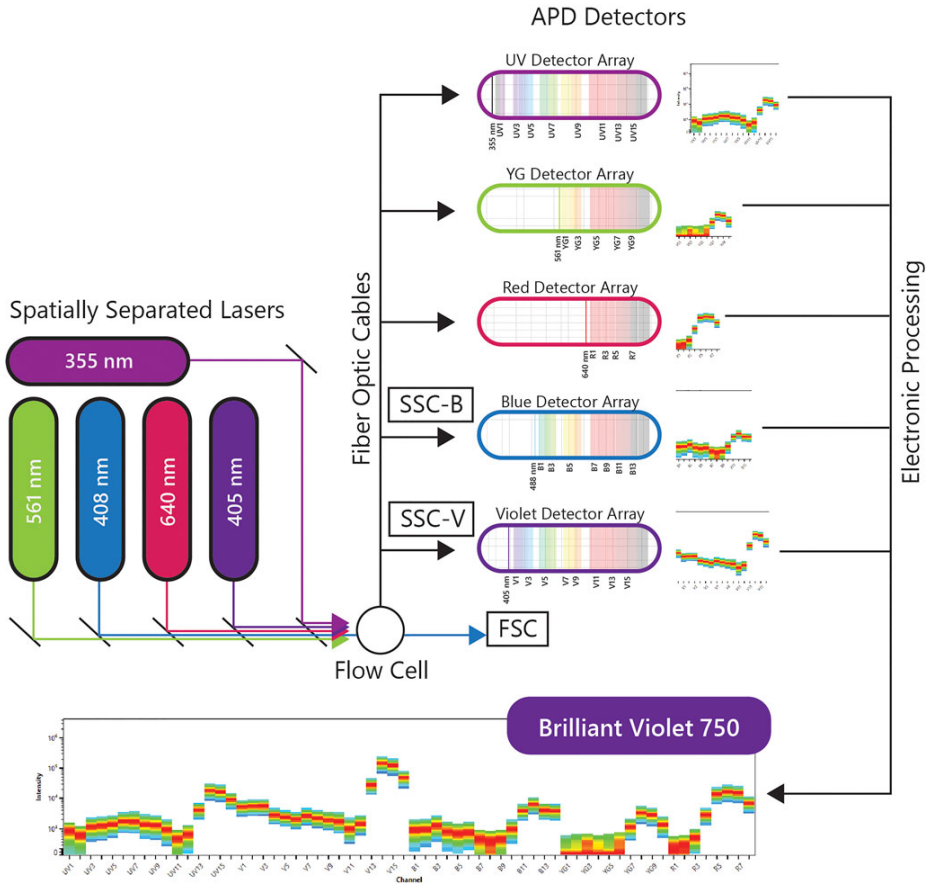

Figure 1.2. Licensed from Bonilla et. al (2021). Full Spectrum Flow Cytometry Diagram

Spectral unmixing refers to the mathematical algorithm that deconvolves the multiple fluorophore signatures within a mixture of fluorophores. This allows

the spectral signatures from each fluorophore to be used to isolate the profiles of each individual fluorophore, using spectral unmixing. This gives an advantage over traditional fluorescence imaging and flow cytometry in that, so long as there are distinct spectral signatures, fluorophores with similar peak emissions can be used in the same panel. Using full spectrum flow cytometry, fluorescent antibody panels using 40 parameters have been designed and demonstrated[19]. However, further development in this area is impeded by the number of commercially available dyes compatible in a single panel.

Combination Fluorescent Probes

To increase the number of dyes compatible for panel design, we look towards a phenomenon known as Förster resonance energy transfer (FRET). FRET occurs when a higher energy fluorophore (the donor) transfers energy to a lower energy fluorophore (the acceptor) when they are in close proximity, which produces a unique emission spectra[20]. The efficiency of FRET is directly related to the orientation of and distance between the two fluorochromes. This concept is central to our recently developed method Multiplexing using Spectral Imaging and Combinatorics (MuSIC), in which stable combinations of fluorophores are used to create MuSIC probes with unique spectral signatures using commercially available dyes[21,22]. If a fluorophore combination exhibits sufficient FRET, then mathematically, its probe levels can be estimated along with that of the single fluorophores that make up the combination. Picture a 3-probe experimental setup (m=3). The emission spectra of the mixture of fluorophores ($\boldsymbol{m}$) are arranged

vertically by emission wavelength per each excitation wavelength. Then, each column in ***R*** is the emission spectra of each individual probe, arranged the same way. When solving this matrix, the resulting output is ***f***, each component's individual probe levels (Figure 1.3)[21].

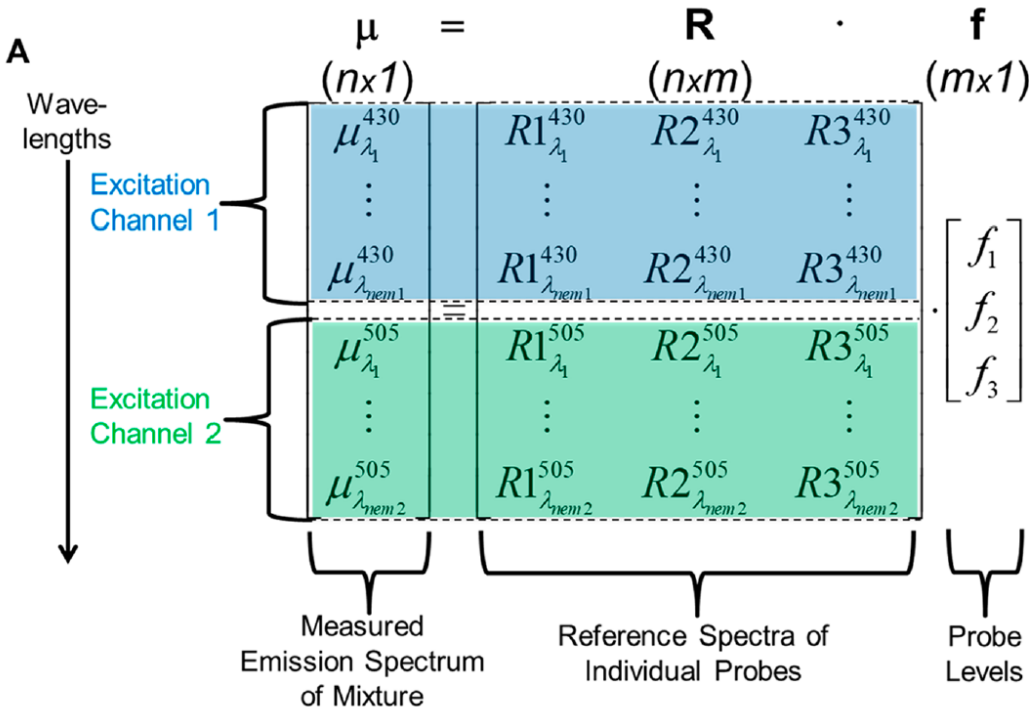

Adapted from Holzapfel et. al (2018)

Figure 1.3 Licensed from Holzapfel et. al 2018. The Mathematical Basis for MuSIC

Dissertation Overview

This dissertation explores the use of combination fluorescent probes for a variety of biological and diagnostic applications. Specifically, we explore the use of combination (or MuSIC) probes for spectral imaging and spectral flow cytometry.

Potential applications for MuSIC probes include cell/tissue imaging, cell-type profiling, and genetic and genetic interaction screenings.

In chapter two, we begin by reviewing cell and tissue imaging methods at a cellular resolution. Tissue imaging can be broadly divided into three categories; fluorescence-based, mass spectrometry-based, and sequencing-based. Furthermore, we look into various methods available for data analysis.

Chapter three introduces a protocol for labeling antibodies with MuSIC probes. Using an oligo-based approach, we show our ability to stably bind combinations of fluorophores to antibodies and validate this using spin column purifications and absorbance measurements. We then create a panel of three probes and demonstrate our ability to unmix these probes using spectral flow cytometry.

In chapter four, we build upon the labeling strategy presented in chapter three to translate this method into staining human cells. Upon testing the labeling strategy described in chapter three by staining human peripheral blood mononuclear cells (PBMCs), we found a significantly lower fluorescent signal of our probes than cells stained with conventionally-labeled fluorescent antibodies. By changing the design of our probes and re-arranging the oligo-fluorophore configuration, we demonstrate our ability to stain human PBMCs at a signal intensity above that of the conventionally-labeled fluorescent antibodies.

In chapter five, we introduce a theory for high-throughput genetic interaction screening. Using our simulation workflow, we generate lists of MuSIC probes that

we predict can be accurately demultiplexed in a mixture together based on binary classification patterns. If these MuSIC probes can be paired with guide RNAs, we predict we can perform genetic interaction screens at the genome level.

In chapter six, we build upon the simulation workflow presented in chapter five and the labeling strategies presented in chapters two and three to propose a method for determining lists of MuSIC probes using small molecule fluorophores that can be accurately demultiplexed in a mixture for antibody labels. We predict that using 30 currently available small molecule fluorophores, we can create fluorescent antibody panels for over 200 markers using currently available spectral equipment.

In chapter seven, we discuss the broad conclusions of this work and propose future directions of the ideas presented in this dissertation. Experimental testing of the simulation study presented in chapter six, using the labeling techniques described in chapters three and four, will lead to the establishment of a full panel of demultiplexable MuSIC probes for fluorescence-based biological and disease diagnostics.

CHAPTER TWO

HIGHLY-MULTIPLEXED, QUANTITATIVE TISSUE IMAGING AT CELLULAR RESOLUTION

Abstract

There is a contemporary push to map tissues and their disease states quantitatively at single-cell and spatial resolution, but standard assays to do so, such as immunohistochemistry, have been historically lowly multiplexed (2-4 measurements). This push has driven the development of several new multiplexed techniques for quantitative tissue imaging, which we review here. Standard multiplexed imaging is primarily limited by fluorophore spectral overlap. Innovations increasing multiplexing capacity include iterative cycles of staining / bleaching / imaging, imaging mass spectrometry with metal-conjugated antibodies, leveraging fluorophore combinatorics, and coupling to sequencing-based methods. Recent progress has increased image-based multiplexing roughly 10-fold, and in some cases of nucleic acid analytes, to genome-scale. This has given unprecedented biological and disease knowledge, but there is still substantial work to achieve genome-scale across all types of analytes, as well as spatial scales greater than ~millimeters. Concomitantly, challenges in data storage, retrieval and analysis will need to be solved moving forward.

Introduction

Human tissues consist of complex networks of interacting cells [23] [24] [25] [26]. The architecture of a tissue, and to a large extent function, is defined by spatial organization of its cellular and extracellular compartments [27] [28] [29]. The architecture of normal and diseased tissues influences the development of a disease as well as receptiveness and resistance to therapy [30] [31]. The ability to characterize and gain further understanding of tissue architecture through imaging has driven progress in biology and pathology [32] [33] [34] [35]. Immunohistochemistry (IHC) is a conventional tool used in clinical diagnostics and research laboratories to assess the spatial distribution of typically two to four analytes in a single sample [36] [37] [38] [39] [40] [41] . However, IHC has a variety of limitations, such as the requirement of a new sample or serial section for each analyte set, which limits multiplexing, and non-linear relationships between analyte abundance and staining intensity (when fluorescence is not used), which limits quantification [42] [43]. Other methods exist which are highly multiplexed and provide quantitative data, such as deep sequencing, or even single-cell sequencing [44]. However, they have the limitation that spatial information in a tissue is often lost [45]. There is currently a large technological gap for methods that are image-based but offer more quantitative multiplexing at single-cell spatial resolution [42].

There are a variety of biological and disease applications for multiplexed tissue imaging; one example is cancer [42]. The NIH-funded Human Tumor Atlas Network was established to, in part, complement the tremendous efforts of The Cancer Genome Atlas with spatial information [46]. Tumor heterogeneity is multi-

dimensional including variation in driver mutation profiles across space, extracellular matrix structure, soluble factor and oxygen gradients, as well as multiple important cell types such as immune infiltrates and tumor-associated fibroblasts that interact with tumor cells to influence tumor microenvironment [47] [48] [49] [50] [51] [52]. This inherent tumor heterogeneity makes diagnosis, prognosis, and treatment a challenge because of its unknown impact on the tumor's evolution and drug sensitivity profile [47] [53] [54] [55]. More highly-multiplexed imaging tools and techniques will facilitate characterizing and better understanding tumor heterogeneity, helping to inform diagnosis, prognosis, and treatment.

In this review, we survey recent advances in image-based multiplexing technologies capable of single-cell spatial resolution, with focus as well on their quantitative features to some extent. Although major advances have been made with radiological methods including PET, CT and MRI, we focus this review on techniques with higher spatial resolution, and rather refer the reader to other resources on such topics [56] [57] [58]. These technologies can generally be divided into three categories: fluorescence-based, mass spectrometry-based, and very recently sequencing-based, which we enumerate below and are summarized in Table 2.1 and Figure 2.1. These advances in imaging techniques have enabled the analysis of significantly more parameters in cells and tissues than what was previously possible, enabling significant progress towards deeply characterizing the tumor microenvironment and other tissue or spatial analyses—a new grand challenge of biology for the 21st century post-genomic era.

Table 2.1 Specifications of available highly multiplexed imaging methods. Important aspects of each method are described, such as differences in degree of multiplexing, assay duration, major equipment, and major reagents. TOF: time of flight, FISH: fluorescence in situ hybridization, H&E: haemotoxylin and eosin.

		Principle of operation	Spatial resolution	Number of simultaneous measurements	Compatible assays	Assay duration
Fluorescence-based methods	Multiplexed fluorescence microscopy (MxIF)	Low-plex fluorescence images repeatedly collected using cycles of staining/bleaching/imaging	~200 nm	Up to 60 analyte/section	DNA FISH	2.5 h/cycle
	Iterative indirect immunofluorescence imaging (4i)	Low-plex fluorescence images repeatedly collected using cycles of staining/bleaching/imaging	~200 nm	~40 analytes/section	Not noted	Not reported
	Cyclic immunofluorescence (CycIF)	Low-plex fluorescence images repeatedly collected using cycles of staining/bleaching/imaging	~200 nm	~60 analytes/section	Super-resolution imaging, H&E	~24 h/cycle
	Co-detection by indexing (CODEX)	Uses DNA-conjugated antibodies as barcodes for fluorescence imaging multiplexing	~200 nm (fluorescence)	66/section	None noted	3.5 h/30 antibodies
	Super-resolution barcoding	Individual mRNAs are spatially resolved in diffraction-limited spots and identified with unique fluorophore barcodes	~5 nm	Up to ~30,000 mRNAs/section	Light sheet/selective plane illumination microscopy (SPIM)	Not reported
	Hyper-spectral fluorescence imaging	Measures fluorescence emission spectra in each pixel to allow linear unmixing of fluorophores with overlapping spectra	~200 nm	7 analyte/section	Fluorescence based modalities	Not Reported
	Multiplexing with spectral imaging and combinatorics (MuSIC)	Creates new independent probes from covalently linked combinations of individual fluorophores which are deconvolved through spectral imaging and linear unmixing	~200 nm	9 in restricted wavelength range, in principle ~30/section	Fluorescence based modalities	Not yet tested
	Spectrally resolved fluorescence lifetime imaging microscopy (sFLIM)	Combines spectral and fluorescence lifetime signatures to estimate fluorophore ratios in mixtures	~200 nm	9/section	None noted	Not reported
Mass spectrometry methods	Imaging mass cytometry	Metal-conjugated antibody levels are detected through mass spectrometry, and there is minimal overlap in mass-to-charge spectra between selected metals	~1000 nm	32/section	None noted	14 h/mm^2
	Multiplexed ion beam imaging (MIBI)	Metal-conjugated antibody levels are detected through mass spectrometry, and there is minimal overlap in mass-to-charge spectra between selected metals	~200 nm	40 experimentally demonstrated; ~7/cycle; up to 100 total	None noted	8 h per mm^2
Sequencing-based methods	Slide-seq	DNA-barcoded beads on a glass coverslip spatially capture mRNA from tissue	~10 μm	Transcriptome	None noted	~Days

	Quantitative?	Compatible with FFPE?	Major equipment	Major reagents	References
Fluorescence-based methods	Yes	Yes	Proprietary microscope	Fluorophore-conjugated primary antibodies; proprietary bleaches	Gerdes et al. [37•], McKinley et al. 2017
	Yes	No	Fluorescence microscope with the ability to remount samples multiple times (i.e., adequate *x-y* position recall)	Unconjugated primary and fluorophore-conjugated secondary antibodies	Gut et al. [38]
	Yes	Yes	Fluorescence microscope with the ability to remount samples multiple times (i.e., adequate *x-y* position recall)	Fluorophore-conjugated primary antibodies	Lin et al. [39], Lin et al. [40••]
	Yes	Yes	Fluorescence microscope	DNA-barcoded antibodies	Goltsev et al. [41••]
	Yes	No	Super-resolution microscope	Standard super-resolution imaging buffers; fluorophore-labeled oligo probes	Cai 2012, Lubeck and Cai [42], Cai, 2019
	Yes	Yes	Imaging spectrometer	Fluorophore-conjugated antibodies	Tsurui et al. [43•], Haraguchi et al. [44], Leavesley et al. 2011, Lu and Fei [45]
	Yes	Yes, in principle, but not yet evaluated	Imaging spectrometer	Fluorophore-conjugated primary antibodies	Holzapfel et al. [46••]
	Yes	Not reported	Microscope with time-resolved fluorescence lifetime and spectral imaging capabilities	Fluorophore-conjugated antibodies	(Niehörster et al. [47])
Mass spectrometry methods	Yes	Yes	Inductively coupled plasma mass spectrometry instrument and laser ablation system	Metal-conjugated antibodies	Giesen et al. [48•], Chang et al. 2017, Bodenmiller 2016
	Yes	Yes	Mass spectrometer and an O- primary ion beam for ablation	Metal-conjugated antibodies	Angelo et al. [49], Bodenmiller [50]
Sequencing-based methods	Yes	Not reported	SOLiD sequencing (and Illumina but that is more standard)	SOLiD reagents/beads for mRNA capture	Rodriques et al. [51••]

TOF time of flight

FISH fluorescence in situ hybridization

H&E hemotoxylin and eosin

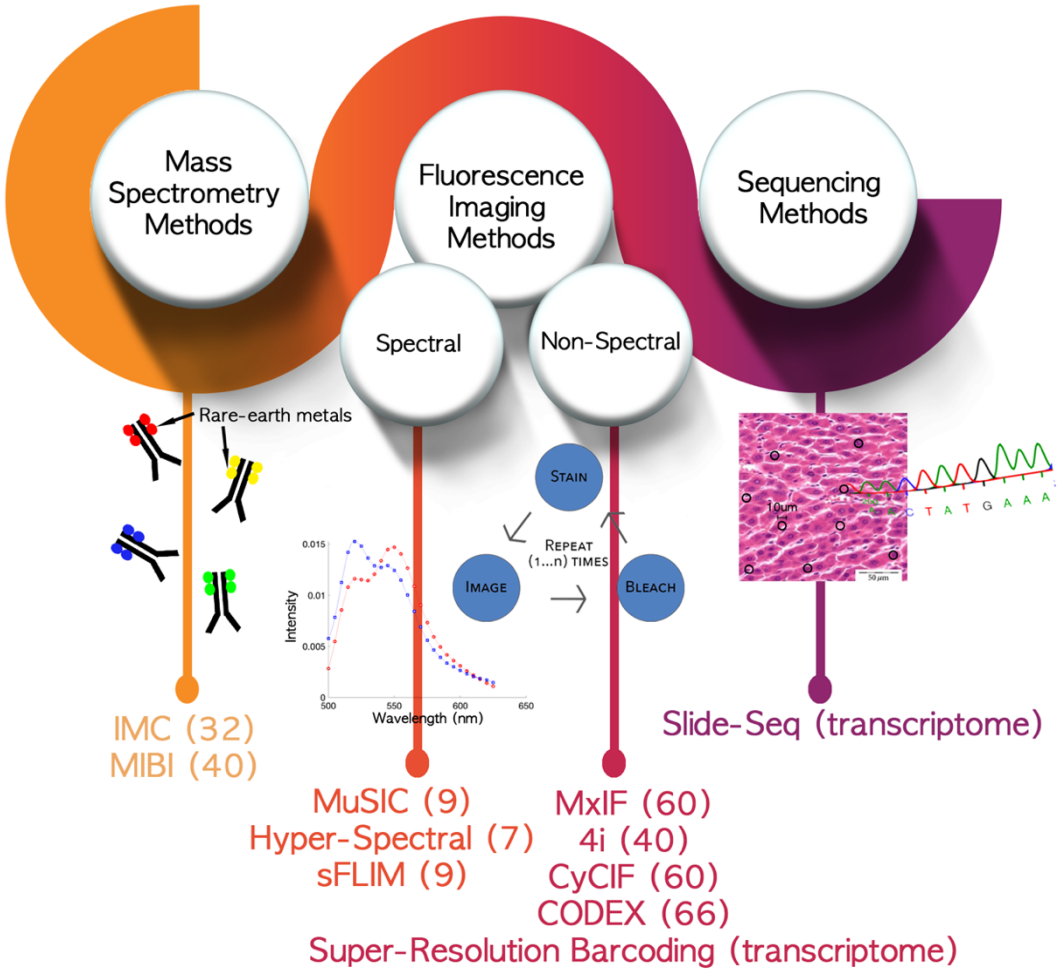

Figure 2.1 Schematic of available highly multiplexed imaging methods. The current highly multiplexed imaging techniques can be grouped into three general categories: mass spectrometry based, fluorescence based, and sequencing based. Rare earth metals attached to antibodies are depicted for mass spectrometry. The fluorescence imaging methods can be further divided into spectral and non-spectral subcategories. Fluorescence intensity data of two fluorophores exhibiting FRET are depicted for spectral and the general procedure for cycles of non-spectral fluorescence imaging are depicted for non-spectral

fluorescence imaging. Sequencing data for a given tissue sample is shown for sequencing methods. The methods are further described in the text. [124].

Fluorescence-Based Methods

Central to fluorescence microscopy are fluorescent dyes attached to affinity binders, such as antibodies or oligonucleotides, which then associate with a targeted analyte, such as proteins, RNA or DNA, allowing visualization and analysis [59]. Fluorescence-based methods can be divided into filter-based and spectral techniques. Filter-based fluorescence imaging uses optical films that allow relatively broad wavelength ranges of light to excite fluorophores in samples and the subsequent emission light to pass onto a detector, but multiplexing is limited usually to about four colors by inevitable spectral overlap. Spectral overlap occurs when fluorophore's excitation and/or emission spectra share substantial wavelength ranges, such that filters cannot efficiently separate them. Spectral (also called hyper-spectral) imaging partially overcomes this issue of overlap because much finer wavelength resolution for fluorescence emission is obtained [60] [61], by using, for example, monochromators, prisms and/or diode arrays [62]. Currently, filter-based methods are the predominant modality because of simplicity and cost.

There are currently a wide variety of different reporter agents available for these techniques. A few examples of these include small molecule, [63] [64] [65],fluorescent proteins, [66] [67] [68], photo-switchable [69] [70] [71], quantum dots [72] [73] [74], polymer dots [75] [76], and endogenous fluorescence [77] [78] [79].

Filter-based

Filter-based fluorescence imaging is the most widely used method for visualizing cells and tissues. There are a variety of established textbook protocols (e.g. [80] [81]), and the required equipment is generally cheaper and more readily available than that for the methods that will be later described.

One way to achieve higher multiplexing is to simply perform repeated rounds of staining and imaging, with bleaching of fluorophores between rounds. Several recent techniques leverage this principle, including multiplexed fluorescence microscopy (MxIF) [82], iterative indirect immunofluorescence imaging (4i) [83], cyclic immunofluorescence (CycIF) [84] [85] and co-detection by indexing (CODEX) [86]. These methods are in principle compatible with formalin fixed paraffin embedded (FFPE) tissue, a common format for preserving samples. They are limited by sample degradation across and the duration of each cycle .

MxIF measures up to 60 analytes in a single FFPE tissue section using fluorophore-conjugated primary antibodies [87]. The MxIF procedure consists of acquiring background autofluorescence, staining with four colors (one typically DAPI for nucleus fiduciary in each round), acquiring immunofluorescence, dye inactivation using alkaline oxidation chemistry, acquiring new background autofluorescence, re-staining with new fluorescent dye-conjugated primary antibodies, and acquiring new images [82]. The cycle is repeated until all target analytes are measured. This technique was used to examine colorectal cancer specimens and allowed the mapping of cellular mechanistic target of rapamycin

complex 1 (mTORCI) and MAPK signal transduction patterns in tissues [82], as well as in other applications [87] [88].

CycIF assembles up to 60-plex images of tissue sections via successive rounds of four-channel imaging [89], similarly to MxIF. Cycles involve four steps: immunostaining with fluorophore-conjugated primary antibodies, staining with a DNA dye to mark nuclei and facilitate image registration across cycles, four-channel imaging at low- and high-magnification, fluorophore bleaching (oxidation in a high pH hydrogen peroxide solution in the presence of light) followed by a wash step, and then subsequent rounds of staining [84], [85]. CycIF is partly limited by the assay duration as each cycle takes roughly 24 hours to complete, but also by sample degradation similar to MxIF [89] [84]. A major difference between CycIF and MxIF is that MxIF requires more expensive reagents and equipment, but has a shorter assay duration [90].

The 4i method can detect up to 40 analytes [83]. So-called “indirect immunofluorescence” uses an unconjugated primary antibody and a fluorophore-conjugated secondary antibody, rather than a single primary antibody directly conjugated to the fluorophore, resulting in compatibility with “off-the-shelf” antibodies. This is the main distinctive feature of 4i. The 4i technique has been used to create multiplexed protein maps in different phases of the cell cycle, in response to cell crowding, inhibitors, and different growth conditions [91].

CODEX has visualized up to 66 DNA-conjugated antibodies in a single image [86]. The barcode information is encoded by an overhang sequence on the

DNA duplex that is read off in cycles of two-color imaging. Thus, 66 antibodies need 33 rounds of imaging. Overhang lengths on each antibody can be as small as two (1 color code) or as large as feasible for the experiment time scale and sample degradation of cycling. Two types of “walking” nucleotides (G and A) are used to traverse the overhang, and then other two (U and T) are labeled with either Cy3 or Cy5, respectively. First, a reaction mixture leaving out A is incubated on the antibody-stained sample. Only overhangs with C as the first base in its sequence are capable of incorporating a fluorescently labeled nucleotide, and then, CG would get a Cy3 label, and CA would get a Cy5 label. Other overhangs with a CT sequence do not yet receive a color. Next, a reaction mixture leaving out G is incubated on the sample. Then, CTG would get a Cy3 label, and CTA would get a Cy5 label. Other overhangs with a CTC sequence do not yet receive a color. This strategy is repeated for multiple rounds of extension on the overhang to perform the multiplexed imaging. Thus, the barcode is then the combination of the round in which a signal was detected, plus whether the color was Cy3 or Cy5. CODEX was used to determine that significant changes in expression levels in certain markers, such as B220, CD79b, or CD27 are dependent on the tissue microenvironment in which the cells reside [86]. This drove the conclusion that cell populations that are currently thought of as broadly expressing a certain marker are actually comprised of multiple sub phenotypes that correlate with the indexed niche identity [86].

There are also non-spectral techniques that do not involve cycles of imaging, but rather use super-resolution microscopy and combinatorial labeling [92].

This method has many similarities to standard fluorescence in situ hybridization (FISH) involving fluorophore-conjugated oligonucleotide probes complementary to mRNA targets [93] [94] [95]. However, because in super-resolution microscopy, which drives beyond the diffraction limit, each mRNA molecule can be spatially resolved in a single pixel (or voxel) and can hybridize to several different color probes, the potential combination of fluorophores in each pixel (or voxel) can be used to multiplex mRNA measurements. Simple counting of spots with matched fluorophore combination barcodes is the quantitative readout. In proof-of-principle studies, three color barcodes with seven fluorophores were used to profile transcripts from 32 stress-responsive genes in single *S. cerevisiae* cells. Thus, a transcript is defined by a combination of 3 colors from 7 choices. The results were confirmed to match to that expected from more conventional readouts [96] [92].

In a recent follow-up, this approach was scaled transcriptome wide (~35,000 transcripts / cell), in a technique called seqFISH+, which combines the super-resolution notion with the repeated rounds of imaging principal from above [97]. Here, the innovation was switching from transcripts having real color barcodes to having “pseudo-color” barcodes. Now, each transcript is only labeled with a single color fluorophore, but is assigned a pseudo-color (1 to 20) based on when this fluorescence signal is observed over 20 sequential rounds of hybridization. This has the added benefit of having only 1/20th of the transcripts in the cell showing a signal in a particular image. Then, these 20 sequential rounds of imaging are repeated 4 separate times in an “outer loop” of barcoding rounds. In

barcoding rounds, the hybridization round where a fluorescence signal appears (1 to 20) can be different for each gene, giving rise to a possible number of permutations on par with the genome.

Another non-spectral technique that does not involves cycles of imaging is fluorescence lifetime imaging microscopy (FLIM). FLIM works by determining the lifetime of the excited state in order to characterize the molecular species [98]. This is used to characterize the environment of the fluorophore [98]. Within FLIM there are two distinct methods; the time-domain method and frequency-domain method [99 100]. Time-domain FLIM works by collecting the decay at each pixel and excitation and intensity are plotted against time for each pixel. This is then fit to an exponential curve to determine the fluorescence lifetime [100 101]. Frequency-domain FLIM operates by taking measurements at different excitation frequencies and determining the phase and amplitudes at the different frequencies. The data is then fit to exponential models and analyzed [102]. These two complementary methods have their own advantages and disadvantages. Time-domain FLIM has a higher sensitivity for measurements with low fluorescence with a single-photon timing technique, whereas frequency domain FLIM is generally faster and electronics are simpler [99 102].

Sample quality becomes increasingly important with cycles of imaging and can become a major limiting factors for these methods. The extent of sample degradation can vary between tissue type and within a single tissue type [85]. For CyCIF, it was found that half of the tissue samples tested could be routinely

imaged up to 15 cycles with 20% loss of cells [85]. Further testing of the effect on different types of tissues in response to the number of cycles can be seen in figure 4E from Lin et. al (2018) [85].

Spectral

Spectral imaging acquires much finer emission wavelength information than non-spectral imaging, which allows one to quantify mixtures of fluorophores with potentially heavily overlapping spectra. Similar to filter-based techniques, spectral imaging might also be performed using multiple rounds of labeling, although this has not yet been described to our knowledge. However, it is currently less popular than non-spectral imaging because the equipment is more expensive, and the technique is less established and therefore more difficult.

Spectral imaging techniques are largely called hyper-spectral, and have been used to image up to seven analytes simultaneously in tissues [103 61 104 105 106], and even live cells [107]. Analysis is broadly called linear unmixing, which applies the principle of additivity of fluorescence emission spectra to cast a linear algebra problem, which when solved gives the levels of the individual fluorophores in each pixel. Multiple fluorophores from ultraviolet to infrared are used with (typically) three (or more) excitation channels. Design of spectral imaging experiments is more complex than filter-based, but there are metrics that can be used to help, such as the Figure of Merit (FoM) [108]. The FoM indicates how well a given imaging protocol performs for a set of fluorophores, relative to the case that these

fluorophores are present singularly and that their fluorescence can be measured noiselessly [108]. Many modern and widely available confocal microscopes also have an ability to perform emission spectral scans. Hyper-spectral fluorescence imaging has a variety of medical applications, including disease diagnosis and image-guided surgery [61]. Although not tissue imaging, also of note are recent flow cytometers that can perform spectral imaging, such as Cytek Aurora [109].

Fluorescence multiplexing using spectral imaging and combinatorics (MuSIC) builds on spectral imaging but uses single or covalent combinations of existing fluorophores to significantly increase the number of multiplexed analytes [110]. If a fluorophore covalent combination probe exhibits significant Förster resonance energy transfer (FRET), then mathematically, adding this probe to the linear unmixing problem is “well-posed” and its levels can be estimated along with the single fluorophores that make up the combination. Multiplexing up to 9 such MuSIC probes was demonstrated in solution-based assays over a restricted excitation wavelength window (~1/4 of that available), and it has the potential to scale to ~30 analytes [110]. MuSIC is compatible with the bleach-and-restain ideas from above, so multiplexing is potentially multiplicative when combining the two ideas. Moreover, because it has been shown to be compatible with fluorescent proteins, it is in principle compatible live cells or tissues.

Another method for spectral imaging is spectrally resolved fluorescence lifetime imaging microscopy (sFLIM). sFLIM is capable of multi-target fluorescence imaging through confocal sample scanning with pulsed excitations at 485nm,

532nm, and 640nm and time-correlated single-photon counting (TCSPC) on 32 spectrally separated detection channels [111]. Similar to MuSIC, a pattern-matching algorithm is used to determine the individual contribution from each fluorophore to the overall multidimensional fluorescence signal. The algorithm is based on reference patterns of fluorescence decay and spectral signatures from various cell samples that are labeled with different fluorescent probes. First the sample is excited by the three lasers (485nm, 532nm, and 640nm) then the fluorescent light is split into 32 channels, where the spectral information is recorded. The spectral information is then analyzed by TCSPC. sFLIM has been used to visualize nine different target molecules simultaneously in mouse C2C12 cells [111].

Mass Spectrometry-Based Methods

In addition to fluorescence, there are also highly multiplexed mass spectrometry methods for tissue imaging. Here, cells are typically stained with metal-conjugated antibodies, whose levels then can be quantified with mass spectrometry [112]. It is easier to multiplex using mass spectrometry as compared to fluorescence imaging because there is negligible spectral overlap. Signal-to-noise is also improved because employed metals are essentially non-existent in tissues. However, the specialized mass spectrometry equipment (and to some extent reagents) that interfaces with imaging is significantly more expensive and not as widely available.

Current mass spectrometry methods include imaging mass cytometry (IMC) [113] and multiplexed ion beam imaging (MIBI) [112], both of which multiplex using a panel of primary antibodies conjugated with isotopically-pure, rare-earth elements (e.g. lanthanides) [113]. Metals are conjugated to antibodies via a polymeric metal-chelating linker that is covalently linked to antibodies, or with metal nanoparticles [114]. In IMC, once a tissue sample has been stained with the metal-conjugated antibodies, it is dried and then positioned in a laser ablation chamber [113]. The tissue is then ablated spot by spot and line by line, which sends material via a mixed argon and helium stream to a CyTOF mass cytometer [113]. This method is capable of 32 simultaneous measurements [115]. IMC has been used to assess the immune microenvironment in breast cancer tissue, leading to the hypothesis that trastuzumab-treated patients with high tumor-infiltrating lymphocyte levels have

improved outcomes [116]. MIBI is similar to IMC, but uses an ion beam ablation (rather than a laser), and thus has slightly different mass spectrometry requirements [112] [115]. Biological specimens are immobilized on a conductive substrate, stained with metal-conjugated antibodies, dried, and loaded under vacuum for MIBI analysis [112]. This method has been used to image 40 analytes simultaneously in breast tumor tissue sections, but is potentially capable of up to 100 [112] [117].

Sequencing-Based Methods

So far, highly multiplexed sequencing methods that have transformed genomics, transcriptomics, and epigenomics have not been highly compatible with imaging. However, a recent technological advancement called Slide-seq has enabled the transfer of RNA from tissue sections onto a surface packed with DNA-barcoded beads at specified positions, allowing the spatial analysis of gene expression in a tissue at ~10 um resolution [118]. This method first involves packing of the DNA-barcoded beads on to a rubber-coated glass coverslip, called the "puck". This is followed by oligonucleotide ligation and detection (SOLiD) sequencing to determine each bead's distinct sequence and x-y location [118]. A tissue section is placed on the "puck" and mRNA from the tissue is captured by the beads with minimal lateral x-y diffusion. After capture, the bead / tissue section combination is homogenized and prepared for mRNA sequencing (via more standard Illumina-based methods), which subsequently allows relating transcriptomes to spatial locations. Using Slide-seq, it was determined that cell proliferation occurs in the first few days after a traumatic brain injury and then transitions to differentiation in the following weeks [118]. The main costs associated with this method seem to be related to the price of the pucks. As the price of these "pucks" and the associated sequencing drop, there is potential to be able to apply this method to entire organs or even entire organisms [118]. One could similarly envision coupling other nucleic acid-based conjugate technologies to enable Slide-seq on analytes other than mRNAs.

Data Analysis

Multiplexed image data are powerful but also come with several data handling, visualization, and analysis challenges, which are just beginning to be explored. Some of these techniques include viSNE , which is used for dimensionality reduction [119], multi-omics heterogeneity analysis (MOHA), which is used for image processing and visualization [47], open microscopy environment remote objects (OMERO) servers, which are used for data handling, and multiplex image cytometry analysis (miCAT / histoCAT) , which is for data handling and analysis [120] [121]. viSNE is a technique that allows visualization of high-dimensional single-cell data on a two-dimensional map and is based on the now widespread t-distributed stochastic neighbor embedding (t-SNE) algorithm [119] [122]. In this method, each cell is represented as a point in high-dimensional analyte space, with each dimension being measurement of one analyte [119]. An optimization algorithm searches for a projection of the points from the high-dimensional space into two or three dimensions to the extent that pairwise distances (e.g. Euclidian) between two points (cells) are best conserved between the high- and low-dimensional space [119]. Coupled with mass cytometry, viSNE was used to compare leukemia diagnosis and relapse samples [119]. This method could also be applied to IMC or MIBI but requires additional image analysis steps to obtain single-cell data.

The MOHA tool computes tissue heterogeneity metrics from multiplexed image data by combining single-cell molecular summary measures with pre-existing knowledge of biological pathways to assign states to cells in the tissue [47].

This is followed by using positional cell information to compute spatial cell state distributions, and importantly, correlations between neighboring cell types. It then computes tissue heterogeneity and diversity measures of the cells from the observed distributions of these molecular and spatially defined states [47]. This technique was used to identify statistically significant correlations between the intratumoral AKT pathway state diversity and cancer stage and histological tumor grade [47].

OMERO is a flexible software platform that provides a structured storage format for a range of biological data, including images [123]. It is used to provide storage access, processing and visualization without downloading entire datasets [123]. OMERO has been used in a variety of applications, including CycIF [85].

miCAT and histoCAT are analyses platforms that are used for quantitative and comprehensive visualization of cell phenotypes, cell interactions, microenvironments, and tissue structures [121] [120]. They are coupled with IMC to investigate cellular phenotypes and microenvironments of human breast cancer, allowing insight into the network structure of cell neighborhood interactions [121] [120].

Conclusion

The methods described here have increased our ability to quantitatively understand the interactions between different biological components in tissues and the regulatory networks in single cells, but importantly, retaining information on how it was arranged spatially. This has and will continue to transform our ability to understand biology and disease. Although multiplexed tissue-imaging has come a long way in the past decade, there remains much work to be done to go from the currently possible dozens of measurements to the proteome scale, especially with post-translational modifications. Very recent methods have begun to approach this scale for the transcriptome. The possibility of combining methods described here could multiplicatively increase the amount of quantitative information that can be obtained. For example, CycIF might be combined with super-resolution imaging, and/or with MuSIC-based approaches to increase the potential number of simultaneous measurements. Moreover, it is not only multiplexing that needs to improve further. Currently, covering more than ~millimeter length scales comprehensively is extremely challenging other than by brute force with time and money; innovation here is also needed to truly multiplex tissue imaging, where important changes happen over centimeter (and greater) scales. Tissue clearing techniques will likely play a large role here [25]. We expect yet still much innovation in these directions in the next several years towards the genome-scale, whole tissue or even whole-body quantitative, single-cell imaging end goal.

Acknowledgements

MRB acknowledges funding from Clemson University and the NIH Grant R21CA196418. We also thank Stephanie Klaubert for discussions and Chloe Worthy and Althea Henderson for figure creation.

CHAPTER THREE

PROTOCOL FOR LABELING ANTIBODIES WITH COMPLEX FLUORESCENCE SPECTRA

Abstract

Fluorescent antibodies are a workhorse of biomedical science, but fluorescence multiplexing has been notoriously difficult due to spectral overlap between fluorophores. We recently established proof-of-principal for fluorescence Multiplexing using Spectral Imaging and Combinatorics (MuSIC), which uses combinations of existing fluorophores to create unique spectral signatures for increased multiplexing. However, a method for labeling antibodies with MuSIC probes has not yet been developed. Here, we present a method for labeling antibodies with MuSIC probes. We conjugate a DBCO-Peg5-NHS ester linker to antibodies, a single stranded DNA "docking strand" to the linker, and finally, hybridize two MuSIC-compatible, fluorescently-labeled oligos to the docking strand. We validate the labeling protocol with spin-column purification and absorbance measurements. We demonstrate the approach using (i) Cy3, (ii) Tex615, and (iii) a Cy3-Tex615 combination as three different MuSIC probes attached to three separate batches of antibodies. We created single, double, and triple positive beads that are analogous to single cells by incubating MuSIC probe-labeled antibodies with protein A beads. Spectral flow cytometry experiments

demonstrate that each MuSIC probe can be uniquely distinguished, and the fraction of beads in a mixture with different staining patterns are accurately inferred. The approach is general and might be more broadly applied to cell type profiling or tissue heterogeneity studies in clinical, biomedical, and drug discovery research.

Introduction

Ultraviolet-to-infrared fluorescence is a bedrock of experimental science, particularly the biomedical sciences. However, multiplexing—the simultaneous analysis of multiple fluorophores in a single sample, is severely limited by spectral overlap[125–128], where excitation and/or emission spectra of fluorescent probes share broad wavelength domains. Spectral overlap limits most standard fluorescence assays to 2-4 readouts at a time. Yet, many applications would benefit from increased fluorescence multiplexing capabilities; one example is cancer. Tumor heterogeneity is multi-dimensional, including spatial variation in cell type, driver mutation profiles, protein expression, and oxygen/metabolic gradients[129–134]. As a result, there are hundreds of markers that have an impact on a tumor's evolution, fitness, and drug sensitivity [5,129,135].

Current sequencing methods can reach high levels of multiplexing and have been used in cancer diagnosis and prognosis[136–138]. Yet, the now somewhat standard biopsy- or homogenized tissue-based deep DNA or mRNA sequencing, and now increasingly single-cell sequencing[139–141], largely do not allow for spatial resolution. However, some recent sequencing-based methods can provide spatial *in situ* data[142–145]. Sequential fluorescence in situ hybridization (seqFISH+) is capable of transcriptome-wide imaging in single cells but has challenges in scaling to large numbers of cells or large areas of tissue sections. Slide-seq, alternatively, made mRNA sequencing compatible with tissue section imaging over large spatial scales with ~10 um resolution[146]. Although powerful advances, such sequencing

methods cannot yet fully capture the heterogeneity of tissue samples, which includes single and subcellular resolution and molecules other than mRNA (i.e., DNA, proteins, post-translational modifications, etc.). On the other hand, antibody-based imaging can access multiple molecule types at single and subcellular resolution while also spanning physiologically relevant length scales. Therefore, increased antibody multiplexing capabilities remain highly complementary to these sequencing-based methods.

There have been many recent advances for increased antibody-based multiplexing with single cell and subcellular spatial resolution, most of which use standard "filter-based" instrumentation that robustly allow imaging 2-4 fluorescence colors simultaneously. A widely adopted strategy is repeated rounds of staining, imaging, and bleaching of fluorophores[147–150]. By performing multiple cycles of 2-4 color imaging, these methods drastically increase fluorescent multiplexing capabilities (up to 60 analytes). Multiplexed fluorescence microscopy (MxIF) was the first but requires proprietary and expensive equipment / reagents[147]. Cyclic Immunofluorescence (CyCIF) is similar in principle but uses inexpensive reagents and standard equipment[149,151]. Similar to MxIF and CyCIF, Iterative indirect immunofluorescence imaging (4i) uses cycles of imaging but leverages fluorophore-conjugated secondary antibodies rather than fluorophore-conjugated primary antibodies as in the above techniques, allowing the use of "off-the-shelf" primary antibodies[148]. Another method that uses staining and bleaching cycles is co-detection by indexing (CODEX)[150], but it differs from the above

methods as it uses DNA-conjugated antibodies and sequencing-like methods to multiplex. While these cyclic methods have significantly expanded multiplexing capability, a primary limitation is the number of rounds of imaging that are possible before sample degradation begins to occur. Additionally, the length of time each round takes to complete, multiplied by the number of rounds, can make these methods excessively time-consuming.

Another way to achieve higher degrees of antibody multiplexing is by labeling antibodies with isotopically pure rare earth metals, such as in imaging mass cytometry (IMC) [152] and multiplexed ion beam imaging (MIBI) [153]. IMC and MIBI can respectively image 32 and 40 analytes simultaneously from a tissue sample. The use of mass spectrometry for quantification makes these techniques easier to multiplex compared to ones that use fluorescence, as they are not limited by spectral overlap. However, these methods use a laser or ion beam to ablate the sample, destroying the sample and preventing further analysis or use, including cyclic methods as above. Additionally, the specialized equipment and reagents required for these techniques can be more expensive than standard fluorescence microscopes and antibodies, making them not as widely available.

The fluorescence-based techniques that were previously described use “filter-based” imaging that lumps emission wavelengths together and thus restricts multiplexing to 2-4 channels, but some have instead used spectral imaging that measures emission intensity with much finer wavelength resolution. Fluorescence emission follows the principle of linear superposition, meaning that the emission

spectra of a mixture of fluorophores can be cast as a sum of contributions from individual probes using a matrix equation. Solving this matrix equation for the levels of individual probes, given the spectra of the mixture and each isolated probe, is called unmixing. These “hyperspectral” techniques have been used to image up to seven analytes simultaneously in tissue sections[127,154–157]. CLASI-FISH (combinatorial labeling and spectral imaging - fluorescence in situ hybridization), which builds upon traditional spectral imaging, classifies up to 15 microbe types using probe combinations[158]. One constraint of CLASI-FISH is that probes must be spatially segregated for demultiplexing. Spectrally resolved fluorescence lifetime imaging microscopy (sFLIM)[159] combines spectral imaging with fluorescence lifetime information and can multiplex nine antibodies simultaneously.

We recently developed an approach called Multiplexing using Spectral Imaging and Combinatorics (MuSIC), which leverages currently available fluorophores along with the power of combinatorics to increase the number of available probes for simultaneous staining[21]. MuSIC probes are created using Förster resonance energy transfer (FRET)-producing fluorophore combinations, which results in a unique probe emission spectrum that is linearly independent from that of the individual fluorophores that make up the combination, enabling unmixing. Our previous work, based on simulation, suggested that MuSIC may increase simultaneous fluorescence multiplexing capabilities ~4-5 fold[21]. Proof-of-principal experimental studies that focused on a small range of excitation

wavelength space have shown that nine MuSIC probes can be accurately unmixed, which should increase when the full range is used. Moreover, MuSIC is compatible with cyclic imaging methods, which would allow more analytes to be measured per cycle, increasing multiplexing capabilities even further. MuSIC differs from CLASI-FISH in that it is not limited by spatial segregation.

Methods to conjugate MuSIC probes to antibodies have not yet been developed. Our previous work showed that standard primary-amine-based conjugation of two fluorophores to the same antibody does not produce a high enough FRET efficiency to create robust MuSIC probes[160]. Here, we report a fluorescent oligo-based labeling approach to conjugate MuSIC probes to antibodies. A DBCO-Peg5-NHS ester molecule (the linker) is used to attach an azide modified oligo (the docking strand) to the antibody. Fluorescent oligos hybridized to the docking strand bring the fluorophores into FRET-compatible distances. Mixtures of antibody-conjugated MuSIC probes using (i) Cy3, (ii) Tex615, and (iii) a Cy3-Tex615 combination were analyzed and accurately unmixed using spectral flow cytometry as a proof-of-principle. These oligo-based MuSIC probes are compatible with the wide range of clinical, biomedical, and drug discovery applications that currently use fluorescent antibodies and spectral imaging.

Results

Probe design and labeling process. A fundamental component of the Multiplexing using Spectral Imaging and Combinatorics (MuSIC) approach is that combinations of fluorophores exhibiting FRET create a unique emission spectrum that is linearly independent from the individual fluorophores in the combination. Thus, creating MuSIC probes on antibodies requires combinations of fluorophores to be stably associated with antibodies with spatial proximity sufficient for FRET. To achieve this, we started from a prior description of antibody-oligo labeling[161] (Figure 3.1a). First, a DBCO (dibenzocyclooctyne)-PEG5-NHS ester molecule (referred to as the linker) is attached to the antibody. The NHS ester group at the end of the linker reacts with available NH_2 groups on the surface of the antibody. From here, a 55 bp DNA oligo with a 5' azide modification (referred to as the docking strand) is added to the complex. The azide reacts with the DBCO group of the linker via copper-free click chemistry, creating an antibody-linker-docking strand conjugate. The PEG5 group is included in the linker to increase the water solubility of the DBCO group and provide space between the antibody and the docking strand[161]. Finally, 20 bp oligos with 5' or 3' fluorophore modifications (referred to as the donor and acceptor strands, respectively) are added to the antibody-linker-docking strand conjugate solution. When the donor and acceptor strands hybridize to the docking strand, the two fluorophores are in close physical proximity to enable FRET. The final product of these reactions should be an

antibody labeled with a MuSIC probe. An in-depth view of the linker and oligo complex is shown in Figure 3.1b.

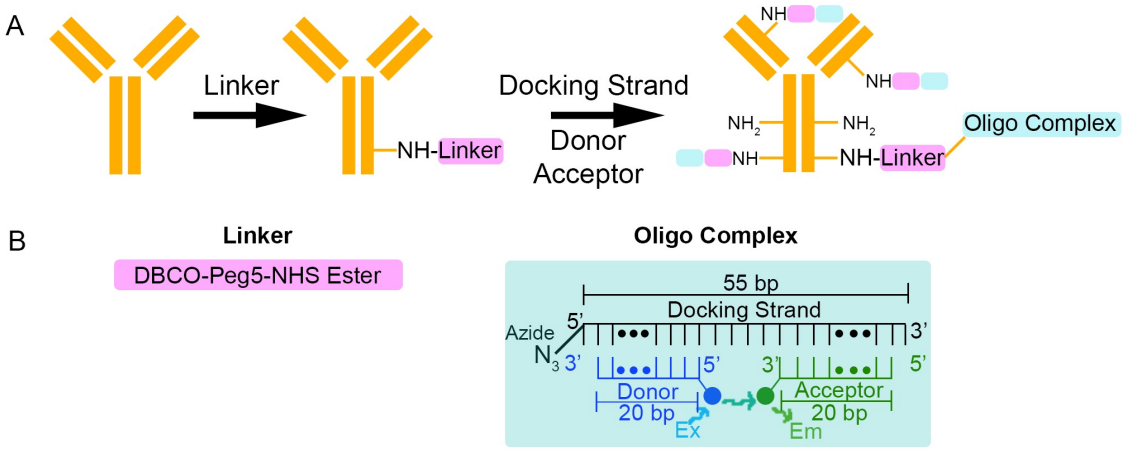

Figure 3.1: Labeling antibodies with oligo-based MuSIC probes. (A) Labeling schematic for MuSIC probes. First, the linker is added to the antibody by reacting the NHS ester on the linker with the NH_2 group on the antibody. Then the docking strand is added and reacts with the linker via copper-free click chemistry. Lastly, the donor and acceptor strands are annealed to the docking strand to form the oligo complex. The linker can attach to the antibody at multiple NH_2 sites, allowing an increased degree of labeling. (B) Detailed versions of the linker and the oligo complex.

Attaching the linker to the antibody. We developed the protocol around labeling 50 μg of IgG, although it is scalable in either direction. The linker is added to the antibody in 60 molar excess, as the linker will react with multiple free amine sites on the surface of the antibody, and the extent of reaction is not certain, but it is desired to maximize the degree of labeling. After incubation, unattached linker

needs to be separated from the antibody-linker conjugate. To do this, we used Amicon Ultra 100 kDa molecular weight cut-off (MWCO) filters (Figure 3.2a). The antibody has a molecular weight of ~150 kDa and the linker has a molecular weight of 0.7 kDa, so once the solution is spun and washed, any linker that does not attach to the antibody will freely flow through the column (Figure 3.2b). In order to verify that all unattached linker was removed, retentate absorbances were measured at 309 nm, where the linker strongly absorbs[161] (Fig. 3.S1), for samples containing the antibody alone, the linker alone, and then antibody and linker together. Results show that the linker is predominantly in the retentate only when the antibody is present (Figure 3.2c). The degree of labeling was estimated to be ~9+/- 0.57 molecules of linker/antibody based on absorbance measurements (see Methods and Figure 3.S1). These results demonstrate that the antibody and linker can stably associate and that unattached linker can be effectively removed from solution.

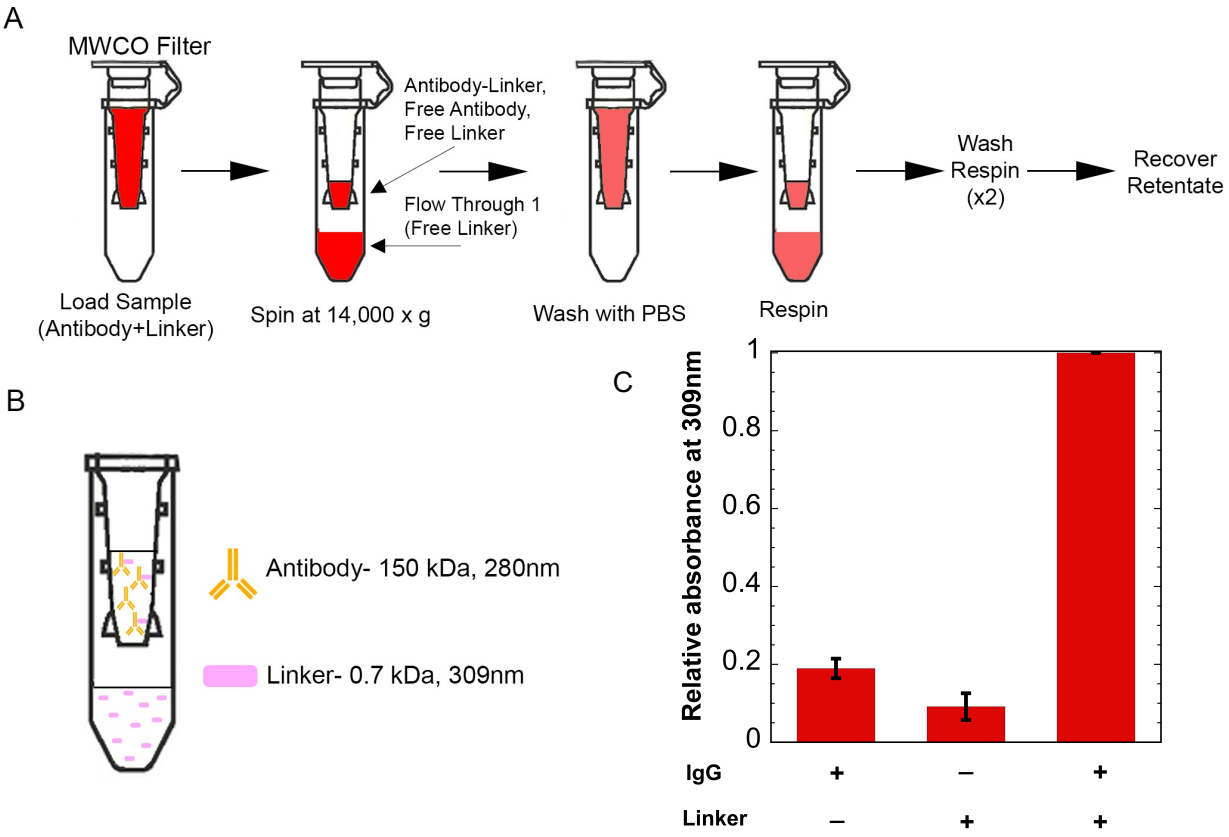

Figure 3.2: Adding linker to antibody. (A) Separating free linker using 100 kDa molecular weight cut-off (MWCO) filters. The antibody and linker are incubated, then the sample is added to the molecular weight cut-off filters. The filters are spun to separate unattached linker and then go through a series of washes. Finally, the retentate is recovered. (B) Expected separation of components after spin and wash steps. (C) Retentate absorbances at 309nm. Results show an increased signal at 309nm when the linker is in the presence of the antibody.

Attaching the docking strand to the antibody. We added the docking strand to the antibody-linker retentate from the previous step in 6 molar excess to the antibody to account for multiple labeling sites. After incubation, unattached docking strand needs to be separated from the antibody-linker-docking strand conjugate. Similar to above, we use Amicon Ultra 100 kDa MWCO filters (Figure 3.3a). Since the docking strand is only 17 kDa, it should freely flow through the columns if it is not attached to the antibody-linker conjugate (Figure 3.3b). In order to evaluate whether unattached docking strand is removed, retentate absorbances were measured at 260 nm, as this is where the docking strand strongly absorbs. Results show that the docking strand can be seen in the retentate when in the presence of the antibody and the linker, as expected. However, a strong retentate signal was also seen for the docking strand when in the presence of only the antibody, without the linker (Figure 3.3c). The cause for the strong docking strand signal in the retentate without the linker present is unknown, but before proceeding, we wanted to understand whether the docking strand was stably bound to the antibody without the linker present or whether it could be removed with further washing via an orthogonal separation mechanism.

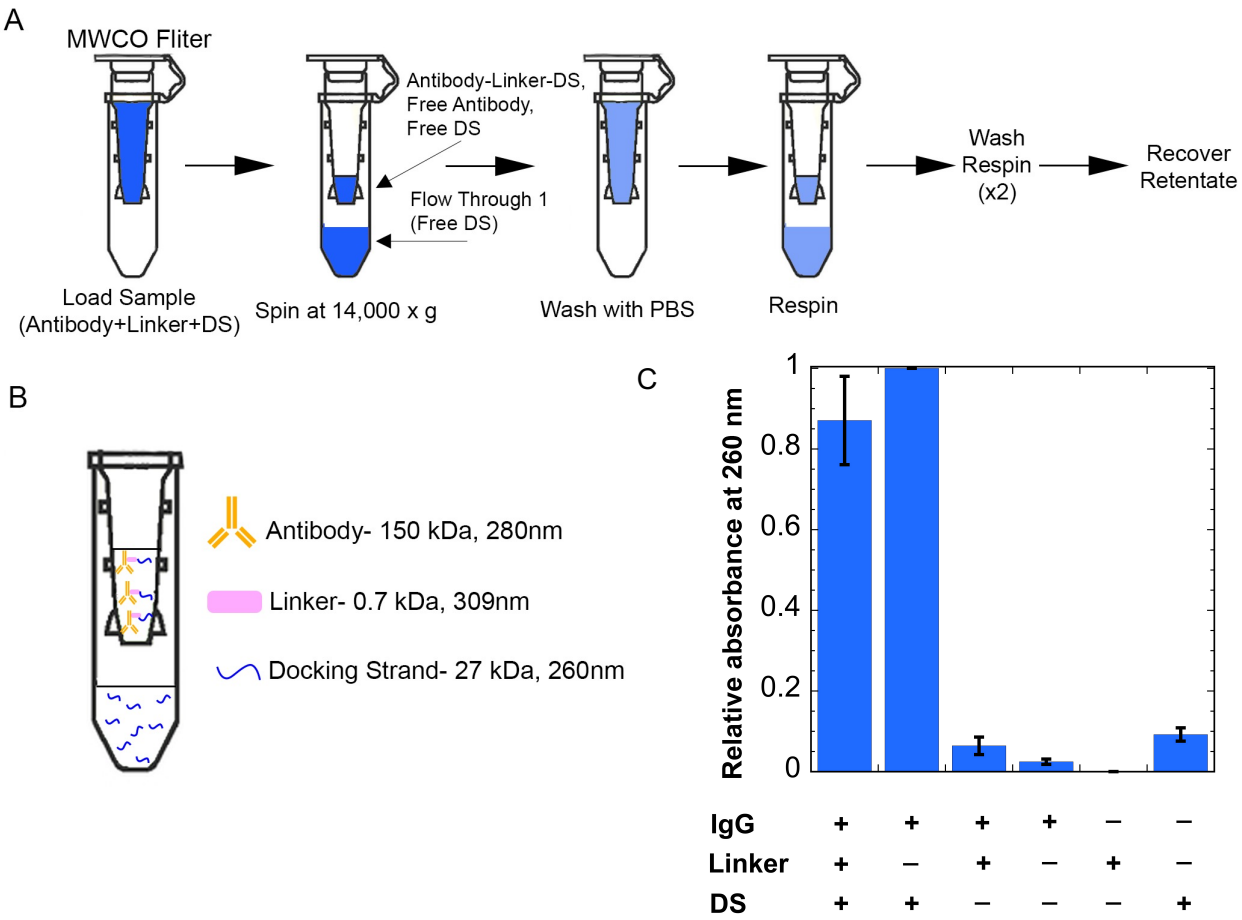

Figure 3.3: Adding docking strand (DS) to antibody-linker. (A) Separating free DS using 100 kDa MWCO centrifugal filters. The DS and antibody-linker conjugate are incubated, then the sample is added to the molecular weight cut-off filters. (B) Expected separation of components after spin and wash steps. (C) Retentate absorbances at 260nm. Results show an increased signal at 260nm when the DS is in the presence of the antibody-linker conjugate. An increased signal can also be seen for the case of just the DS and antibody, which is accounted for in later steps.

The docking strand requires the linker to be stably associated with the antibody. To determine whether the docking strand could stably bind to the antibody without the linker, we used protein A dynabeads. The beads should strongly and selectively bind to the antibody, and anything attached to the antibody will also be bound to the beads. We generated samples with and without linker containing antibody, docking strand, and a donor strand with the fluorophore Atto 488 (for measurement). The supernatant containing any non-stably attached reagents can be removed by washing when the solution is placed on a magnet (Figure 3.4a). Atto 488 fluorescence was measured to evaluate whether the docking strand could stably associate with the antibody without the linker. The bead-based nature of the experiment precluded reliable absorbance assays as used previously; consequently, we are not able to estimate the degree of labeling for the docking strand on the antibody. The fluorescence signal for samples without the linker present was comparable to the signals of the controls where no fluorophore was present, while when the linker was present, a significant fluorescence signal was observed (Figure 3.4b). We conclude that the linker is needed for the antibody to be stably associated with the docking strand, and subsequently, fluorophore-labeled donor or acceptor strands.

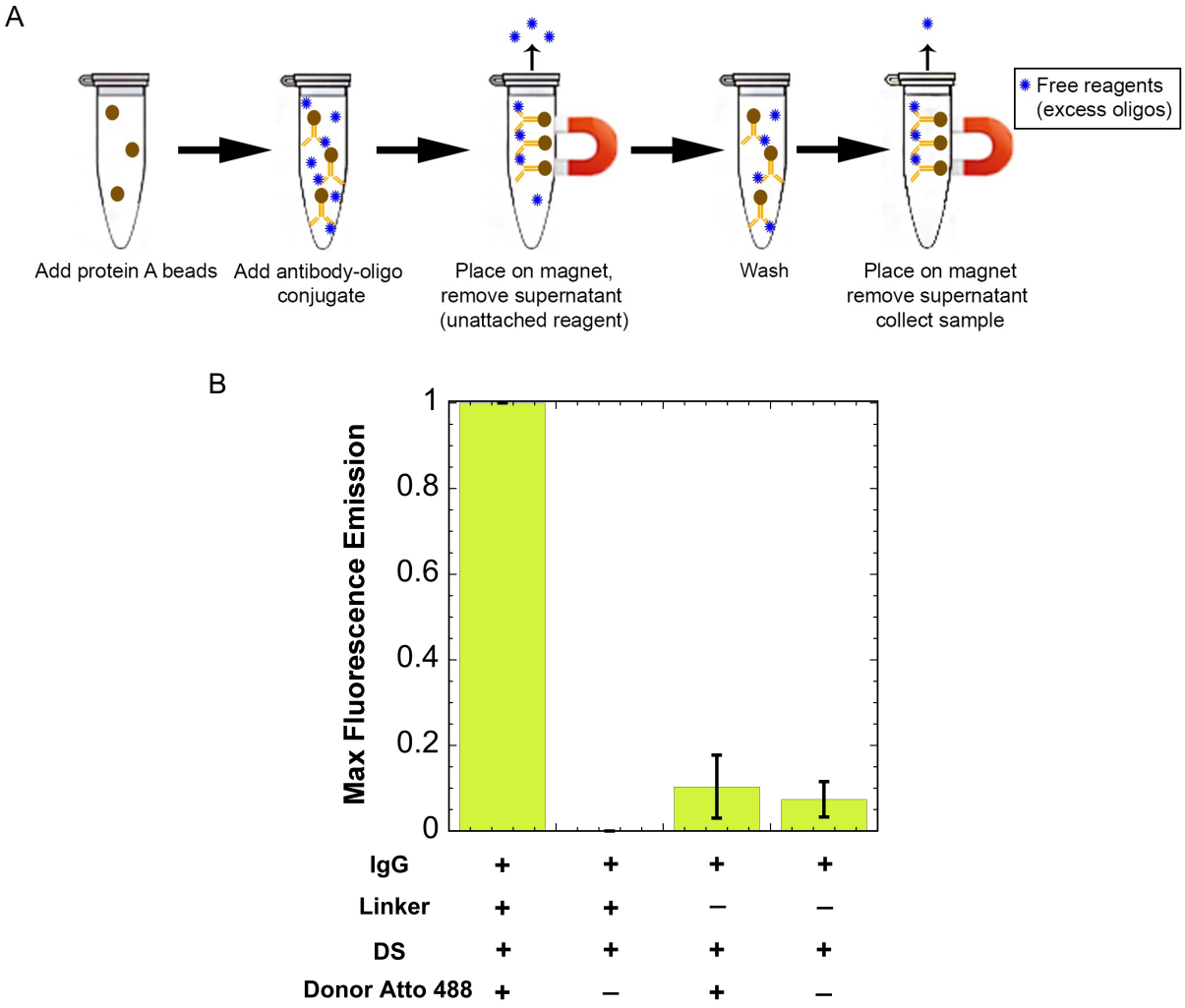

Figure 3.4: Separating free reagents using protein A beads. (A) The antibody-oligo conjugate (red Y with a blue circle attached) is added to the protein A beads (brown circle) and is incubated with rotation for 10 minutes. It is then placed on a magnet, pulling the beads out of solution, and the supernatant containing free reagents (unattached blue circles) is removed. The final product is collected containing the antibody-oligo conjugate. (B) Maximum fluorescence intensity values when excited at 450nm. Results show an increased fluorescence signal for the donor when the

linker is added. Without the linker, the fluorescence signal for the donor is the same intensity as the background fluorescence.

Obtaining a donor and acceptor pair that produces FRET when co-hybridized to the docking strand. As mentioned above, MuSIC probes must have donor and acceptor pairs that exhibit FRET, such that the combination probe has a unique spectral signature. To test if a donor and acceptor pair exhibits FRET, the emission spectra of solutions containing (i) just the donor, (ii) just the acceptor, (iii) the donor and the acceptor, and (iv) the donor and acceptor co-hybridized to the docking strand were analyzed using a plate reader (Figure 3.5a). We used 488 nm excitation, a common laser line in multiple assay types. The pair of Cy3 (donor) and Tex615 (acceptor) showed a much larger, red-shifted emission peak when excited at 488 nm and co-hybridized to the docking strand, as compared to the case without docking strand, indicating strong FRET (Figure 3.5a). These results show that this donor and acceptor pair would be a suitable MuSIC probe candidate, i.e., a donor and acceptor strand hybridized to the antibody-linker-docking strand conjugate.

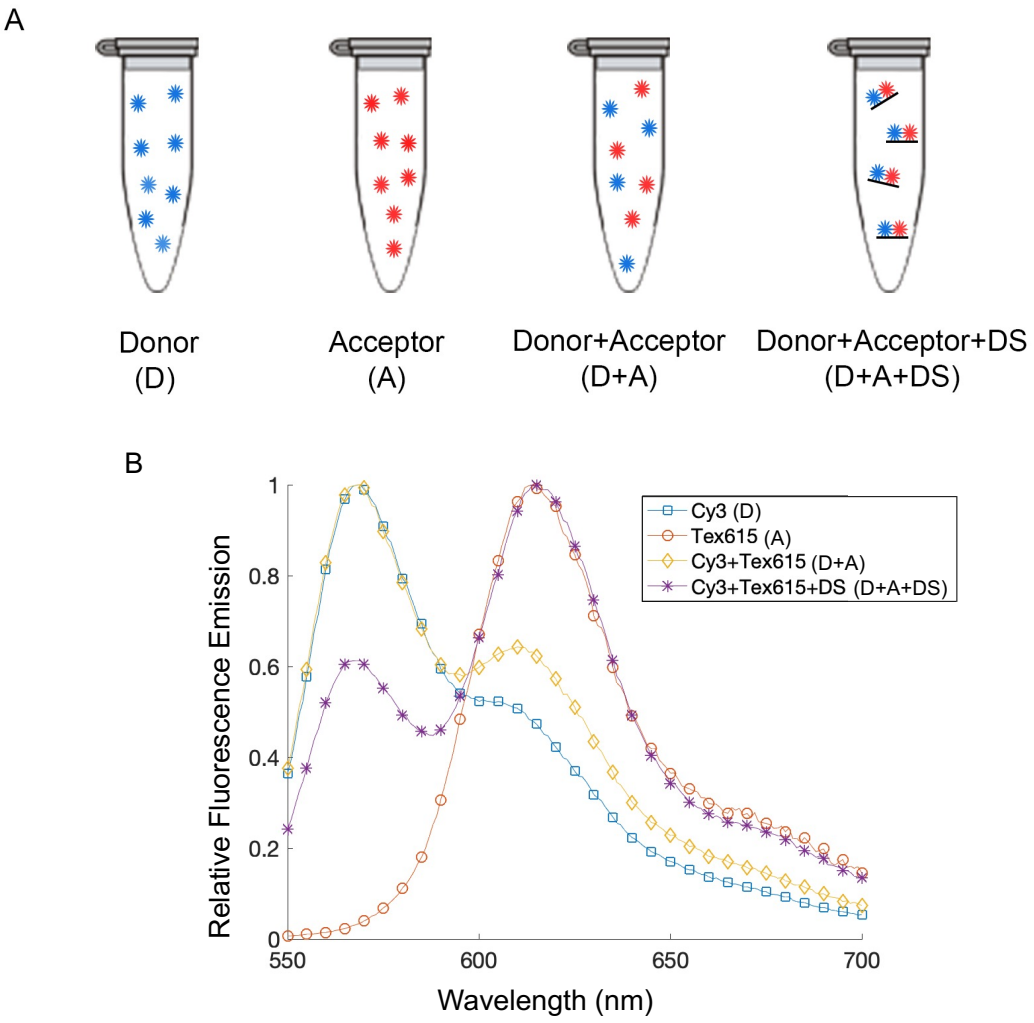

Figure 3.5: Donor and acceptor fluorophore pair, Cy3 and Tex615. (A) Experimental setup for testing fluorophore combination. The tubes contain the donor alone (blue circles), the acceptor alone (red circles), the donor and acceptor free in solution together, and then the donor and acceptor bound to the docking strand (black line). We expect only the sample with the DS shows significant FRET. DS: docking strand. (B) Fluorescence emission spectra when excited at 488 nm.

An increased acceptor emission peak is seen when the donor and acceptor are annealed to the docking strand, indicating increased FRET.

Application to flow cytometry for event classification. While there are many potential applications of MuSIC probe-labeled antibodies, we set out to obtain proof-of-principle data using spectral flow cytometry. Namely, we wanted to understand whether we could (i) robustly classify events as containing a particular combination of MuSIC probes and (ii) estimate the proportion of events having a particular probe staining pattern (Fig. 3.6a). This is analogous to cell type classification assays such as peripheral blood mononuclear cell (PBMC) analysis[162,163]. Three antibody batches with different probes were created: probe 1-donor Cy3 and acceptor Cy3; probe 2-donor Tex615 and acceptor Tex615; and probe 3-donor Cy3 and acceptor Tex615. Because Cy3 and Tex615 produce FRET when co-hybridized to the docking strand, probes with this combination of fluorophores can be thought of as a different "color" from the probes with the individual fluorophores of the combination. Once the antibodies with either MuSIC probe 1, 2, or 3 are created, they are incubated with protein A dynabeads to be analyzed using the flow cytometer. Each bead is similar to a single "cell." One or more antibody type (i.e., with probes 1, 2, or 3) can be conjugated to the same set of beads. For example, incubating beads with two antibody types creates "double positive beads (cells)." In the following set of experiments, we made single positive beads (one antibody type conjugated to one bead set), double positive beads (two

antibody types conjugated to one bead set), and triple positive beads (three antibody types conjugated to one bead set) (Figure 3.6a). This is related to (i) above. We also make mixtures of these different bead sets. This is related to (ii) above. For analysis, we use simple quadrant gates on bivariate plots to classify beads as negative, single positive, or double positive, and additionally, estimate the proportion of beads that fall into each category (Figure 3.6b). Populations of single positive beads are observed in R1 and R4, populations of double positive beads are observed in R2, and the negative population of beads is observed in R3. Triple positive bead classification is done by further gating on double positive populations.

First, we made an equal 3-way mixture from single positive bead sets and analyzed it by spectral flow cytometry. Unmixing results showed relatively equal amounts of each bead type in the mixture, demonstrating that single positives could be robustly classified (Figure 3.6c, 6d first column). We also tested a single positive mixture containing more probe 1 beads than probe 2 or 3 beads, and unmixing results showed relatively similar compositions compared to the known compositions (Figure 3.6d second column). We then investigated if various mixtures of single, double, and triple positive beads could be accurately unmixed (Figure 3.6d). Overall, results demonstrate robust classification of bead type, as well as accurate estimation of the relative abundance of each bead type. (Figure 6d-compare actual to inferred heatmaps). We conclude that MuSIC probe-labeled

antibodies as generated here can be used in spectral flow cytometry applications for cell type classification and proportion estimation.

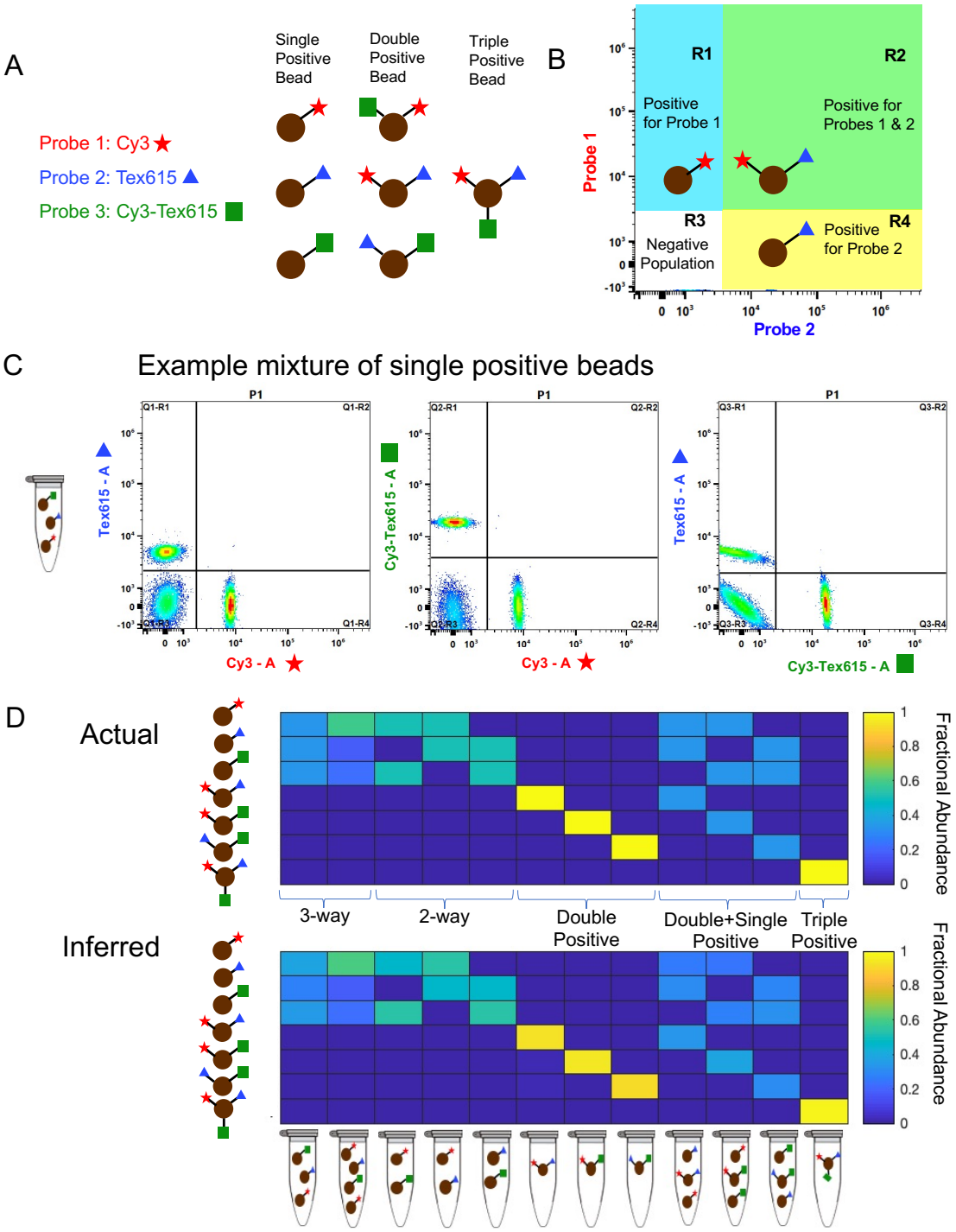

Figure 3.6: Spectral flow cytometry setup and results. (A) Experimental setup for the three-probe mixture ((1) Cy3 (red star), (2) Tex615 (blue triangle), and (3) Cy3-Tex615 (green square)) using single positive, double positive, and triple positive beads (brown circles). (B) Gating strategy for the populations of beads in the three-probe mixture. (C) Unmixing populations of single-labeled beads in a three-way equimolar mixture of probes Cy3, Tex615, and Cy3-Tex615 using spectral flow cytometry. The plots show unmixing results of Tex615 compared to Cy3 (left), Cy3-Tex615 compared to Cy3 (middle), and Tex615 compared to Cy3-Tex615 (right). (D) Comparing actual amounts of each probe in the mixture (top panel) to the inferred or calculated amounts of each probe in the mixture (bottom panel). The composition of each mixture is shown below the bottom panel.

Discussion

Here we established a method to conjugate two fluorophores to an antibody in a way that enables FRET between them (if they are compatible). The use of combinations of fluorophores that exhibit FRET creates unique emission spectral signatures that can be used for multiplexing via the MuSIC approach. Antibodies are labeled with combinations of fluorophores by combining a “linker” and DNA oligos. The linker is used to covalently attach a “docking strand” oligo to the antibody. Separate “donor” and “acceptor” strands then hybridize to the docking strand. The donor and acceptor strand oligos place the fluorophores at a specified distance from one another on the antibody. Absorbance data suggested a degree of labeling of ~9+/- 0.57 linker/antibody molecules. We validated the approach using three different MuSIC probes (Cy3, Tex615, and a Cy3-Tex615 combination) attached to three separate mixtures of antibodies. MuSIC probe-labeled antibodies attached to protein A beads served as surrogate single, double, and triple positive cells for testing via spectral flow cytometry. Spectral flow cytometry experiments demonstrated that each MuSIC probe can be uniquely differentiated by accurately determining compositions of bead mixtures.

While the focus here was using MuSIC probe labeled antibodies with spectral flow cytometry, they are also compatible in principle with spectral imaging. Several methods that increase image multiplexing capabilities use a stain/strip technique, which involves cycles of staining, imaging, and bleaching[147,149,151,164]. These methods have improved multiplexing abilities by ~10 fold over standard

single-round 4-color imaging. The use of MuSIC probes is in principle compatible with the cyclic methods, which would expand the number of probes that can be used per round of imaging using spectral scanning microscopes. Current cyclic methods on average use 10 rounds of four-color imaging and our previous simulation studies suggested that ~25 MuSIC probes might be accurately unmixed[21]. Therefore, the use of MuSIC probes may allow 10 rounds of 25 color imaging, thus increasing multiplexing capabilities by roughly another six-fold. However, spectral emission scanning microscopes are certainly not as pervasive and filter-based microscopes currently. Angle-tuned emission filters for wavelength scanning may help to make such technology more accessible[165]. Such microscopes also commonly have white light lasers for tunable excitation wavelengths and a potentially large number of channels, which would further empower multiplexing capabilities via MuSIC approaches.

To further increase fluorescent multiplexing capabilities using the MuSIC approach, additional combinations of fluorophores are needed. The FRET efficiency of a fluorophore combination is dependent on the physical distance between the two fluorophores based on the Förster radius, which is dependent on the spectral properties of the pair. Some fluorophore pairs may require different distances between the two fluorophores in order to optimize FRET efficiency. This distance between the fluorophores can be varied by using different length docking strands which have varying numbers of spacer base pairs—the nucleotides in the middle between the donor and acceptor strand binding sites. Thus, we expect

future solutions will use different length docking strands for different fluorophore combinations in the march towards a larger palate of antibody-compatible MuSIC probes. Additionally, in this paper, we demonstrated unmixing of MuSIC probes using a two-laser spectral flow cytometer (488nm and 638 nm). The number of useful MuSIC probe combinations can be further increased by using a spectral flow cytometer with five excitation lasers (355 nm, 405 nm, 488nm, 561 nm, and 638nm—Cytek Aurora). We are currently screening large sets of fluorescent oligos for MuSIC-probe suitability for a 3-laser and 5-laser setup.

While MuSIC probes may be useful for multiple flow cytometry applications, one of which in particular is immune profiling[166–168]. Flow cytometry-based immune profiling has limited multiplexing to roughly a dozen analytes (depending on the capabilities of the instrument) as a result of spectral overlap[10,169]. Mass cytometry has been transformative for immune profiling[170–172], but is slower than flow cytometry and is destructive, so it prevents further use of the cells after analysis[169]. The use of MuSIC probes for immune profiling via flow cytometry may allow for increased multiplexing for deep immune profiling on par with mass cytometry while also being fast (more than 10,000 cells/second rather than about 1,000 as with mass cytometry[173]) and non-destructive. This could open up avenues of increased throughput for monitoring immune responses across large patient cohorts, as well as the isolation of rare cell types alone or in specified combinations that would otherwise not be possible.

We conclude that oligo-based approaches are a robust and modular way to create MuSIC probe-labeled antibodies. Future work needs to expand the MuSIC probe palette, as well as expand to larger antibody panels for flow cytometry or other spectral fluorescence applications. This would enable broader applications for advancing our understanding of microbial communities[174] such as gut and skin microbiomes[175,176], cancer research and clinical diagnostics, host-pathogen interactions, developmental biology, and many other areas of life science research where more highly multiplexed single and sub-cellular resolution of antibody-target readouts is informative.

Methods

Adding the linker to the antibody

This and the below procedures were developed around labeling 50 μg of IgG but are compatible with scaling up or down. In our case, normal Rabbit IgG (ThermoFisher Cat: 31235) is combined with DBCO-Peg5-NHS Ester (linker; 10 mM in DMSO; Click Chemistry Tools Cat: 1378531-80-6) in 20 molar excess (50 μg of Rabbit IgG and 4.6 μg of linker). This is brought to a volume of 100μl with PBS and allowed to incubate for 30 minutes at 25°C. After incubation, the solution is added to an Amicon Ultra 0.5ml 100 kDa centrifugal filter (Fisher Scientific Cat: UFC5100BK) and spun for 5 minutes at 14,000 x g. The filter is then placed into a new tube, and PBS is added to the top of the filter in order to bring the total volume back to 100 μl and is spun again for 5 minutes at 14,000 x g. This wash step is repeated twice more (three total). Finally, the filter is flipped upside down and placed in a clean tube and spun for 1 minute at 1000 x g to collect the retentate. The retentate absorbance is measured at 309nm, where the linker strongly absorbs, and 280nm, where the antibody strongly absorbs, using a NanoDrop spectrophotometer (Thermo Scientific).

Adding the docking strand to the antibody-linker conjugate

The docking strand (Integrated DNA technologies-Table 3.1) is added to the antibody-linker retentate from the previous step in 6 molar excess to the original amount of antibody (2 nmoles of docking strand). The volume is brought up to 100 μl with PBS and incubated at 4°C overnight. The sample is then placed in an

Amicon Ultra 0.5ml 100 kDa centrifugal filter and spun for 5 minutes at 14,000 x g. Once this spin is completed, the filter is placed into a new tube, and PBS is added to the top of the filter in order to bring the total volume back to 100 μl and is spun again for 5 minutes at 14,000 x g. This wash step is repeated twice. Finally, the filter is flipped upside down and placed in a clean tube and spun for 1 minute at 1000 x g to collect the retentate. The retentate absorbance is measured at 309nm and 280nm as above, and also at 260nm, where the docking strand strongly absorbs light, using a NanoDrop spectrophotometer (Thermo Scientific).

Table 3.1: Oligo Sequence

Component	**Sequence**
Docking Strand	5' – Azide - GTG TAG TTC AGG TCA AGA CAT CGT GCG ACC AGT CAG CAT GAG ACT CAT TGG TGC G -3'
Donor Strand	3'- C AAG TCC AGT TCT GTA GCA C - Fluorophore- 5'
Acceptor Strand	3' - Fluorophore - CA GTC GTA CTC TGA GTA AC – 5'

Degree of Labeling

To generate calibration curves for concentrations of the antibody, linker, and docking strand, absorbance measurements were taken using a NanoDrop spectrophotometer (Thermo Scientific) for known concentrations of the antibody, linker, and docking strand at 309, 280, and 260 nm. Five-point, 2-fold serial dilutions were used to generate samples for the calibration curve. A least-squares line of best fit (MATLAB) is generated to estimate absorbance extinction coefficients based on Beer's law (1) for each component at 309, 280, and 260nm.

(1)

$$A = \varepsilon c L$$

Here, *A* is the absorbance of the solution, ε is the extinction coefficient, *L* is the length of the path traveled by light (1 mm), and *c* is the concentration of the solution. From here, a system of three simultaneous equations are solved in Matlab using the function `vpasolve` to estimate molar concentrations of the antibody (a), linker (l), and docking strand (DS) given absorbance measurements at 260, 280, and 309 nm from a mixture (M).

(2)

$$A_{M-309nm} = c_l * \ \varepsilon_{l-309nm} + c_a * \varepsilon_{a-309nm} + c_{DS} * \varepsilon_{DS-309nm}$$

(3)

$$A_{M-260nm} = c_l * \ \varepsilon_{l-260nm} + c_a * \varepsilon_{a-260nm} + c_{DS} * \varepsilon_{DS-260nm}$$

(4)

$$A_{M-280nm} = c_l * \ \varepsilon_{l-280nm} + c_a * \varepsilon_{a-280nm} + c_{DS} * \varepsilon_{DS-280nm}$$

The degree of labeling for the linker to antibody could be calculated from the above-estimated concentrations. However, due to the nature of the spin column-based separation, some unreacted linker will remain. This amount of residual linker can be calculated based on mole balance, and we used this calculation to correct the degree of labeling as follows, where *n* is the number of washes, c_{l0} is the initial concentration of the linker ($\frac{mmole}{ml}$) before washing, V_r is the volume of the retentate (ml) after washes, V_w is the wash volume (ml), and V_{rf} is the volume of the final retentate (ml).

$$\frac{c_{l0} * {V_r}^n}{{V_w}^{n-1} * V_{rf}} = c_{residual-linker}$$

The concentration of the residual linker is subtracted from the calculated linker concentration to determine the concentration of the linker that is attached to the antibody in the retentate. The degree of labeling is then calculated as the ratio of this adjusted linker concentration to that of the antibody concentration.

Adding the donor and acceptor strands to the antibody-linker-docking strand conjugate

A 20 bp oligo with a 5' fluorophore modification (donor strand) and a 20 bp oligo with a 3' fluorophore modification (acceptor strand) (each 100 μM in water, Integrated DNA technologies) are added in equimolar amounts (2 nmoles each) to the antibody-linker-docking strand retentate and brought up to 100 μl with PBS. Sequences are shown in Table 1. This solution is allowed to incubate for 15 minutes at 25°C in the dark. When testing the necessity of the linker, the donor strand with an Atto 488 modification was added to the antibody-linker-docking strand retentate. To make the different probes, Probe 1 consists of equimolar amounts of the donor strand with a Cy3 modification and the acceptor strand with a Cy3 modification (each 2 nmoles), Probe 2 consists of equimolar amounts of the donor strand with a Tex615 modification and the acceptor strand with a Tex615 modification (each 2 nmoles), and Probe 3 consists of equimolar amounts of the

donor strand with a Cy3 modification and the acceptor strand with a Tex615 modification (each 2 nmoles).

Choosing donor and acceptor pairs

To test the donor and acceptor fluorophore pair of Cy3 and Tex615, four samples are created: (1) donor strand with a 5' Cy3 modification and acceptor strand with a 3' Tex615 modification (each 100 μM in water) are added in equimolar amounts (0.2 nmoles), (2) The donor, acceptor, and docking strands are added in equimolar amounts (0.2 nmoles), (3) 0.2 nmoles of the donor strand, (4) 0.2 nmoles of the acceptor strand. All samples are brought to 50 μl with PBS. The samples (oligos in solution) are loaded into a black 96 well plate (Fisher Scientific Cat: 655900), and fluorescence emission spectra are assayed with a Synergy MX microplate reader (Biotek). Parameters are set to a slit width of 9nm, a 10-second shake prior to reading, taking readings from the top, and an excitation wavelength of 488 nm. The emission start ranges are 50nm greater than the excitation wavelength.

Incubating labeled antibodies with protein A dynabeads

The MuSIC-probe labeled antibodies from above were suspended in 200 μl of 0.02% (2 μl/10ml) Tween 20 (Fisher Scientific Cat: 9005-64-5) in PBS and added to 50 μl of protein A dynabeads (Fisher Scientific Cat: 10 001 D—33 μg of initially added IgG; 100 μg batch makes three incubations). For making double positive beads, both probes are simultaneously added to 50 μl of protein A dynabeads. This solution is allowed to incubate for 10 minutes with rotation in the

dark. After incubation, the solution is placed on a magnet, the supernatant is removed, and the bead-antibody complex is resuspended in 200 μl PBS with 0.02% Tween-20 (Fisher Scientific Cat: BP337-100). The solution is then placed back on the magnet, and the supernatant is again removed and is resuspended in PBS.

Analyzing probe mixtures using Cytek Aurora flow cytometer

Mixtures of bead-conjugated probes are analyzed using a Cytek Aurora spectral flow cytometer with 488nm and 638nm lasers. First, beads with single probes are assayed as reference controls. The events to record is set to 5,000, the stopping time is set to 10,000 sec, and the stopping volume is set to 3,000 μl. For samples containing mixtures of bead types or double-positive beads, the events to record are set to 15,000, the stopping time is set to 10,000 sec, and the stopping volume is set to 3,000 μl. Once mixtures have been analyzed, the SpectroFlo software (Cytek) is used to first gate single beads with forward and side scatter, and then to unmix and report (i) the amount of each probe on every bead that was analyzed and (ii) the fraction of each bead type in each mixture of bead types.

Acknowledgments: We thank Allon Klein at HMS Systems Biology for helpful discussion related to oligo-based labeling and Chloe Worthy for help with illustrations.

Funding Information: MRB received funding from Clemson University and the NIH/NCI Grant R21CA196418. MEM received funding from the Department of Education Grant P200A180076.

CHAPTER FOUR

INCREASING FLUORESCENT SIGNAL OF OLIGO-BASED LABELS FOR SPECTRAL FLOW CYTOMETRY

Abstract

Fluorescent antibodies are an important tool for biomedical research, particularly for single-cell readouts. Full-spectrum flow cytometry has increased fluorescent antibody-based multiplexing capabilities to ~40 simultaneous markers but remains limited compared to single-cell RNA-sequencing which can identify 100s-10,000s of markers. However, single-cell RNA-sequencing is limited by higher cost and sample destruction, leaving motivation for more multiplexing with full spectrum flow cytometry. We recently proposed fluorescence Multiplexing using Spectral Imaging and Combinatorics (MuSIC), which uses combinations of existing fluorophores to create new spectrally unique MuSIC probes and developed an associated oligo-based antibody labeling method. In this work, we found that such MuSIC-probe labeled antibodies had significantly lower signal intensity than conventionally-labeled antibodies in human cell experiments. We then modified the position of fluorophore labels in the oligos to investigate whether improved signal intensity could be obtained. Specifically, rather than using 3' or 5' fluorophore-labeled oligos (ext.), we tested oligos with internal (int.) fluorophore modifications. Cell-free spectrophotometer measurements showed a ~6-fold

signal intensity increase of the new int. oligo configuration compared to the previous ext. oligo configuration. This approach was further validated by using CD8 antibodies labeled with ext. and int. MuSIC probes or conventional labeling to stain human peripheral blood mononuclear cells (PBMCs). Spectral flow cytometry experiments showed that int. MuSIC probe-labeled antibodies can be used to stain PBMCs with an intensity that is equal to or greater than conventionally-labeled antibodies while having no significant impact on the estimated proportion of CD8+ lymphocytes. The antibody labeling approach is general and can be broadly applied to many biological and diagnostic applications, such as tissue imaging, when fluorescence emission spectra detection is available.

Introduction

Fluorescent antibodies are an integral tool for biological and diagnostic applications[177]. One application for fluorescent antibodies is flow cytometry[17]. The use of fluorescent antibodies with conventional flow cytometers is restricted to typically 3-4 markers, but up to ~10-15 markers have been reported[15–17]. This is largely due to spectral overlap between fluorophores, limiting the number of analytes that can be reliably detected. Regardless, flow cytometry remains a useful platform as it is a cost-effective, high-throughput, and non-destructive method for single-cell analysis[178,179]. Recent advances have led to full-spectrum flow cytometry (FSFC), which captures the entire fluorophore emission spectra, creating a unique spectral fingerprint for each fluorophore[18,180]. This allows fluorophores with similar peak emissions to be used in the same panel, so long as they have distinctive spectral signatures. FSFC has enabled the detection of up to 40 markers simultaneously[19], but further multiplexing capabilities are stunted by the number of commercially available dyes that are compatible in a singular panel. Moreover, FSFC is still far from meeting the multiplexing capabilities of methods such as single-cell RNA sequencing, which has the ability to identify 100s-10,000s of markers[181,182].

The 40-plex FSFC panel, previously mentioned, largely relies on single-dye fluorescent antibodies, with relatively few tandem-dye fluorescent antibodies[19]. We recently developed Multiplexing using Spectral Imaging and Combinatorics

(MuSIC), which uses combinations of currently available fluorophores to create spectrally unique MuSIC probes[21]. MuSIC probe-labeled antibodies may expand the multiplexing capability for FSFC by providing new tandem probes. Previously, we proposed an oligo-based method for covalently labeling antibodies with MuSIC probes **(Fig 4.1A)** and validated this method using spin column purification and absorbance measurements [183]. However, this method had yet to be tested on human cells.

In the current study, we first explored the application of this method on human peripheral blood mononuclear cells (PBMC). However, in doing so, we found that our previous method for labeling antibodies with MuSIC probes[183] has a significantly lower staining intensity, compared to a conventional antibody labeling kit (Biotium Mix-n-Stain Antibody Labeling Kit). Consequently, we hypothesized that a different oligo-fluorophore arrangement of the MuSIC probes, using internal fluorophore modifications rather than external fluorophore modifications, could increase the fluorescent signal intensity of MuSIC-probe labeled antibodies. Results showed that the new method with internal fluorophore modifications produced ~6-fold increase in fluorescent signal compared to the previous method. We then again compared the internally modified MuSIC-probe labeled antibodies to the conventionally labeled antibodies by staining PBMCs. Results showed that the new internal labeling method has ~2.5-fold increase in fluorescent signal over the conventionally labeled antibodies while having no significant difference in the estimated % of CD8+ lymphocytes. This increased

fluorescent signal suggests the potential of MuSIC-probe labeled antibodies to add to the existing capabilities of FCFS, by providing new spectrally unique fluorescent antibodies with competitive intensity. Such antibodies are not restricted to FSFC but could be useful for other biomedical applications such as tissue heterogeneity studies with immunofluorescence imaging when spectral detection is available.

Methods

Measuring fluorescent oligo emission spectra

All oligos (Integrated DNA Technologies, Table 1) used here are resuspended in ddH20 at 100 μM. In a black 96-well plate (Fisher Scientific Cat: 655900), 200 μmols of the fluorescent oligo(s) is added to the well and the volume is brought up to 50μl with PBS. The fluorescent emission spectra are gathered using a Synergy MX microplate reader (Biotek) with parameters set to a slit width of 9 nm, taking readings from the top, an excitation wavelength set to the maximum excitation wavelength for that fluorophore, and an emission wavelength starting 30 nm after the excitation wavelength (Table 2) and emission collected at every nm.

Table 4.1: Oligo sequences for the Ext. and Int Oligo complexes (Integrated DNA Technologies)

	Component	**Sequence**
Ext. Oligo Complex	Docking Strand	5′-azide-GTG TAG TTC AGG TCA AGA CAT CGT GCG ACC AGT CAG CAT GAG ACT CAT TGG TGC G-3′
	5’ Donor Strand	3′-C AAG TCC AGT TCT GTA GCA C-fluorophore-5′
	3’ Acceptor Strand	3′-fluorophore-CA GTC GTA CTC TGA GTA AC-5′
Int. Oligo Complex	Azide Strand	3’ CGT TAT GAA CCT GA 5’
	Int. Donor Strand	5’ GCA ATA CTT GGA CTA GTC TAG GCG AAC GTT TAA GGC GAT TCT TGT T-fluorophore- A CAA CTC CGA AAT AGG CCG 3’
	Ext. Acceptor Strand	3’ CAG ATC CGC TTG CAA ATT CCG C – fluorophore-A GAG ACA AAT GTT GAG GCT TTA TCC GGC 5’

Table 4.2: Fluorophore modifications for Donor and Acceptor Strands with their corresponding excitation wavelength and emission start wavelength.

Fluorophore Modification	Excitation (nm)	Emission (nm)
6-FAM (Fluorescein)	490	520
Atto 488	492	522
Atto 532	524	554
MAX (NHS Ester)	527	557
Cy3	534	564
Atto 550	545	575
Tamra (NHS Ester)	553	583
Atto 565	561	591
ROX (NHS Ester)	578	608
TEX 615	583	613
Atto 590	594	624
Atto 633	623	653
Atto 647	632	662
Cy5	638	668
Cy5.5	676	706

Labeling Antibodies

Antibodies are conjugated according to McCarthy et. al 2021[183]. In short, the antibody (CD8 clone RPA-T8; Biolegend Cat: 301002) is incubated with DBCO-Peg5-NHS Ester (linker; 10mM in DMSO; Click Chemistry Tools Cat: 1378531-80-6) in 60 molar excess (10 μg of antibody and 2.8 μg of linker) for 30 minutes at room temperature. Post-incubation, the excess linker is removed with Amicon Ultra 100 kDa molecular weight cut-off filters (Fisher Scientific Cat: UFC5100BK). The antibody-linker retentate is collected. Two oligo complexes are created using external (ext.) or internal (int.) fluorophore modifications.

For externally-modified oligos, a 20 bp oligo with a 5' fluorophore modification (5' donor strand) and a 20 bp oligo with a 3' fluorophore modification (3' acceptor strand) are co-hybridized to a 55 bp oligo with a 5' azide modification (docking strand) (Integrated DNA Technologies, Table 1) in a 1:1:1 ratio (0.4 nmol of each oligo) to form the ext. oligo complex.

For internally-modified oligos, a 15bp oligo with a 3' azide modification (azide strand) and a 50 bp oligo with an internal fluorophore modification (int. acceptor strand) are co-hybridized to a 65 bp oligo with an internal fluorophore modification (int. donor strand) (Integrated DNA Technologies, Table X) at a 1:1:1 ratio to one another (0.4 nmol of each oligo) to form the int. oligo complex.

For each, oligo mixtures are incubated for five minutes at room temperature in the dark to allow for complex formation. These complexes (0.4 nmol of each oligo) are then added to the antibody-linker retentate at a 6-molar excess to the original 10 ug of antibody. The volume is brought up to 100 μl with PBS and incubated at 4°C overnight in the dark.

Conventionally labeled antibodies are labeled as per the manufacturer's instructions (Biotium, Cat: 92446). In short, CD8 antibodies are covalently labeled with CF488A dyes using the Biotium mix-n-stain kit.

Preparing Peripheral Blood Mononuclear Cells

Normal Peripheral Blood Mononuclear Cells (PBMCs) (Precision for Medicine; 10M cells/vial) are thawed and counted with a hemacytometer. Cells are

washed twice with cold (4^{o}C) stain buffer (.01 g/ml BSA in PBS) at 300 x g for 5 min. Post-wash, the cells are resuspended in cold stain buffer and divided into 100 μl aliquots containing 10^6 cells.

Staining PBMCs

In order to block non-specific Fc-mediated interaction,1 μg of normal Rabbit IgG (ThermoFisher Cat: 31235) is added to the cell sample and incubated for 10 minutes at room temperature. Conventionally, ext., and int. labeled-antibodies are made for staining using the protocols described above (10μg of antibody each); (1) CD8 (clone RPA-T8; Biolegend Cat: 301002) labeled with Atto488 ext. MuSIC probes, (2) CD8 (clone RPA-T8; Biolegend Cat: 301002) labeled with Atto488 int. MuSIC probes, and (3) CD8 (clone RPA-T8; Biolegend Cat: 301002) labeled with CF488A (Biotium Cat: 92446), Antibody concentration is adjusted to 0.25 ug/ul for each sample. The labeled CD8 antibody is added to the cell sample at the appropriate amount as per manufactures recommendations (2μg CD8 antibody / 10^6 cells) and allowed to incubate in the dark for 20 minutes on ice. Post-incubation, cells are washed twice with 1ml of cold staining buffer at 300 x g for 5 min. The final cell pellet is resuspended in 0.5 ml of cold staining buffer.

Flow Cytometry

Stained PBMC samples are analyzed using a Cytek Aurora spectral flow cytometer. First, unstained PBMCs are assayed with the events to record set to

10,000. The SpectroFlo software (Cytek) is used to gate single cells (lymphocytes, monocytes, and granulocytes) by forward and side scatter. We then further gate specifically over the lymphocyte population, as typical based on light scattering distributions[184]. Using these same settings, the stained cell samples are assayed. To compare fluorescence intensity between stained samples we calculate the median intensity of the positively stained cells in the maximum emission channel (B2) using the Spectroflo software. Positively stained cells are defined as cells with a staining intensity above that of the unstained cell samples using a marker gate. To compare the compositions of CD8+ cells, we compare the positively stained population to the negative population of cells for each sample using the Spectroflo software.

Results

We previously developed a method for labeling antibodies with combinations of fluorophores (i.e MuSIC probes)[183]. In short, an oligo complex containing fluorescent molecules is conjugated to the antibody via a DBCO-Peg5-NHS ester (referred to as the linker) (**Fig 4.1A**). Here the oligo complex is composed of a 20 bp oligo with a 5' fluorophore modification (referred to as the 5' donor strand) and a 20 bp oligo with a 3' fluorophore modification (referred to as the 3' acceptor strand) that are co-hybridized to a 55bp oligo with a 5' azide modification (referred to as the docking strand) to form the externally labeled (ext.) oligo complex (**Fig 4.1B**). We previously demonstrated our ability to covalently label antibodies with MuSIC probes using this method and validated the labeling protocol with spin-column purification and absorbance measurements[183]. Furthermore, we validated our approach by creating ext. oligo complexes with (i) Cy3, (ii) Tex615, and (iii) a Cy3-Tex615 combination as three different MuSIC probes attached to three separate batches of antibodies. We created batches of stained beads, that are analogous to single cells, by incubating MuSIC-probe labeled antibodies with protein A beads. Using FSFC, we showed that each MuSIC probe can be uniquely distinguished in a mixture, and the fraction of beads in a mixture with different staining patterns can be accurately inferred.

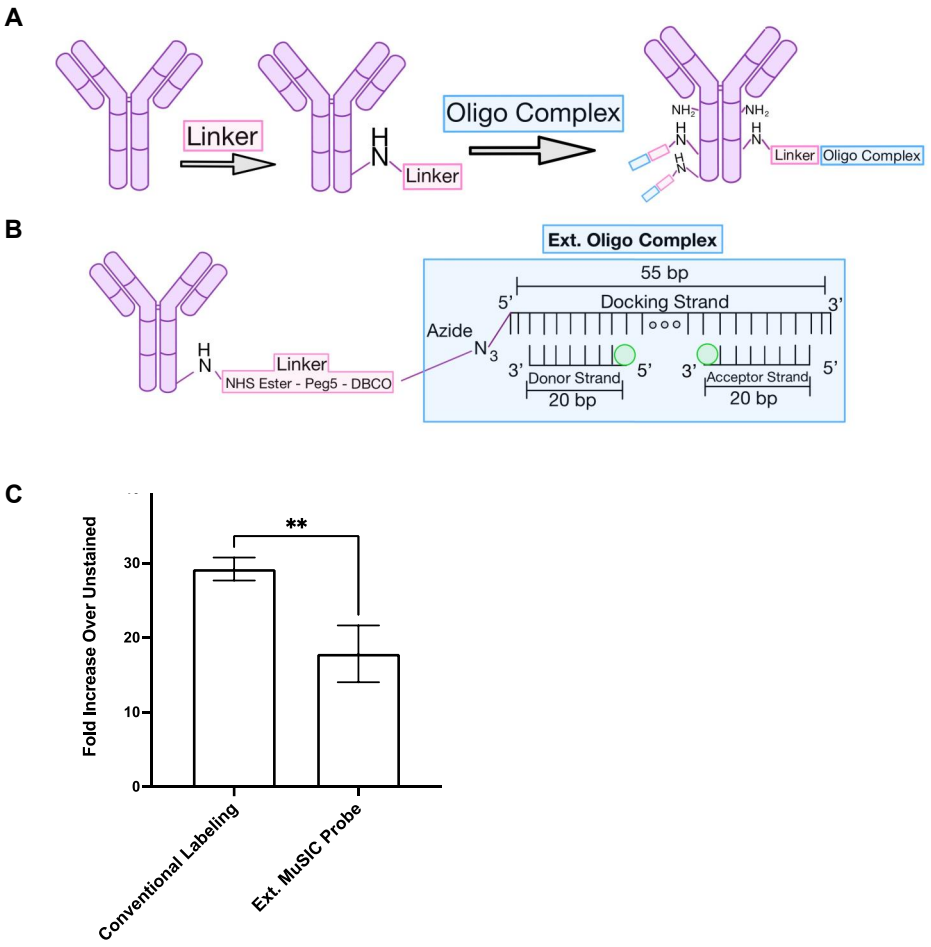

Figure 4.1: Oligo-based MuSIC probe labeling of antibodies. (A) Graphic depicting MuSIC probe labeling. By reacting the NHS ester of the linker with the NH_2 group of the antibody, the linker is attached. Subsequently, donor and acceptor strands are annealed onto the docking strand to form the oligo complex. The azide on the docking strand, in the oligo complex, is reacted with the free DBCO group on the linker to covalently bind the oligo complex to the antibody. There are multiple NH_2 sites on each antibody, allowing for the linker to attach at multiple sites, increasing the degree of labeling. (B) A more detailed depiction of the linker-oligo complex.

(C) Comparison of fluorescence intensity of PBMCs stained with CF488A conventional labeling kit vs Atto488 Ext. MuSIC probes. The fold increase in intensity over unstained cells is significantly greater for the conventional labeling kit compared to the ext. MuSIC probe.

Since this method had only been validated using beads, we asked whether this method would work when staining peripheral blood mononuclear cells (PBMCs)? We created an ext. oligo complex using an Atto488 5' donor strand and an Atto488 3' acceptor strand as the MuSIC probe and conjugated it to anti-CD8 antibodies. For comparison, we used a commercially available Biotium Mix-n-Stain kit to conventionally label CD8 antibodies with CF488A dye, which is reported to have comparable fluorescent properties (excitation peak, emission peak, and brightness) to Atto488[185]. PBMCs were stained with each antibody batch and analyzed on a Cytek Aurora flow cytometer. Results showed that the median signal intensity of cells stained with the ext. labeled MuSIC probe was ~1.6-fold (p-value=0.0086) lower compared to cells stained with conventionally labeled antibodies (**Fig 4.1C**).

We then asked how we can increase the signal intensity of MuSIC probes. We reasoned that because the previously calculated degree of labeling[183] was within the standard range[186], that the lower fluorescence signal was not due to the degree of labeling. We acknowledge that some degree of difference in signal intensity may be due to differences in dye properties between Cf488A and Atto488, although as mentioned above, the dyes are expected to have similar

characteristics. We then decided to examine the fluorescence emission intensity of Atto488 5' donor strands and Atto488 3' acceptor strands alone in solution and when co-hybridized to the docking strand (**Fig 4.2A**). Results showed that the hybridization of the 5' donor and 3' acceptor strands to the docking strand results in a significant decrease in fluorescent signal, as compared to the strands on their own (**Fig 4.2A**).

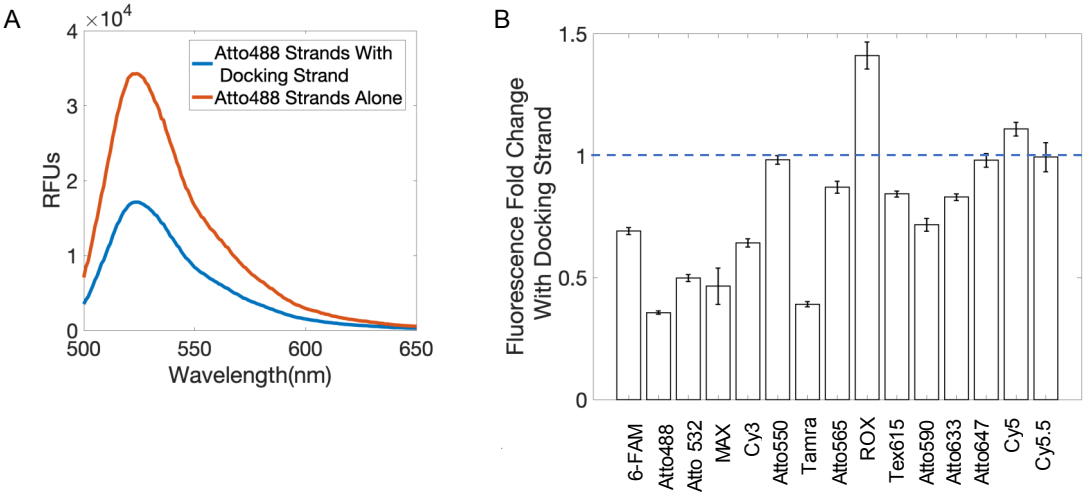

Figure 4.2: Fluorescence signal change from Docking Strand. (A) Comparison of fluorescence emission spectra, excited at 470nm, of the Atto488 5' Donor and 3' Acceptor strands hybridized to the Docking Strand and when alone in solution with and without the Docking Strand. (B) Change in fluorescence intensity of 15 fluorescent oligos when hybridized to the Docking Strand.

We further wondered whether this was a fluorophore-specific phenomenon or if it occurred for other fluorophores. Therefore, we examined the emission intensity of fluorophore-conjugated 5' donor strands and 3' acceptor strands for 15

different fluorophore-conjugated strands alone in solution and compared it to the emission intensity when co-hybridized to the docking strand (**Fig 4.2B**). Results show an observed decrease in signal for all but five of the fluorophore-conjugated strands that were tested. Previous studies showed that there can be a significant change in fluorescence when oligo-strands containing an end-fluorophore modification are hybridized to strands containing an overhang[187], such as in our ext. oligo complex.

These findings led us to hypothesize that a different orientation and interaction with the aqueous phase of the fluorophores within the oligo complex could give an increased fluorescent signal. To test this, we adjusted the configuration of the ext. oligo complex (**Fig 4.1B**) to contain oligos with internally (int) conjugated fluorophores. The resulting oligo complex consists of the 50 bp int. acceptor strand and a 15 bp azide strand which both co-hybridize to the 65 bp int. donor strand (**Fig 4.3A**). The purpose of a separate azide strand here is to reduce the cost of oligo production, due to the increased difficulty of synthesizing an oligo with two modifications. The new donor and acceptor strands both have an internal fluorophore modification (int donor and int acceptor), rather than 5' and 3' end fluorophore modification, respectively. We then created int. and ext. oligo complexes (both using Atto488 conjugated strands) and measured their fluorescent emission spectra. We observed a ~6-fold fluorescent signal increase of the int. oligo complex compared to the ext. oligo complex (**Fig 3B**).

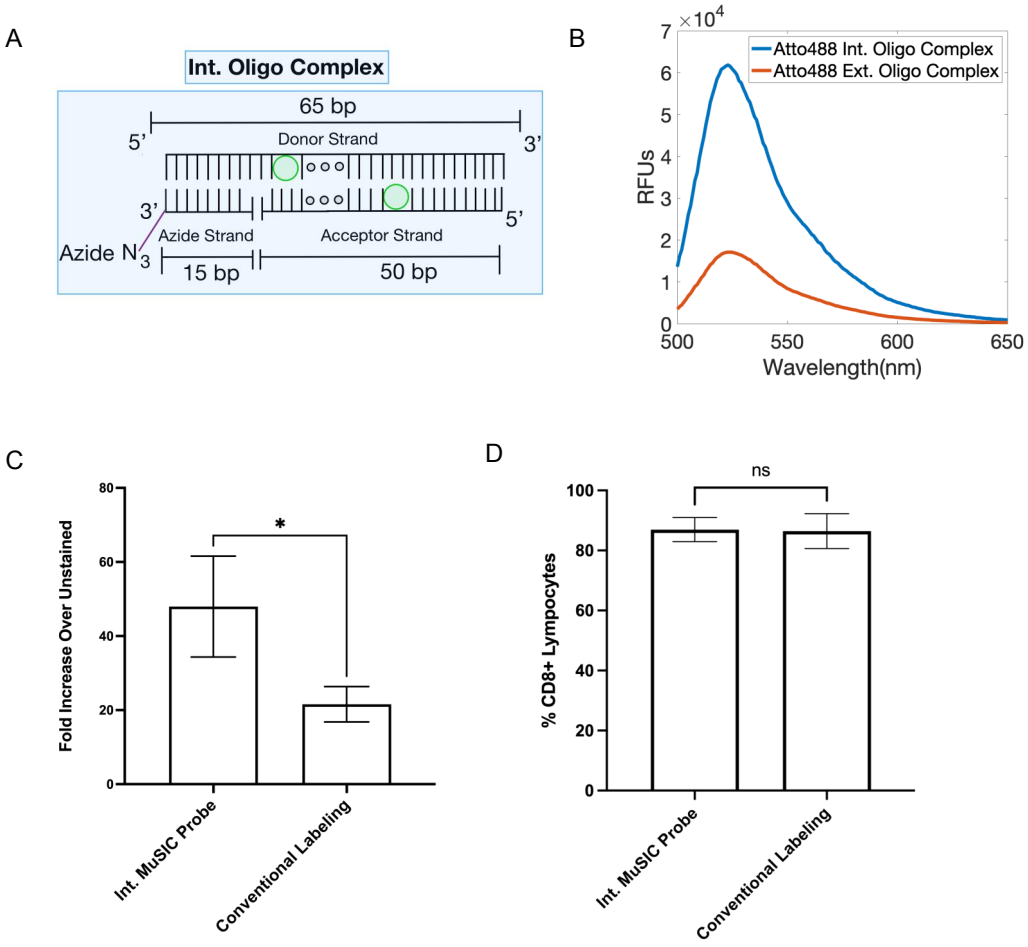

Figure 4.3: Comparison the Int. labeling method to the ext. labeling method and conventional labeling kit. (A) Int. oligo complex containing the Int. Donor and Acceptor strands and the Azide strand arranged to allow for increased fluorescence emission and fine control of Förster resonance energy transfer (FRET). (B) Comparison of relative fluorescent units of the Atto488 probe using the Int. and Ext. oligo complexes to compare their intensity when excited at 470nm. (C) Fold increase comparison of PBMCs stained with Atto488 Int. MuSIC probe-labeled CD8 antibodies and the CF488A conventional labeled- CD8 antibodies

over unstained PBMCs. (D) Percentage of CD8 + lymphocytes in PBMC for Int. Music probe-labeled CD8 antibodies compared to CF488A conventional-labeled CD8 antibodies.

With this increase in signal intensity, we then asked how new int. MuSIC probe-labeled antibodies would compare to conventionally labeled antibodies when staining PBMCs for estimation of specific cell type abundances. Similar to above, int. oligo complexes with Atto488 were conjugated to CD8 antibodies to create int. MuSIC probe-labeled antibodies and CF488A was conjugated to CD8 antibodies using a Mix-n-stain kit to create the conventionally labeled antibodies. PBMCs were stained with each antibody batch and analyzed on a Cytek Aurora flow cytometer. Results showed that the signal intensity of cells stained with the int. labeled MuSIC probe was ~2.5 fold (p-value=0.034) higher compared to cells stained with conventionally labeled antibodies (**Fig 3C**). When comparing the % of CD8+ lymphocytes detected, we found no significant difference between the int. MuSIC probe-labeled antibodies and conventionally labeled antibodies (**Fig 3D**). These results demonstrate that we were able to effectively improve the design of MuSIC-probe labeled antibodies to increase the signal-to-noise ratio, with staining behavior comparable to conventionally labeled antibodies.

Discussion

Here, we established a method to conjugate two fluorophores to an antibody and stain human cells with an increased signal intensity, compared to conventionally labeled antibodies, and accurate detection of % of CD8+ lymphocytes. This method builds on our previously established labeling protocol but introduces key modifications to the oligo-fluorophore arrangement of the MuSIC probe. By re-arranging the oligo complex of the MuSIC probe to eliminate the use of overhang sequences in the oligo complex, we observe a significant increase in fluorescent signal. Using this new MuSIC probe design, we stained human PBMCs and compared the signal intensity to that of conventionally labeled fluorescent antibodies using a spectral flow cytometer and observed a statistically significant increase in the resulting fluorescent signal without creating any significant differences in the % of CD8+ lymphocytes.

In order to maximize the potential of this new increased intensity probe design, the next step will be to select different combinations of fluorophores to assemble a palette of spectrally unique antibody-conjugated MuSIC probes. Approaches to do so can include stimulation studies for compatibility using a workflow similar to that described in our previous work[13], and then testing the highest-ranked fluorophore combinations experimentally. For these simulations, the emission spectra of each possible MuSIC probe is generated, and using the simulation workflow, lists of MuSIC probes that are likely to be deconvolvable in a mixture are generated, given binary classification applications. Using these lists of

potential good MuSIC probes, the probes would be prioritized for testing experimentally by measuring the emission spectra of mixtures of MuSIC probes and unmixing them to determine which MuSIC probes can be accurately demultiplexed.

One major application of using MuSIC probe-labeled antibodies with FSFC can be cell-type profiling, which is the process by which a complex mixture of cell types, for example, from blood or tumors, are classified into the fractional composition of its components (e.g., neutrophils, natural killer cells, various types of T and B cells, etc.), based on classification of expression patterns (e.g., CD3 expressed or not)[188]. While there are 40 dyes available, very few of them are tandem dyes that can be used as uniquely identifiable markers, which limits the number of individual analytes that can be classified simultaneously. However, MuSIC probe-labeled antibodies could be used to expand the number of markers that can be detected by creating new combination fluorophore probes from the current dyes, to enhance current cell-type profiling efforts. FSFC has been previously paired with cell-type profiling to investigate the correlation between CD38 expression in macrophages and the predicted immune response to immune-checkpoint blockade therapy for hepatocellular carcinoma[189]. With a larger palette of compatible fluorescent tags, cell-type profiling efforts could expand further to look at an increased number of cell-type markers, for a more comprehensive view of a patient's immune response to various treatments.

Additionally, MuSIC probe-labeled antibodies can be applied to a broad range of biological and diagnostic applications that involve the detection of protein expression. One of these applications can be for tissue imaging. If MuSIC probe-labeled antibodies can be combined with spectral imaging, this could allow for highly multiplexed, quantitative tissue imaging. Current immunostaining on biopsies can only provide data for a small portion of the tumor and cannot properly account for tumor heterogeneity _As such, increasing multiplexing capabilities would improve diagnostic potential from biopsies by allowing for more tumor markers to be analyzed, thus leading to an increased mapping of tumor heterogeneity[190]. This could impact early tumor detection, diagnosis, and treatment.

Although here we focused on increasing the fluorescent signal of MuSIC probes, by titrating the fluorescent oligos, we can decrease the fluorescent signal of MuSIC probes to a desired level in a highly controllable manner. Tunable fluorescence intensity is useful; for example, Pittman et al.[15] used MuSIC probes in static light scattering experiments, where the sensitive photodiode detectors are easily saturated. They labeled BSA at varying concentrations of fluorescent oligos between 0.03 - 0.10 μM that fluoresced below the saturation limit of the detectors while still achieving desired fluorescent effects. Conventional labeling kits would have been too powerful, and as most are single reaction use, using less than the recommended amount of labeling reagent is not cost-effective and difficult to control compared to MuSIC probes which offer the unique advantage of reduced,

tailorable intensities. In their case, the tunability of the MuSIC probes enabled a more flexible experimental design capable of separating simultaneous fluorescence and light scattering signals. The tunability of MuSIC probe fluorescent intensity could also be beneficial for cell staining, where some epitopes may have such a high abundance that a reduced fluorescent signal is necessary.

In addition to tunability for probe fluorescent intensity, the new int. oligo arrangement of MuSIC probes offers tunability of Förster Resonance Energy Transfer (FRET) between fluorophore combinations on the donor and acceptor strands. By adjusting the distance (bp) between the two fluorophores, we can increase or decrease the FRET efficiency. By adjusting the FRET efficiency of each combination, there is the potential to even further increase the number of possible compatible MuSIC probes.

We conclude that by using an oligo-based approach with internally-labeled fluorophores, we can increase the signal intensity of MuSIC-probe labeled antibodies. MuSIC probe-labeled antibodies may find useful to increase multiplexing capabilities of full spectrum flow cytometry, and also more broadly where increased multiplexing at single-cell or sub-cellular resolution is needed, including cell-type profiling, tissue studies, and immunofluorescence imaging.

CHAPTER FIVE

A THEORY FOR HIGH-THROUGHPUT GENETIC INTERACTION SCREENING

Abstract

Systematic, genome-scale genetic screens have been instrumental for elucidating genotype-phenotype relationships, but approaches for probing genetic interactions have been limited to at most ~100 pre-selected gene combinations in mammalian cells. Here, we introduce a theory for high-throughput genetic interaction screens. The theory extends our recently developed Multiplexing using Spectral Imaging and Combinatorics (MuSIC) approach to propose ~10^5 spectrally unique, genetically-encoded MuSIC barcodes from 18 currently available fluorescent proteins. Simulation studies based on constraints imposed by spectral flow cytometry equipment suggest that genetic interaction screens at the human genome-scale may be possible if MuSIC barcodes can be paired to guide RNAs. While experimental testing of this theory awaits, it offers transformative potential for genetic perturbation technology and knowledge of genetic function. More broadly, the availability of a genome-scale spectral barcode library for non-destructive identification of single-cells could find more widespread applications such as traditional genetic screening and high-dimensional lineage tracing.

Introduction

Understanding which genes play essential roles in a cellular or organismal process is crucial to our understanding of biology[191]. This can be accomplished by perturbing genes and observing the corresponding phenotype alterations[192]. This process, when applied in parallel to multiple genes one-at-a-time, is known as genetic screening[193,194195–198]. Historically, there have been several methods for performing genetic screens, including Zinc finger nucleases (ZFNs) and transcription activator-like effector nucleases (TALENs) which are engineered nucleases that induce DNA DSBs at specific locations[199,200], RNAi which uses double stranded RNAs (or a short hairpin (sh)RNA) to knock down the gene-of-interest[201], and CRISPR which induces DNA breaks or alters transcription at specific sites in the genome[202,203 205].

While these gene perturbation technologies have revolutionized biomedical science, most genome-scale screens (outside of organisms like *S. cerevisae*[206]) remain limited to one gene at a time[207]. However, often genes cooperate with one another to influence phenotype. Such cooperation is called genetic interaction[208–211]. Recent approaches have made progress towards larger scale genetic interaction screening. For example, cloning two different CRISPR gRNAs into a single plasmid enables interaction screening for ~100 pre-selected genes [209,215–217]. Other approaches include dual recombinase-mediated cassette exchange to create mosaic *in vivo* models harboring multiple desired cancer driver mutations[218], or using protein epitope combinatorial barcodes (pro-codes) with mass cytometry

to perform high-dimensional CRISPR screens on 100s of selected genes in single cells[219]. The sheer number of observations that must be made to cover human gene interactions space almost necessitates a single-cell approach, like Perturb-seq[220–222]. However, genetic interaction screening approaches that scale past ~100 genes have yet to be described.

Here, we propose that our recently developed fluorescence **mu**ltiplexing with **s**pectral **i**maging and **c**ombinatorics (MuSIC)[21] approach may be compatible with single cell genetic interaction screening that could scale to the full human genome. MuSIC uses combinations of fluorophores (proteins or small molecules) to create spectrally unique MuSIC probes. Here we introduce the concept of further combining MuSIC probes into MuSIC barcodes for increased diversity and thus multiplexing. Moreover, because these spectral barcodes are fluorescence-based, they can be read non-destructively. Theory and simulations based on currently available fluorescent proteins suggests that given a palette of 18 fluorescent proteins, ~400,000 MuSIC barcodes could be generated, far surpassing human genome-scale. Simulations suggest that given current spectral flow cytometry equipment and experimental noise, human genome-scale genetic interaction screens may be possible. More advanced instrument hardware such as more excitation lasers and/or higher resolution emission spectra could increase such capabilities. While experimental testing of this theory awaits, it offers transformative potential for genetic perturbation technology and knowledge of genetic function. More broadly, the availability of a genome-scale spectral library

for non-destructive cell identification could find more widespread applications such as traditional genetic screens and high-dimensional lineage tracing.

Methods

Availability, Code Overview, and Simulation. All MATLAB code and raw data used for simulations are open source on Zenodo. DOI: https://doi.org/10.5281/zenodo.7186939. The scripts `GenerateProbeData_3l_HN.m`, `GenerateProbeData_3l_LN.m`, `GenerateProbeData_5l_HN.m`, and `GenerateProbeData_5l_LN.m` are used for generating the list of good probes for single probes, barcodes, and two barcodes, for 3 lasers/high noise (HN), 3 lasers/low noise (LN), 5 lasers/high noise, and 5 lasers/low noise respectively. The core of these scripts is done by the functions `RemoveProbes_onebyone.m`, `RemoveBarcodes_onebyone.m`, and `RemoveTwoBarcodes_onebyone.m`, respectively. The README file contains relevant information on the code for execution and reproducing the results. These simulations were performed in MATLAB using 40 CPUs on the Palmetto supercomputing cluster at Clemson University.

Data Sources. Emission spectra, excitation spectra, and brightness for fluorescent proteins were gathered from *fpbase.org* (**Supplementary Table 5.1** and references therein). Specifications for flow cytometer noise, excitation channels, and emission binning were obtained from the Aurora and Northern Lights flow cytometer user guides on *cytekbio.com*.

Simulated FRET Efficiency and MuSIC Probe Selection. FRET efficiency ε between two fluorophores is typically calculated as follows

$$\varepsilon = \frac{1}{1 + \left(\frac{r}{R_0}\right)^6}$$

(1)

where *r* is the distance between the two fluorophores and R_0 is the Förster radius[223]. The Förster radius is the distance between fluorophores that gives a 50% FRET efficiency[223]. Thus, to estimate the FRET efficiency between any given pair of fluorescent proteins, we must calculate R_0 and *r*.

The Förster radius can be cast as follows[224]

$$R_0 = [\beta * \mathrm{K}^2 * Q_D * e_A * J]^{\frac{1}{6}} nm$$

(2)

where β is a constant (which also converts to nm), K^2 is an orientation factor between the two fluorophores, Q_D is the donor quantum yield, e_A is the maximal acceptor extinction coefficient ($M^{-1*}cm^{-1}$), and *J* is the spectral overlap integral. The value of K^2 is not usually known (nor easily measurable) but is assumed to be a constant value of 2/3 for isotropic reorientation of the coupled fluorophores [225]. This value may not be 2/3 for fluorescent protein tandems but in practice, deviations can be accounted for by the constant β[226]. J is calculated as follows

$$J = \int F_D(\lambda) E_A(\lambda)\, \lambda^4 d\lambda$$

(3)

where F_D is the normalized emission spectra of the donor and E_A is the normalized excitation spectra of the acceptor, which both are evaluated at wavelength λ. Here, the spectral data is normalized to have a maximum value of 1. We calculate the overlap integral using the function `trapz` in MATLAB (see code) with bounds from λ = 300 to 800 nm. The value for β is estimated to be $6.33*10^{-6}$ based on a known Förster radius of 6.1 nm for mTFP-Venus[227] (along with known Q_D, and e_A, and J calculated as above).

The closest physical distance that chromophores of fluorescent proteins can be is ~3 nm[228]. Furthermore, most high FRET producing pairs have an R_0 greater than 5 nm[229]. Thus, we do not consider MuSIC probes that have R_0 < 5 nm. Since the distance between fluorescent proteins can usually be adjusted (by linker length, for example), we set $r = R_0$ in simulations, giving a FRET efficiency of 50% for each MuSIC probe with more than one fluorescent protein.

Simulating Reference Emission Spectra for MuSIC probes. There are three classes of MuSIC probes that require separate consideration for simulating their emission spectra: those made of a (i) single fluorescent protein, (ii) two fluorescent proteins, and (iii) three fluorescent proteins. The below equations are used to generate columns of the reference matrix **R** (see below) for unmixing. Each simulated spectra for a single excitation channel has a value every nm from 300 to 800 nm. The below model assumes that tandem fluorescent proteins have the same properties as the monomers, that static quenching is not a dominant feature,

and that fluorescent protein maturation is not a significant factor for the spectra. We assume cross-talk is negligible, but for all intents and purposes, it would be observed as effective FRET-related activity and therefore is expected to not have additional functional consequences for simulation results. We also note here that this model does not take into account detector quantum efficiency. Avalanche Photodiode (APD) detectors (used in the Cytek instruments) generally have slightly lower quantum efficiency in the lower wavelengths (UV/Blue), but so long as all reference spectra and samples are measured with the same instrument, this would not introduce any further bias and not affect the conclusions drawn here.

To simulate the emission intensity spectra *I* for a single fluorescent protein MuSIC probe, given a particular excitation wavelength (λ_{ex}) and vector of emission wavelengths from 300 to 800nm at every nm ($\boldsymbol{\lambda}$), the following equation is used (adapted from Schwartz et. al)[230]

$$I(\boldsymbol{\lambda}) = E(\lambda_{ex}) * C * B * F(\boldsymbol{\lambda}) \quad (4)$$

Where *E* is the fraction of excited fluorophores and is a function of excitation wavelength (explained below), *C* is the relative probe concentration (taken as 1 for reference spectra assuming a null condition of equal expression levels between probes), *B* is the brightness (product of maximal extinction coefficient and quantum yield), and *F* is the normalized emission spectra vector of the fluorescent protein (normalized as above). $E(\lambda_{ex})$ is given by the fluorescent protein's normalized excitation spectra at the designated excitation wavelength.

For MuSIC probes with two fluorescent proteins, called 1 and 2 ordered from blue to red, the emission intensity spectra $I(\boldsymbol{\lambda})$ has three contributing components: acceptor emission due to FRET ($I_{2,1}$), donor emission (I_1), and acceptor emission due to direct excitation (I_2). The overall emission intensity spectra I is the sum of the three components

$$I = I_{2,1} + I_1 + I_2$$

(5)

Each of these terms depends on the FRET efficiency. We assume that FRET efficiency is reduced due to any direct acceptor (2) excitation, since excited acceptors would not be able to undergo FRET. This adjusted FRET efficiency, ε_{adj}, is calculated as follows

$$\varepsilon_{adj} = \varepsilon * \left(1 - E_2(\lambda_{ex})\right)$$

(6)

where E_2 is the fraction of excited fluorophores for fluorescent protein 2 and the term (1-E_2) denotes the fraction of fluorescent protein 2 molecules that have not been directly excited.

Fluorescent protein 2 emission due to FRET from fluorescent protein 1 is then calculated by

$$I_{2,1}(\boldsymbol{\lambda}) = E_1(\lambda_{ex}) * \varepsilon_{adj} * C * B_2 * F_2(\boldsymbol{\lambda})$$

(7)

This emission intensity is proportional to emission properties of fluorescent protein 2 (emission spectra and brightness), the fraction of excited molecules for

fluorescent protein 1, and the adjusted FRET efficiency between the two fluorescent proteins.

Fluorescent protein 1 emission is calculated by

$$I_1(\boldsymbol{\lambda}) = E_1(\lambda_{ex}) \ * (1 - \varepsilon_{adj}) * C * B_1 * F_1(\boldsymbol{\lambda})$$

(8)

This emission is calculated similarly to that above for a single fluorescent protein; however, it is corrected to only take into account the fraction of excited molecules that are not undergoing FRET $(1 - \varepsilon_{adj})$.

Fluorescent protein 2 emission due to direct excitation is calculated by

$$I_2(\boldsymbol{\lambda}) = E_2(\lambda_{ex}) * \left(1 - \varepsilon_{adj}\right) * C * B_2 * F_2(\boldsymbol{\lambda})$$

(9)

We opt here to be conservative and reduce the amount of fluorescence from direct excitation of fluorescent protein 2 by the FRET taking place.

For MuSIC probes with three fluorescent proteins, called 1, 2, and 3 ordered from blue to red, the emission intensity depends on six different components. Three are due to direct excitation: emission intensity of fluorescent protein 1 (I_1), emission intensity of fluorescent protein 2 (I_2), and emission intensity of fluorescent protein 3 (I_3). The other three are due to FRET: FRET sensitized emission intensity of fluorescent protein 2 due to FRET with fluorescent protein 1 ($I_{2,1}$), FRET sensitized emission intensity of fluorescent protein 3 due to FRET with fluorescent protein 2 that ultimately came from FRET with fluorescent protein 1 ($I_{3,1}$), and FRET sensitized emission intensity of fluorescent protein 3 due to FRET with fluorescent

protein 2 ($I_{3,2}$). The overall intensity is calculated as the sum of the six intensities. We assume negligible direct FRET from fluorescent protein 1 to 3.

$$I = I_1 + I_2 + I_3 + I_{2,1} + I_{3,1} + I_{3,2}$$

(10)

The adjusted FRET efficiencies between fluorescent proteins, ε_{adj1} and ε_{adj2}, are calculated as above

$$\varepsilon_{adj_1} = \varepsilon_1 * \left(1 - E_2(\lambda_{ex})\right)$$

(11)

$$\varepsilon_{adj_2} = \varepsilon_2 * \left(1 - E_3(\lambda_{ex})\right)$$

(12)

The emission intensity of fluorescent protein 1 due to direct excitation is calculated by

$$I_1(\boldsymbol{\lambda}) = E_1(\lambda_{ex}) \ * (1 - \varepsilon_{adj1}) * C * B_1 * F_1(\boldsymbol{\lambda})$$

(13)

This emission is calculated similarly to that above and is corrected to only consider the fraction of excited fluorescent protein 1 molecules that are not undergoing FRET with fluorescent protein 2.

The emission intensity of fluorescent protein 2 due to direct excitation is calculated by

$$I_2(\boldsymbol{\lambda}) = E_2(\lambda_{ex}) \ * (1 - \varepsilon_{adj_1} - \varepsilon_{adj_2}) * C * B_2 * F_2(\boldsymbol{\lambda})$$

(14)

This emission is corrected to only consider the fraction of excited fluorescent protein 2 molecules that are not undergoing FRET with either fluorescent proteins 1 or 3.

The emission intensity of fluorescent protein 3 due to direct excitation is calculated by

$$I_3(\boldsymbol{\lambda}) = E_3(\lambda_{ex}) * \left(1 - \varepsilon_{adj_2} - \varepsilon_{adj_1} * \varepsilon_{adj_2}\right) * C * B_3 * F_3(\boldsymbol{\lambda})$$

(15)

This emission intensity only considers the fraction of fluorescent protein 3 molecules that are not involved in FRET with either fluorescent protein 2 or FRET from the first fluorescent protein through the second.

The emission intensity of fluorescent protein 2 due to FRET from fluorescent protein 1 is calculated by

$$I_{2,1}(\boldsymbol{\lambda}) = E_1(\lambda_{ex}) * \varepsilon_{adj_1} * C * B_2 * F_2(\boldsymbol{\lambda})$$

(16)

The emission intensity of fluorescent protein 3 due to FRET from fluorescent protein 1 through fluorescent protein 2 is calculated by

$$I_{3,1}(\boldsymbol{\lambda}) = E_1(\lambda_{ex}) * \varepsilon_{adj_1} * \varepsilon_{adj_2} * C * B_3 * F_3(\boldsymbol{\lambda})$$

(17)

Finally, the emission intensity of fluorescent protein 3 due to FRET from fluorescent protein 2 is calculated as follows

$$I_{3,2}(\boldsymbol{\lambda}) = E_2(\lambda_{ex}) * \varepsilon_{adj_2} * C * B_3 * F_3(\boldsymbol{\lambda})$$

(18)

Calculating the Observed Spectra Using Cytek Binning. The emission spectra of the MuSIC probes are simulated at every nm as described above. To best replicate the emission spectra generated from the Cytek Northern Lights and the Cytek Aurora flow cytometers, we condensed the simulated emission spectra based on the emission channels for each instrument, referred to as binning. Each emission channel represents spectral data condensed over a range of wavelengths, so to convert the simulated emission spectra (which is at every nm) we averaged the simulated emission spectra *I* for each probe over the wavelength ranges of each instrument's emission channels. Each binned emission point is calculated as follows

$$f_j = \frac{\sum_i I_{ji}}{n_j}$$

(19)

Where f_j is the binned emission point over the wavelength range for channel *j*, *n* is the number of wavelengths in channel *j*, and *I* is calculated as above.

Noise Model. Noise is assumed to be normally distributed and simulated using the MATLAB function `randn`. The standard deviation for the normal distribution is estimated based on data from the Cytek Northern Lights flow cytometer, given by the manufacturer, which is estimated at 50 relative fluorescent units (RFUs) for an intensity of 10^5 RFUs. In the above simulations, the fluorescence emission spectra have an average maximum of ~10 RFUs. The standard deviation of 50 is thus decreased by a factor of 10^4 to adjust for the

simulated emission spectra, giving a standard deviation of 0.005 for noise. This value is used as the value for “low” noise. The standard deviation is set to 0.05 for “high” noise (10-fold higher than the low noise).

Unmixing. The fluorescence emission spectra of a mixture of fluorophores can be cast as a sum of the emission spectra of the individual fluorophores as follows.

$$\boldsymbol{\mu} = \boldsymbol{R} \cdot \boldsymbol{c} \quad (20)$$

Where $\boldsymbol{\mu}$ is an *n-by-1* vector of observed fluorescence emission intensity at *n* emission wavelength/excitation channel combinations, **R** is an *n-by-m* reference matrix that is generated from the simulated emission spectra of *m* individual probes with multiple excitation channels as described above, and ***c*** is an *m-by-1* vector containing the relative probe concentrations.

Solving this equation gives an estimate of the relative probe concentrations, ***c***. This is done using the MATLAB function `lsqlin`. The lower bound for elements of ***c*** is set to zero, and the upper bound is left empty.

Generating a Simulated Experimental Data Set. Simulated data are generated by first specifying the relative probe concentrations for different mixtures of MuSIC probes. This is referred to as the actual mixture composition vector, $\mathbf{c_a}$.

For single probe mixtures, one probe concentration is set to 1 and all others are zero. For barcode mixtures, two probe concentrations are set to 1, and all others are zero. For two barcode mixtures, four probe concentrations are set to 1, and all others are zero. For the case of variable probe expression levels, probe concentrations are set to a random number between 0.5-1.5 (`rand`). For two barcode mixtures, the probes are divided into two batches, and two probes are chosen from the first batch while two are chosen from the second (see Results). Equation 20 with $\mathbf{c_a}$ and **R** is used to calculate $\boldsymbol{\mu_a}$, the simulated emission spectra of the mixture. Experimental noise is then added to the simulated emission spectra at either low or high levels, as described above, giving $\boldsymbol{\mu_n}$, the simulated observed spectra. Finally, Equation 20 is used to solve for **c** (i.e., unmixing), giving the predicted mixture composition, $\hat{\mathbf{c}}$.

Binary Classification. Binary classification is performed on the predicted mixture composition vector by converting the relative level for each probe to a one or zero based on a threshold for each probe. The threshold for each probe is determined as that which gives the maximum Matthews Correlation Coefficient value for each probe respectively based on simulation data (see below).

Confusion Matrix and Matthews Correlation Coefficient (MCC). Evaluating binary classification performance requires the calculation of a confusion matrix, which serves as a centralized table that tracks the number of true and false positive

and negative classifications. The confusion matrix allows for the calculation of a multitude of performance metrics and is calculated using the MATLAB function `confusionmat.m`. Out of these different metrics, the Matthew's Correlation Coefficient (MCC), or phi coefficient, was chosen to quantify the performance of probes in the simulations. The MCC was chosen because it is appropriate when the classes are highly imbalanced[231], such as what we have here when there are many more true negatives than true positives. Other metrics, such as the F1 score or Accuracy, are problematic for situations where there might be significantly more true negatives than false positives.

Given a classification threshold to evaluate, a confusion matrix is generated for each probe using the actual mixture compositions and the binary predicted probe concentrations for each probe. These confusion matrices are used to generate an individual MCC score for each probe, given the threshold. The threshold is then varied to determine the optimum threshold to maximize MCC for a particular probe.

A confusion matrix is generated for the entire group of probes using a matrix of all concatenated actual mixture composition vectors and a matrix of all concatenated predicted mixture composition vectors. This confusion matrix is used to generate the overall MCC score which represents the performance for the entire group of probes.

Results

This paper explores a theory for creating a large library of genetically-encoded, fluorescence spectral barcodes for potential application to genetic interaction screening. It is based on our recently published Multiplexing using Spectral Imaging and Combinatorics (MuSIC) approach[21], which creates unique spectral signatures from stably-linked combinations of individual fluorophores. The individual fluorophores or combinations are called MuSIC probes. In this work, we consider expanding the number of fluorophores used by fusing 2 or 3 individual fluorophores that would give rise to unique spectral properties. The spectral signatures of combination probes are linearly independent (i.e., unique) from the individual fluorophore spectra comprising the combination so long as sufficient Förster resonance energy transfer (FRET) occurs. This linear independence property allows for the estimation of individual MuSIC probe levels when they are together in a mixture, a process often called “unmixing”.

We selected 18 fluorescent proteins (see Methods and **Table 5.S1**) that span the ultraviolet to infrared spectrum and first wanted to determine how many MuSIC probes could be generated. The quality of unmixing depends on the FRET efficiency, which is directly related to the Förster radius and the physical distance between chromophores of the fluorescent proteins (see Methods). The distance between fluorescent proteins can usually be adjusted by altering the length and nature of the peptide fusion linker; thus, the answer to this question depends on the Förster radius chosen as acceptable (**Fig 5.1A-B**). Since high FRET producing

pairs usually have a Förster radius greater than 5 nm[229], we only consider MuSIC probes that have an estimated Förster radius greater than 5 nm. At this cutoff, 910 MuSIC probes can be generated (**Table 5.S2**), but this is far from genome-scale. We should also note here that in principle the same fluorescent proteins in a probe could be engineered to be a different distance apart and thus a different FRET efficiency, which would increase the number of probes. However, for the purposes of this work, we only consider one FRET efficiency (~50%) per probe.

Can we develop another layer of combinatorics to generate further diversity? Consider the concept of a MuSIC barcode that is a combination of MuSIC probes. As an example, let us start with two fluorescent proteins, mAmetrine and mOrange2. From these two fluorescent proteins we can create three MuSIC probes: a single fluorescent protein probe of mAmetrine, the combination probe of mAmetrine and mOrange2, and another single fluorescent protein probe of mOrange2. A MuSIC barcode is then every 2-way combination of the probes. Thus, from these probes we can create three MuSIC barcodes **(Fig 5.1C-D)**. The MuSIC barcode spectra are clearly unique from one another. The number of barcodes that can be generated given a particular number of probes is given by combinatorics (see Methods); 910 probes gives 413,595 barcodes (**Fig 5.1B, E**).

This barcode diversity far exceeds the number of genes in the human genome (**Fig 5.1E**). If each MuSIC barcode could be paired to a guide RNA (gRNA), and if resolvable in practice, one could perform genome-scale genetic screening that is non-destructive in single cells. Specifically, then if a certain MuSIC barcode is

detected in a particular cell (via a fluorescence emission spectra measurement), that would indicate the gRNA that was present, and therefore the target gene that was likely modulated in that cell.

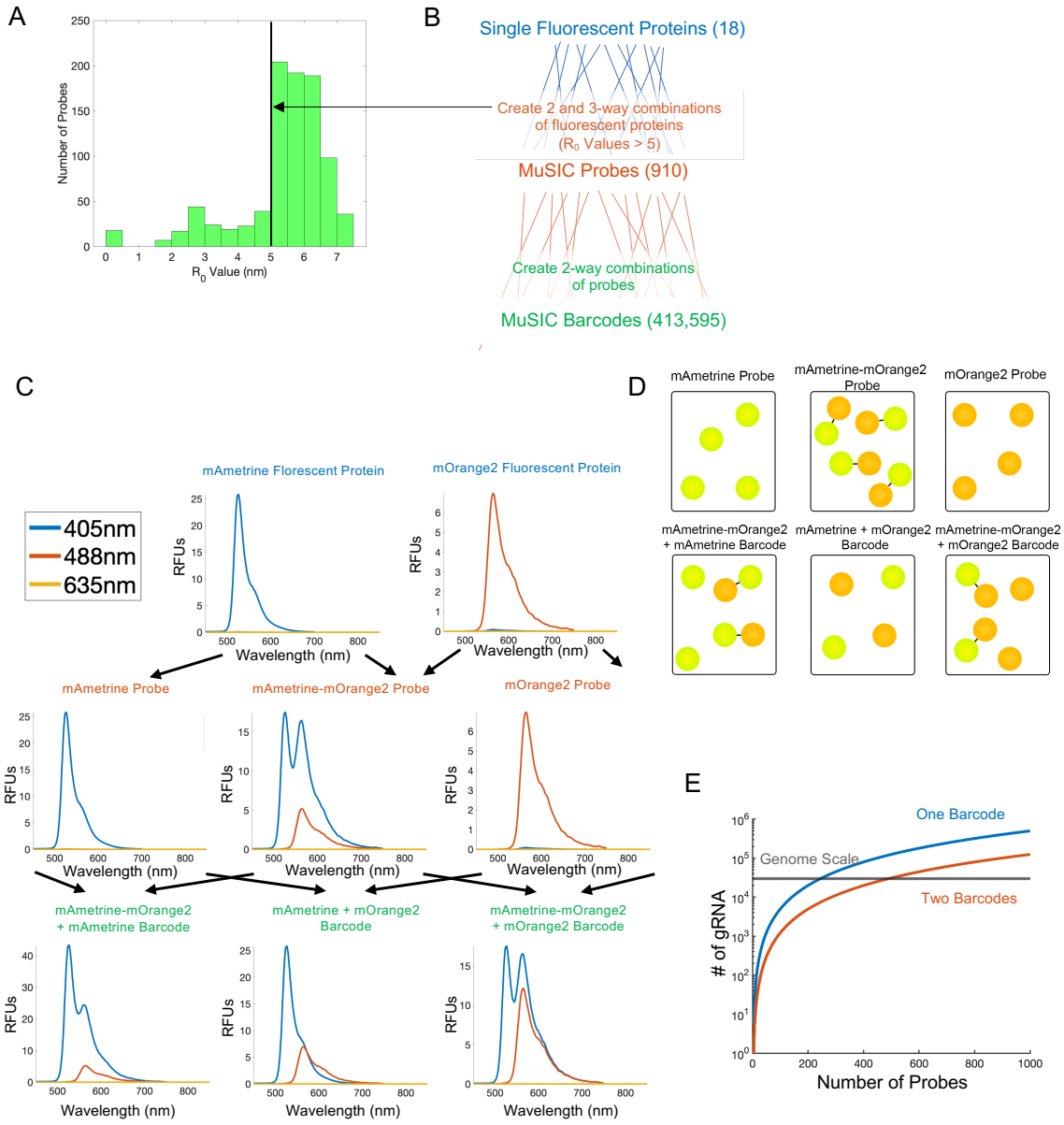

Figure 5.1: Theory and scope of MuSIC Barcodes for genetic and genetic interaction screening. (A) Forster Radius (R_0) cut off for probe selection. From the

total list of possible MuSIC probes (987), only probes with an R_0 value greater than 5nm (910) are selected as potentially good probes. (B) Potential number of MuSIC probes and barcodes. Given 18 fluorescent proteins, 910 MuSIC probes can be created (with an R_0>5nm), and given 910 MuSIC probes, 413,595 MuSIC barcodes could be created. (C) Example emission spectra of MuSIC probes and barcodes when excited at 405, 488, and 635nm. Given the fluorescent proteins mAmetrine and mOrange2, three MuSIC probes can be created that are spectrally unique. Given these three MuSIC probes, three MuSIC barcodes can be created. (D) Schematic showing the creation of MuSIC probes and barcodes from single fluorescent proteins. (E) Genetic and genetic interaction screening capabilities given the number of MuSIC probes that can be created.

MuSIC barcodes may also enable large-scale genetic interaction screening (**Fig 5.1E**). Consider that a gRNA is paired to a MuSIC barcode as above, but instead there are two MuSIC barcodes in a cell corresponding to two specific gRNAs. This means four MuSIC probes would be present in the cell. To avoid mapping ambiguity from probes to barcodes to gRNA, the MuSIC probe library would have to be split in half before linking gRNA with MuSIC barcodes, which makes the predicted scale of genetic interaction screening lower than that of genetic screens. With 910 MuSIC probes, 103,285 gRNA could be studied for genetic interactions, which approaches human genome-scale genetic interaction screening at ~3x redundancy.

While the above suggests MuSIC barcodes may enable novel genetic screening technology, how well might it work in practice? Of the 910 potential probes, how many can reliably be identified from expected mixtures? To constrain the answer to this question, we developed a simulation workflow. Rapid measurement of fluorescence emission spectra in single cells has recently become possible with Cytek flow cytometers. For this reason, we have based the simulation studies described in this paper off the Cytek Northern Lights Flow Cytometer (3 lasers; 405, 488, and 635nm) and the Cytek Aurora Flow Cytometer (5 lasers; 356, 405, 488, 561, and 635nm) **(Fig 5.2A)**. The spectral emission bin structure for each instrument and its signal-to-noise ratio is known and we incorporate such information into our simulated measurements (**Fig 5.2A—**see also Methods). For genetic screens, it can be useful to reserve one excitation channel to measure an observed phenotype. Therefore, we also investigated a setup for 2 lasers (Northern Lights, dedicating the 635nm laser to a phenotype) and 4 lasers (Aurora, dedicating 635nm laser to phenotype) **(Fig 5.2B**).

We implemented the following simulation strategy to eliminate “poorly” performing probes from consideration **(Fig 5.3A).** A “poorly” performing probe is one that leads to at least one misclassification event in simulations. At the core of the algorithm is a simulated MuSIC probe mixture. This is a vector that represents which probe or probe(s) are present in the ground truth, which we call the actual mixture composition. Using the actual mixture composition vector and the calculated reference matrix (see Methods—spectra of individual probes), we can

calculate the emission spectra of the mixture. We add low or high noise (see Methods—based on Cytek flow cytometer specs) to the emission spectra of the mixture, generating the simulated observed spectra. After noise is added, we perform linear unmixing, which generates the predicted mixture composition. To compare the predicted mixture composition to the actual mixture composition, we first perform binary classification (see Methods). To quantify performance, we calculate the Matthews correlation coefficient, which is suitable for cases such as this where there are many more true negatives than true positives. If overall classification is not perfect (MCC < 1), then we identify which probe has the worst MCC, and remove it. The simulation is repeated until overall classification is perfect **(Fig 5.3B)**, at which point we obtain the final list of good probes (**Table 5.S2**). This process is performed in triplicate.

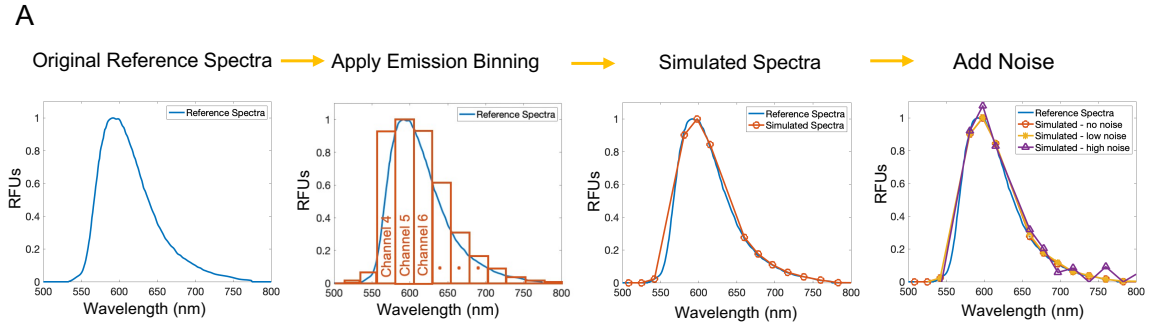

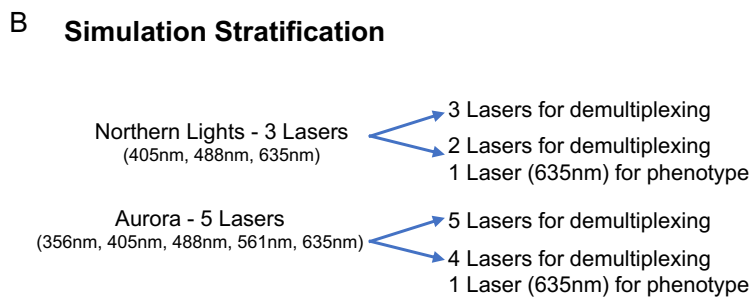

Figure 5.2: Simulation setup. (A) Simulating emission spectra. Process of condensing the original emission spectra at every nm according to the emission binning and noise of the simulated instrument. (B) Cases for the simulation experiment setup based on Cytek flow cytometers.

We use three sequential sets of simulations to determine a list of "good" MuSIC probes that can be used (1) on their own, (2) for MuSIC barcodes (genetic screening), and (3) for two MuSIC barcodes (genetic interaction screening) (**Table 5.S2**). The final list that is obtained in Simulation 1 is used for Simulation 2, and likewise 2 for 3 (**Fig 5.3C**). For example, only probes that are good for use on their own are considered for MuSIC barcodes. The list of "good" MuSIC probes from Simulation 2 sets constraints on genetic screening for single gene effects and the list of good MuSIC probes from Simulation 3 sets constraints on genetic interaction screening.

The results of this process are summarized in **Table 5.1.** The final number of good MuSIC probes that can be unmixed with perfect classification for MuSIC barcodes and sets of two MuSIC barcodes are listed for each of the experimental setups (summarized in **Fig 5.2B**). We found reasonable overlap between which probes were labeled as good between replicate runs (**Fig 5.S1**), although the overall number of probes seems to be a more reproducible and larger factor (**Table** 5.**1**). Given these results, the number of gRNA that can be used for genetic and genetic interaction screening are calculated from **Fig 5.1E**. In general, more lasers and lower noise allows for more probes and barcodes, as expected. For genetic

screens, each scenario investigated suggested potential for genome-scale operation. For genetic interaction screens, 4 and 5 laser setups with low noise predicted operation at genome-scale. Even 2 and 3 laser setups with high noise predicted operation with 1000s of gRNA in genetic interaction screens, an order of magnitude above current methods. If we consider typical ranges of cell-to-cell variability in probe expression levels, then we can still generate gRNA on the same scale (**Table 5.S3**). If we only consider MuSIC probes with one or two fluorescent proteins, as opposed to three, we can still achieve multiple hundred gRNA for genetic interaction screens (**Table 5.S4**). Overall, these results suggest MuSIC barcoding theory represents a promising approach to transforming genetic perturbation technology.

Table 5.1: Simulated number of gRNA that could be used for genetic and genetic interaction screens. Results for the number of good probes for barcodes and pairs of barcodes are shown for each experimental setup. Given the number of good probes, the number of potential gRNA for genetic and genetic interaction screens

			# of Good Probes		# of gRNA	
Experimental Setup	# Laser	Noise	One Barcode	Two Barcodes	Genetic Screen	Genetic Interaction Screen
Cytek Northern Lights	3	high	337±3	113±5	56737±1001	1565±146
	3	low	634±5	230±11	200897±3149	6544±610
	2	high	292±8	92±5	42458±2445	1024±101
	2	low	550±25	175±12	151970±14008	3805±528
Cytek Aurora	5	high	666±15	294±7	221893±10020	10694±510
	5	low	894±3	708±12	399477±2596	62397±2046
	4	high	580±9	252±10	167983±4916	7860±654
	4	low	879±2	590±11	385885±1755	43294±1535

is listed. Results for the Cytek Northern Lights flow cytometer are highlighted in blue and results for the Aurora flow cytometer are highlighted in yellow.

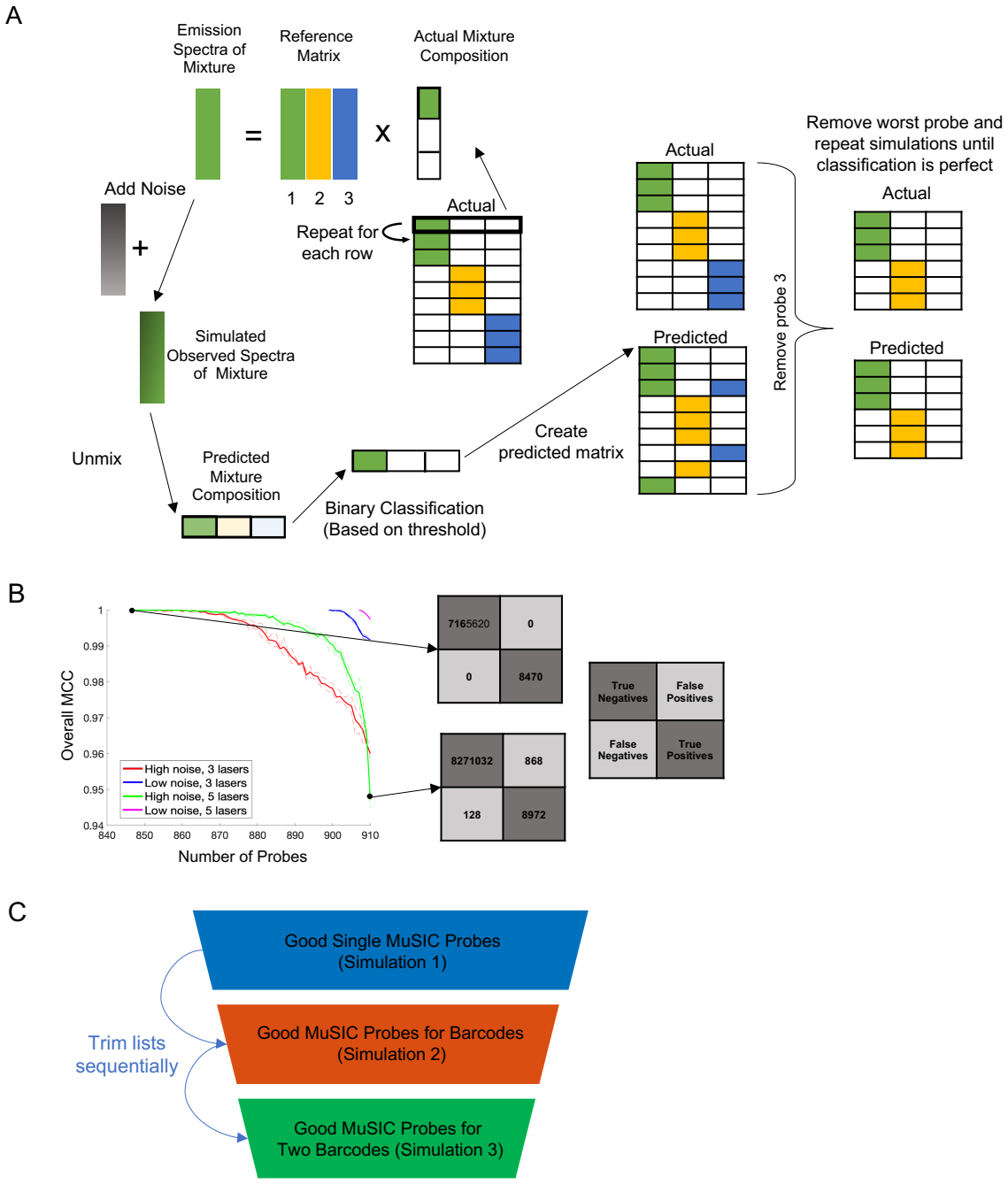

Figure 5.3: Workflow for probe removal. (A) Obtaining the list of good probes based on classification metrics. First, the emission spectra of a mixture of probes is simulated given a set of probes. Next, noise is added to the emission spectra and the spectra is unmixed (using the reference matrix) to predict the mixture composition of probes. Binary classification is performed and finally, the predicted mixture composition is compared to the actual mixture composition. This process is repeated for each probe and the worst performing probe is removed until the overall classification is perfect. (B) Graphical representation of probe removal results. Individual probes are removed until the overall MCC value (confusion matrices shown on the right-hand side) is perfect (i.e equal to 1). (C) Workflow of sequential trimming of lists of good MuSIC probes. The final list of good MuSIC probes for single MuSIC probes (simulation 1) is used as the starting list for simulation 2. Then the final list of good MuSIC probes for barcodes (simulation 2) is used as the starting list for simulation 3.

Discussion

Here we propose an approach for single-cell, non-destructive, and potentially genome-scale genetic and genetic interaction screens. This work builds on our recently developed theory for Multiplexing using Spectral Imaging and Combinatorics (MuSIC). MuSIC probes are stably linked combinations of fluorophores with unique spectral signatures that can be deconvolved when in a mixture with other MuSIC probes. The novel concept introduced in this work is that of a MuSIC barcode, a combination of MuSIC probes. Given currently available fluorescent proteins, we estimate that ~10^5 unique MuSIC barcodes can be created from combinations of MuSIC probes. We devised a simulation workflow to generate lists of MuSIC probes that are likely to be deconvolvable in a mixture, given binary classification applications. These results show the potential for genetic screens at the human genome-scale and genetic interaction screens for at least 1000s of genes. In some cases (i.e. 4 or 5 lasers and low noise), results show the potential to perform genetic interaction screens at a human genome-scale.

What could be learned with non-destructive, single-cell genetic screens? When analyses are done on a single-cell level, each cell is analyzed independently, and as a result, multiple measurements can be done in parallel, increasing throughput[232–234]. To accomplish this, CRISPR screenings have been paired with single-cell RNA sequencing using methods like Perturb-Seq[235], CRISP-seq[236], or CROP-seq[237,238]. While single-cell sequencing has the ability to pair transcriptome responses to a nucleic acid barcode that indicates the genetic

perturbation, it is as yet prohibitively expensive for covering interaction space[239,240]. Moreover, sequencing is a destructive technology so one cannot subsequently study perturbed cells-of-interest. The use of MuSIC barcodes could expand on the capabilities of these methods by allowing for high throughput genetic screening in a non-destructive manner. A non-destructive application in single live cells could allow sorting of rare cell types for subsequent follow-up studies. This could lead to co-isolating rare cell types thought to cooperate with each other for a disease phenotype.

What could be explored with high-dimensional non-destructive genetic interaction screens? One application is synthetic lethal interactions, which is defined as a genetic interaction that results in cell death, but disruption of the individual genes does not. Synthetic lethality has previously led to the discovery that poly(ADP-ribose) polymerase (PARP) inhibitors effectively kill BRCA1- and BRCA2 mutant tumor cells in breast cancer[241]. The proposed method may allow for genetic interaction screening at a near genome-scale, which could lead to the discovery of new synthetic lethal interactions in a high-throughput manner that is not currently possible. By discovering and exploiting synthetic lethal interactions in cancer cells, combinations of drugs can be used to treat cancer more effectively and at lower drug concentrations and thus lower toxicity[242].

Although simulations suggest a large potential for the approach when applied to genetic screening, there are multiple technical hurdles to its implementation. How can one clone thousands of unique MuSIC barcodes

specifically paired with matched gRNA? If one uses lentiviruses to deliver the constructs, how does one avoid template switching between genetically similar fluorescent proteins or barcodes, corrupting the connection between the barcode and gRNA[243]? The constructs may be large as well, so how does one achieve high enough titer to perform genetic interaction screening? Although flow cytometry is fast, can one assay enough cells to adequately explore gene interaction space? These are just some of the major issues that will arise, yet the potential applications, if these issues can be overcome, could be highly impactful.

Although we focused here on genetic screening as an application, genome-scale spectral barcode libraries could have other uses, such as high-dimensional cell lineage tracing. Current fluorescence-based lineage tracking is limited from spectral overlap and the number of unique probes. Techniques such as Brainbow work to fill this gap by using random ratios of different fluorophores to label cells[244], but are still limited to ~10s of deconvolvable colors[245]. This has been partially overcome through the use of DNA barcodes in each cell but requires destructive DNA sequencing to be deconvovled[245]. Music barcodes could be used to bridge this gap by expanding the available palette of color codes for fluorescence-based lineage tracing to potentially thousands of deconvolvable colors.

In conclusion, despite impending technical hurdles, the simulation studies presented here show the potential for MuSIC barcodes to enable high-dimensional genetic interaction screens at the human genome-scale. Its single-cell resolution compatibility and non-destructive features could also enable multiple new

applications for established genetic screening, or for cell lineage tracking. The capabilities of this approach can further be increased by increasing the number of excitation lasers and/or the spectral wavelength resolution.

Acknowledgments

The authors acknowledge funding from Clemson University, NIH/ NCI Grant R21CA196418, and NIH/NIGMS Grant R35 GM141891 . M.E.M. received funding from the Department of Education Grant P200A180076. This work was performed using the Clemson University Palmetto Super Computing Cluster.

Supplementary Figure and Table Legends

Figure S1: Comparison of lists of good probes between trials. The similarities and differences between the final lists of good probes for each trial are shown for each of the experimental setups.

Table S1: Fluorescent protein data. The maximum excitation and emission wavelength, brightness, extinction coefficient, and quantum yield for each fluorescent protein is found in the Attributes tab. Excitation and emission spectra for each fluorescent protein are found in the Excitation Spectra and Emission Spectra tabs, respectively. Sources for the raw data are found in the Sources tab.

Table S2: Probe lists. The lists of good probes for single probes, barcodes, and two barcodes are listed for each experimental setup in replicate.

Table S3: Simulated number of gRNA that could be used for genetic and genetic interaction screens with variable probe expression levels. We allowed probe expression levels to vary between 0.5 and 1.5 (relative) to capture single cell-to-cell variability. Results for the number of good probes that can be used to form barcodes and pairs of barcodes are shown for each experimental setup (the flow

cytometer used), the number of lasers used, and the noise level (either low or high). Given the number of good probes, the number of potential gRNA for genetic and genetic interaction screens is listed.

Table S4: Simulated number of gRNA that could be used for genetic and genetic interaction screens when only considering one and two-way fluorescent protein probes. Probes containing three fluorescent proteins were not considered here. Results for the number of good probes that can be used to form barcodes and pairs of barcodes are shown for each experimental setup (the flow cytometer used), the number of lasers used, and the noise level (either low or high). Given the number of good probes, the number of potential gRNA for genetic and genetic interaction screens is listed.

CHAPTER SIX

SIMULATION STUDIES FOR COMBINATIONS OF SMALL MOLECULE FLUOROPHORES

Abstract

Cells are the functional building blocks of multicellular organisms, where each cell type plays a different role in the body. Consequently, characterizing the various types and functions of each cell is a powerful tool for disease diagnosis and treatment. Recent advances in full spectrum flow cytometry (FSFC) have led to the increased multiplexing capability of 40 analytes simultaneously, rivaling the multiplexing ability of mass cytometry. We previously developed a theory for screening combinations of fluorescent proteins to create spectrally unique fluorescent probes. Here, we adjust this simulation workflow to simulate combinations of small molecule fluorophores rather than fluorescent proteins. Based on the constraints of 30 currently available small molecules and currently available spectral flow cytometry equipment, simulation studies suggest that cell-type profiling can be performed simultaneously at a level of 200+ analytes. This work, combined with our recently developed method for labeling antibodies with combinations of small molecule fluorophores, suggests our ability to label antibodies with combinations of small molecule fluorophores for flow cytometry based-highly multiplexed cell-type profiling.

Introduction

The human body is composed of multiple organ systems, each comprising numerous different cell types, which play an essential regulatory role in maintaining the body's homeostasis[246]. There is a drive to increase our understanding of each cell type of the human body to ultimately help provide better diagnoses, monitoring, and treatment of disease. For this reason, the Human Cell Atlas Project was created to generate molecular profiles of single cells across the different human organs and systems[247]. However, creating single-cell cartography of human tissues is a current grand challenge; initial efforts suggest hundreds to thousands of functionally distinct cell types exist[248]. One relevant development working towards this goal is cell type profiling, which is the process by which a complex mixture of cell types, for example, from blood or tumors, are classified into the fractional composition of its components (e.g., neutrophils, natural killer cells, various types of T and B cells, etc.), based on classification of expression patterns (e.g., CD3 expressed or not)[188].

A traditional method of cell-type profiling used for immune profiling is flow cytometry, which uses the maximum emission wavelength of fluorescently-labeled antibodies to measure the expression of protein components of a cell. The use of fluorescent antibodies with conventional flow cytometers is restricted to ~10-15 markers due to spectral overlap between fluorophores, severely limiting the number of cell types that can be distinguished[16,17]. However, flow cytometry remains a valuable platform for cell-type profiling as it is a cost-effective, high-

throughput, and non-destructive method with single-cell analysis[178]. Another method for cell-type profiling is mass cytometry. Here cell samples are labeled with isotopically pure rare earth metals and analyzed by mass spectrometry on a single-cell level. Metal-labeled antibodies circumvent the issue of spectral overlap allowing analysis of ~40+ analytes[173]. While mass cytometry has been revolutionary to the field of cell-type profiling, compared to flow cytometry, it is more expensive and acquires cells at a significantly lower rate (~300/400 events/second compared to thousands of events/second)[178,249]. Additionally, this method destroys the sample during acquisition, preventing the use of follow-up studies.

Another approach, single-cell RNA sequencing, is a state-of-the-art technique for cell-type profiling with unmatched multiplexing[181]. Thus far, no other method approaches the ability to identify 100s (or even 1000s) of cell types, as recent single-cell RNA sequencing studies suggest[181,182]. However, similar to mass cytometry, this method does not allow for the non-destructive analysis of samples. Further, it also requires substantial instrumentation, reagent cost, and personnel expertise, hindering adoption efforts outside of a high resource availability environment[250].

More recent developments have led to full-spectrum flow cytometry (FSFC), which captures the entire fluorophore emission using multiple excitation lasers and emission channels, creating a unique spectral fingerprint for each fluorophore[180]. This has enabled the simultaneous detection of 40 markers simultaneously[19], a

significant improvement relative to the traditional flow cytometry. However, FSFC is far from meeting the multiplexing capabilities of single-cell RNA sequencing. Therefore, a flow cytometry-based method that allows for an increased number of simultaneously detectable markers would be instrumental in current cell-type profiling efforts.

As such, we propose that by incorporating our recently developed method, Multiplexing using Spectral Imaging and Combinatorics (MuSIC)[21] with FSFC, we can expand the current multiplexing capabilities that FSFC can provide for cell-type profiling. MuSIC uses combinations of fluorophores to create spectrally unique MuSIC probes. In this study, we adapt our previously developed method[251] for screening combinations of MuSIC probes created from fluorescent proteins to screen combinations of MuSIC probes created from small molecule fluorophores. This work, combined with our recently developed method to covalently label antibodies with small molecule fluorophore-MuSIC probes[183], suggests that we can perform cell-type profiling of up to 265 markers simultaneously with currently available equipment.

Methods

Availability, Code Overview, and Simulation. All MATLAB code and raw data used for simulations are open-source on Zenodo. DOI: 10.5281/zenodo.7186939 The scripts `GenerateIDT_5probes_3l_HN.m` and `GenerateIDT_5probes_5l_HN.m` are used for generating the list of good probes for groups of 5 probes for 3 lasers/high noise (HN) and 5 lasers/high noise, respectively. The core of these scripts is done by the function `RemoveIDTprobes_onebyone.m`, which is adapted from the function `RemoveTwoBarcodes_onebyone.m` (McCarthy et al.) to simulate mixtures of 5 MuSIC probes rather than 4. The README file contains relevant information on the code for execution and reproducing the results. These simulations were performed in MATLAB using 40 CPUs on the Palmetto supercomputing cluster at Clemson University.

Data Sources. Emission spectra, excitation spectra, and brightness for fluorescent proteins were gathered from *idtdna.com* (**Supplementary Table 1** and references therein). Specifications for flow cytometer noise, excitation channels, and emission binning were obtained from the Aurora and Northern Lights flow cytometer user guides on *cytekbio.com*.

Results

This paper adapts a previously established theory for creating a library of fluorescent protein-MuSIC probes for genetic screening to create a library of small molecule-fluorophore MuSIC probes for cell-type profiling. We selected 30 small-molecule fluorophores (**Fig 6.1A)** currently available as oligo modifications at Integrated DNA Technologies to determine how many MuSIC probes could be created. Here we only consider MuSIC probes made from one- and two-way combinations of fluorophores, as this theory is based on the fluorophore-oligo labeling protocol described in Chapters 3-4. As previously described in Chapter 5, the ability to unmix probes depends on the FRET efficiency of the combination of fluorophores, which is directly related to the Förster radius and the physical distance between chromophores of the fluorophores. The distance between fluorophores in the MuSIC probe is adjustable by altering the number of base pairs between the fluorophores in the oligo complex (see Chapter 4); thus, the answer to this question depends on the Förster radius chosen as acceptable (**Fig 6.1B**). Since the minimum distance that fluorophores can be placed from one another is 5 bp, we only consider MuSIC probes that have an estimated Förster radius, R_0, greater than 17 angstroms (or 5 bp). At this cutoff, 372 MuSIC probes can be generated.

We then asked how many MuSIC probes should be present in a mixture to determine the multiplexing capabilities of MuSIC probes for cell-type profiling. Our previous work (Chapter 5) simulates mixtures of one, two, and four MuSIC probes

and removes poorly-performing probes based on classification parameters; however, for this study, we had to determine the number of MuSIC probes that can be co-expressed on a cell at one time. We chose to look at normal human PBMCs, as they are cells commonly used for immune profiling (a popular form of cell-type profiling), and we determined that up to 5 markers in a typical immune profiling panel could be present in a single cell type. Based on this, we adjusted our simulation workflow to simulate mixtures of 5 MuSIC probes. Unmixing, classification, and probe removal was performed as previously discussed (Chapter 5). Using the noise specifications and laser configurations of the 3-laser Cytek Northern lights and the 5-laser Cytek Aurora flow cytometers, we determined that 191 and 265 MuSIC deconvolvable probes could be used for cell-type profiling, respectively (**Fig 6.1C**). While replicates of the simulations still need to be performed, these preliminary results suggest the capability of MuSIC probes for cell-type profiling at a scale that is not currently possible with currently used methods.

A

Fluorophores	Ex max	Em max	Brightness
6-FAM	495	520	0.00675
HEX	538	555	0.00547
Yakima Yellow	524	551	0.00806
JOE	529	555	0.00438
TET	522	539	0.00534
Cy3	550	564	0.00204
Cy5	648	668	0.00750
Cy5.5	685	706	0.00627
ROX (NHS Ester)	588	608	0.00820
Tamra (NHS Ester)	559	583	0.00623
Atto 488	502	522	0.00720
Atto 532	534	554	0.01035
Atto 565	570	591	0.01080
Atto 590	602	624	0.00960
Atto 633	635	653	0.00832
Atto 550	560	575	0.01080
Atto 647	649	662	0.00240
Alexa Fluor 488	492	517	0.00627
Alexa Fluor 532	527	553	0.00518
Alexa Fluor 546	556	571	0.00958
Alexa Fluor 594	584	616	0.00299
Alexa Fluor 647	650	670	0.00260
Alexa Fluor 660	661	691	0.00181
Alexa Fluor 750	753	782	0.00348
5' IRDye 700	684	702	0.00127
5' IRDye 800	791	809	0.00259
5' IRDye 800CW	767	791	0.01458
Rhodamine Green	504	531	0.00459
Rhodamine Red	574	594	0.00801
Texas Red	598	617	0.00940

B

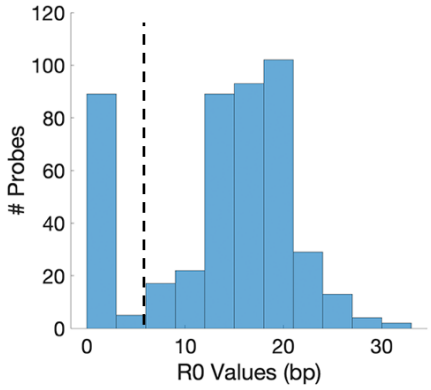

C

Experimental Setup	# Laser	# of Good Probes
Cytek Northern Lights	3	191
Cytek Aurora	5	265

Figure 6.1 Simulating small-molecule fluorophore probes. (A) List of small molecule fluorophores used in simulations with their corresponding brightness and excitation and emission maximum wavelength. (B) Forster Radius (R0) cutoff for probe selection. Only probes with an R0 greater than 5bp are selected. (C) The potential number of MuSIC probes that can be used in a panel for cell type profiling, given currently available flow cytometers.

Discussion

Here we propose an approach for spectral flow cytometry-based, highly multiplexed cell-type profiling. This work builds on our previously developed simulation workflow for screening lists of spectrally unique MuSIC probes, given current technology. The novel concept introduced here is adapting the previous simulation studies to create combinations of small molecule fluorophores instead of fluorescent proteins and generate lists of MuSIC probes that can be used for cell-type profiling rather than genetic interaction screening. Here we simulate mixtures of 5 different small-molecule MuSIC probes (as this is likely the maximum number of immune profiling markers that can be simultaneously present in a single cell) and test whether they are likely to be deconvolvable in a mixture based on binary classification applications. Using the results generated in this study, we can create panels of spectrally unique MuSIC probes based on current flow cytometry equipment constraints. These results show the potential for cell-type profiling of up to 265 cellular markers simultaneously using a Cytek Aurora flow cytometer.

How might one execute cell-type profiling of 265 markers? In order to perform highly multiplexed immune profiling, we can leverage our previously developed method to covalently label antibodies with combinations of small molecule fluorophores (MuSIC probes). In short, an oligo complex is created using complimentary oligos with internal fluorescent modifications to place combinations of small molecule fluorophores at specified distances and orientations from one another. Using a DBCO-Peg5- NHS Ester (linker), we can covalently bind the oligo

complex to an antibody. Using the panels generated here, we can covalently label antibodies with MuSIC probes and test these results experimentally by unmixing probes using a spectral flow cytometer.

CHAPTER SEVEN

CONCLUSION

Conclusions

This dissertation broadly covers the various applications of combination fluorescent probes for biological and diagnostic applications. This work was inspired by the need to study cells and tissues quantitatively at a single-cell level for cancer research, diagnostics, and treatment. Current state-of-the-art fluorescent labeling techniques still lack the multiplexing capability to measure greater than forty analytes in a single cell, primarily due to spectral overlap between fluorophores. We propose here that combinations of fluorophores can be used to create new spectrally unique probes for fluorescent imaging and flow cytometry, thus increasing the multiplexing capabilities of these techniques. With increased multiplexing capabilities, a complete visualization of cellular markers, spatial organization, and gene function could be achieved, leading to improved cancer diagnostics and treatment.

In chapter 2, we review current tissue imaging techniques and describe the advantages and disadvantages of each approach. We discuss fluorescent-based, mass spectrometry-based, and sequencing-based methods. Within fluorescent-based methods, we further categorize methods by filter-based or spectral. Within the spectral methods, we introduce our previously developed method of Multiplexing using Spectral Imaging and Combinatorics (MuSIC), which the rest of the dissertation is built on.

In chapters 3 and 4, we present a technique to covalently label antibodies with combinations of small molecule fluorophores (referred to as MuSIC probes). In chapter three, we offer the initial antibody labeling protocol and validate it using spin column purification and absorbance measurements. In chapter 4, we improve this method to achieve an increased fluorescent signal of the MuSIC probe-labeled antibodies. We found that by changing the orientation of the fluorophores within the oligo complex, we can improve the fluorescent signal by ~6-fold over the previous method. The new labeling method is compared to a conventional antibody labeling kit for signal intensity by staining human cells to further test the new labeling method. Results showed an increased signal intensity of MuSIC-probe stained cells compared to cells stained with the conventional labeling kit. This shows our ability to label antibodies with combination probes with adequate staining intensity compared to conventional methods.

In chapters 5 and 6, we introduce a simulation workflow to generate lists of MuSIC probes that, in theory, can be demultiplexed in a mixture. In chapter 5, we use a set of 18n currently available fluorescent proteins and generate MuSIC probes based on acceptable one-, two-, and three-way combinations of fluorescent proteins. We then introduce the concept of a MuSIC barcode (two MuSIC probes), which in theory, can be used to perform genetic screens, providing that MuSIC barcodes can be paired to guide RNA. We further predict the capabilities for genetic interaction screenings by using pairs of barcodes (four MuSIC probes) and find that we have the potential to perform genetic interaction screens at the human

genome scale. In Chapter 6, we adapt this simulation workflow to use a set of 30 small molecule fluorophores and make MuSIC probes based on acceptable one- and two-way combinations. Here we simulate the capabilities of MuSIC probes for cell-type profiling and find that we have the potential to perform cell-type profiling of 200+ analytes.

Future Work

Future work involves the experimental testing of the lists of MuSIC probes generated in chapters 5 and 6. Using the procedure demonstrated in chapters 3 and 4, antibodies can be labeled with the lists of MuSIC probes generated in chapter 6. Antibodies should be selected based on cell-type markers for the chosen cell line (here, we used human PBMCs). From here, cells stained with MuSIC probes will be analyzed using a spectral flow cytometer and compared to a commercially available panel. To start, groups of 40 MuSIC probes should be tested and compared against the state-of-the-art forty-color commercially available panel[19] for signal intensity and % cells stained. Unmixing will be performed to determine which MuSIC probes can be accurately demultiplexed in a mixture. This method will be repeated until all 265 probes have been tested. Finally, the full list of the remaining MuSIC probes will be tested using an antibody panel compatible with the chosen cell line to test the unmixing capabilities of the complete list.

The lists of MuSIC probes generated in chapter 5 should be used as a basis for the experimental testing of fluorescent-protein MuSIC probes for genetic and

genetic interaction screening. However, a method to pair the MuSIC barcodes to guide RNA must first be established, which will require future experimental design.

Although the methods discussed in this dissertation focus on cancer, in theory, they are general and can be applied to any genetic disease. The ability to characterize and visualize cellular components at a single-cell resolution is instrumental in the design of biological and diagnostic applications.

REFERENCES

(1) Nenclares, P.; Harrington, K. J. The Biology of Cancer. *Medicine (Baltimore)* **2020**, *48* (2), 67–72. https://doi.org/10.1016/j.mpmed.2019.11.001.

(2) Hassanpour, S. H.; Dehghani, M. Review of Cancer from Perspective of Molecular. *J. Cancer Res. Pract.* **2017**, *4* (4), 127–129. https://doi.org/10.1016/j.jcrpr.2017.07.001.

(3) Grzywa, T. M.; Paskal, W.; Włodarski, P. K. Intratumor and Intertumor Heterogeneity in Melanoma. *Transl. Oncol.* **2017**, *10* (6), 956–975. https://doi.org/10.1016/j.tranon.2017.09.007.

(4) Strickaert, A.; Saiselet, M.; Dom, G.; De Deken, X.; Dumont, J. E.; Feron, O.; Sonveaux, P.; Maenhaut, C. Cancer Heterogeneity Is Not Compatible with One Unique Cancer Cell Metabolic Map. *Oncogene* **2017**, *36* (19), 2637–2642. https://doi.org/10.1038/onc.2016.411.

(5) Turashvili, G.; Brogi, E. Tumor Heterogeneity in Breast Cancer. *Front. Med.* **2017**, *4*, 227. https://doi.org/10.3389/fmed.2017.00227.

(6) Mattiuzzi, C.; Lippi, G. Current Cancer Epidemiology. *J. Epidemiol. Glob. Health* **2019**, *9* (4), 217–222. https://doi.org/10.2991/jegh.k.191008.001.

(7) Wilbrey-Clark, A.; Roberts, K.; Teichmann, S. A. Cell Atlas Technologies and Insights into Tissue Architecture. *Biochem. J.* **2020**, *477* (8), 1427–1442. https://doi.org/10.1042/BCJ20190341.

(8) Zhang, X.; Lan, Y.; Xu, J.; Quan, F.; Zhao, E.; Deng, C.; Luo, T.; Xu, L.; Liao, G.; Yan, M.; Ping, Y.; Li, F.; Shi, A.; Bai, J.; Zhao, T.; Li, X.; Xiao, Y. CellMarker: A Manually Curated Resource of Cell Markers in Human and Mouse. *Nucleic Acids Res.* **2019**, *47* (D1), D721–D728. https://doi.org/10.1093/nar/gky900.

(9) McKinnon, K. M. Flow Cytometry: An Overview. *Curr. Protoc. Immunol.* **2018**, *120* (1), 5.1.1-5.1.11. https://doi.org/10.1002/cpim.40.

(10) Spitzer, M. H.; Nolan, G. P. Mass Cytometry: Single Cells, Many Features. *Cell* **2016**, *165* (4), 780–791. https://doi.org/10.1016/j.cell.2016.04.019.

(11) Ahmed, R.; Zaman, T.; Chowdhury, F.; Mraiche, F.; Tariq, M.; Ahmad, I. S.; Hasan, A. Single-Cell RNA Sequencing with Spatial Transcriptomics of Cancer Tissues. *Int. J. Mol. Sci.* **2022**, *23* (6). https://doi.org/10.3390/ijms23063042.

(12) Hartmann, F. J.; Bendall, S. C. Immune Monitoring Using Mass Cytometry and Related High-Dimensional Imaging Approaches. *Nat. Rev. Rheumatol.* **2020**, *16* (2), 87–99. https://doi.org/10.1038/s41584-019-0338-z.

(13) Ferrer-Font, L.; Mayer, J. U.; Old, S.; Hermans, I. F.; Irish, J.; Price, K. M. High-Dimensional Data Analysis Algorithms Yield Comparable Results for Mass Cytometry and Spectral Flow Cytometry Data. *Cytometry A* **2020**, *97* (8), 824–831. https://doi.org/10.1002/cyto.a.24016.

(14) Ratnasiri, K.; Wilk, A. J.; Lee, M. J.; Khatri, P.; Blish, C. A. Single-Cell RNA-Seq Methods to Interrogate Virus-Host Interactions. *Semin. Immunopathol.* **2023**, *45* (1), 71–89. https://doi.org/10.1007/s00281-022-00972-2.
(15) McKinnon, K. M. Multiparameter Conventional Flow Cytometry. In *Flow Cytometry Protocols*; Hawley, T. S., Hawley, R. G., Eds.; Springer New York: New York, NY, 2018; pp 139–150. https://doi.org/10.1007/978-1-4939-7346-0_8.
(16) Newell, E. W.; Sigal, N.; Bendall, S. C.; Nolan, G. P.; Davis, M. M. Cytometry by Time-of-Flight Shows Combinatorial Cytokine Expression and Virus-Specific Cell Niches within a Continuum of CD8+ T Cell Phenotypes. *Immunity* **2012**, *36* (1), 142–152. https://doi.org/10.1016/j.immuni.2012.01.002.
(17) Adan, A.; Alizada, G.; Kiraz, Y.; Baran, Y.; Nalbant, A. Flow Cytometry: Basic Principles and Applications. *Crit. Rev. Biotechnol.* **2017**, *37* (2), 163–176. https://doi.org/10.3109/07388551.2015.1128876.
(18) Bonilla, D. L.; Reinin, G.; Chua, E. Full Spectrum Flow Cytometry as a Powerful Technology for Cancer Immunotherapy Research. *Front. Mol. Biosci.* **2021**, *7*.
(19) Park, L. M.; Lannigan, J.; Jaimes, M. C. OMIP-069: Forty-Color Full Spectrum Flow Cytometry Panel for Deep Immunophenotyping of Major Cell Subsets in Human Peripheral Blood. *Cytometry A* **2020**, *97* (10), 1044–1051. https://doi.org/10.1002/cyto.a.24213.
(20) Sekar, R. B.; Periasamy, A. Fluorescence Resonance Energy Transfer (FRET) Microscopy Imaging of Live Cell Protein Localizations. *J. Cell Biol.* **2003**, *160* (5), 629–633. https://doi.org/10.1083/jcb.200210140.
(21) Holzapfel, H. Y.; Stern, A. D.; Bouhaddou, M.; Anglin, C. M.; Putur, D.; Comer, S.; Birtwistle, M. R. Fluorescence Multiplexing with Spectral Imaging and Combinatorics. *ACS Comb. Sci.* **2018**, *20* (11), 653–659. https://doi.org/10.1021/acscombsci.8b00101.
(22) McCarthy, M. E.; Birtwistle, M. R. Highly Multiplexed, Quantitative Tissue Imaging at Cellular Resolution. *Curr. Pathobiol. Rep.* **2019**, *7* (3), 109–118. https://doi.org/10.1007/s40139-019-00203-8.
(23) Koifman, G.; Rotter, V.; Aloni-Grinstein, R. P53 Balances between Tissue Hierarchy and Anarchy. **2019**. https://doi.org/10.1093/jmcb/mjz022.
(24) Griffith, L. G.; Swartz, M. A. Capturing Complex 3D Tissue Physiology in Vitro. *Nat. Rev. Mol. Cell Biol.* **2006**, *7*, 211.
(25) Tainaka, K.; Kubota, S. I.; Suyama, T. Q.; Susaki, E. A.; Perrin, D.; Ukai-Tadenuma, M.; Ukai, H.; Ueda, H. R. Whole-Body Imaging with Single-Cell Resolution by Tissue Decolorization. *Cell* **2014**, *159* (4), 911–924. https://doi.org/10.1016/j.cell.2014.10.034.
(26) Gerner, M. Y.; Kastenmuller, W.; Ifrim, I.; Kabat, J.; Germain, R. N. Histo-Cytometry: A Method for Highly Multiplex Quantitative Tissue Imaging Analysis Applied to Dendritic Cell Subset Microanatomy in Lymph Nodes.

Immunity **2012**, *37* (2), 364–376. https://doi.org/10.1016/j.immuni.2012.07.011.
(27) Bissell, M. J.; Rizki, A.; Mian, I. S. Tissue Architecture: The Ultimate Regulator of Breast Epithelial Function. *Curr. Opin. Cell Biol.* **2003**, *15* (6), 753–762. https://doi.org/10.1016/j.ceb.2003.10.016.
(28) Sasai, Y. Cytosystems Dynamics in Self-Organization of Tissue Architecture. *Nature* **2013**, *493* (7432), 318–326. https://doi.org/10.1038/nature11859.
(29) Van J. Wedeen; Patric Hagmann; Wen-Yih Isaac Tseng; Timothy G. Reese; Robert M. Weisskoff. Mapping Complex Tissue Architecture with Diffusion Spectrum Magnetic Resonance Imaging. *Magnetic Resonance in Medicine*. 2005, pp 1377–1386. https://doi.org/10.1002/mrm.20642.
(30) Cohen, A. S.; Morse, D. L.; Chen, T.; Rejniak, K. A.; Estrella, V.; Lloyd, M. C. The Role of Tumor Tissue Architecture in Treatment Penetration and Efficacy: An Integrative Study. *Front. Oncol.* **2013**, *3* (May), 1–13. https://doi.org/10.3389/fonc.2013.00111.
(31) Nelson, C. M.; Bissell, M. J. Of Extracellular Matrix, Scaffolds, and Signaling: Tissue Architecture Regulates Development, Homeostasis, and Cancer. *Annu. Rev. Cell Dev. Biol.* **2006**, *22* (1), 287–309. https://doi.org/10.1146/annurev.cellbio.22.010305.104315.
(32) Kherlopian, A. R.; Song, T.; Duan, Q.; Neimark, M. A.; Po, M. J.; Gohagan, J. K.; Laine, A. F. A Review of Imaging Techniques for Systems Biology. *BMC Syst. Biol.* **2008**, *2*, 1–18. https://doi.org/10.1186/1752-0509-2-74.
(33) Micheva, K. D.; Smith, S. J. Array Tomography: A New Tool for Imaging the Molecular Architecture and Ultrastructure of Neural Circuits. *Neuron* **2007**, *55* (1), 25–36. https://doi.org/10.1016/j.neuron.2007.06.014.
(34) Hama, H.; Kurokawa, H.; Kawano, H.; Ando, R.; Shimogori, T.; Noda, H.; Fukami, K.; Sakaue-Sawano, A.; Miyawaki, A. Scale: A Chemical Approach for Fluorescence Imaging and Reconstruction of Transparent Mouse Brain. *Nat. Neurosci.* **2011**, *14*, 1481.
(35) Lee, E.; Choi, J.; Jo, Y.; Kim, J. Y.; Jang, Y. J.; Lee, H. M.; Kim, S. Y.; Lee, H.-J.; Cho, K.; Jung, N.; Hur, E. M.; Jeong, S. J.; Moon, C.; Choe, Y.; Rhyu, I. J.; Kim, H.; Sun, W. ACT-PRESTO: Rapid and Consistent Tissue Clearing and Labeling Method for 3-Dimensional (3D) Imaging. *Sci. Rep.* **2016**, *6*, 18631.
(36) Roelofs, A. J.; De Bari, C. Immunostaining of Skeletal Tissues. In *Methods in molecular biology*; 2019; Vol. 1914, pp 437–450. https://doi.org/10.1007/978-1-4939-8997-3_25.
(37) Intartaglia, M.; Sabetta, R.; Gargiulo, M.; Roncador, G.; Marino, F. Z.; Franco, R. Immunohistochemistry for Cancer Stem Cells Detection: Principles and Methods. In *Cancer Stem Cells: Methods and Protocols*; Papaccio, G., Desiderio, V., Eds.; Springer New York: New York, NY, 2018; pp 195–211. https://doi.org/10.1007/978-1-4939-7401-6_17.

(38) Ouyang, N.; Wang, L. Basic Histopathological Methods and Breast Lesion Types for Research. In *Breast Cancer: Methods and Protocols*; Cao, J., Ed.; Springer New York: New York, NY, 2016; pp 3–9. https://doi.org/10.1007/978-1-4939-3444-7_1.
(39) Taylor, C. R. Immunohistochemistry in Surgical Pathology: Principles and Practice. In *Histopathology: Methods and Protocols*; Day, C. E., Ed.; Springer New York: New York, NY, 2014; pp 81–109. https://doi.org/10.1007/978-1-4939-1050-2_5.
(40) Sedgewick, J. Imaging Techniques in Signal Transduction IHC. In *Signal Transduction Immunohistochemistry: Methods and Protocols*; Kalyuzhny, A. E., Ed.; Humana Press: Totowa, NJ, 2011; pp 113–142. https://doi.org/10.1007/978-1-61779-024-9_7.
(41) Robertson, D.; Savage, K.; Reis-Filho, J. S.; Isacke, C. M. Multiple Immunofluorescence Labelling of Formalin-Fixed Paraffin-Embedded (FFPE) Tissue. *BMC Cell Biol.* **2008**, *9*, 1–10. https://doi.org/10.1186/1471-2121-9-13.
(42) Rimm, D. L. What Brown Cannot Do for You. *Nat. Biotechnol.* **2006**, *24* (8), 914–916. https://doi.org/10.1038/nbt0806-914.
(43) Jensen, K.; Krusenstjerna-Hafstrøm, R.; Lohse, J.; Petersen, K. H.; Derand, H. A Novel Quantitative Immunohistochemistry Method for Precise Protein Measurements Directly in Formalin-Fixed, Paraffin-Embedded Specimens: Analytical Performance Measuring HER2. *Mod. Pathol.* **2016**, *30*, 180.
(44) Islam, S.; Kjällquist, U.; Moliner, A.; Zajac, P.; Fan, J.-B.; Lönnerberg, P.; Linnarsson, S. Highly Multiplexed and Strand-Specific Single-Cell RNA 5′ End Sequencing. *Nat. Protoc.* **2012**, *7*, 813.
(45) Ren, X.; Kang, B.; Zhang, Z. Understanding Tumor Ecosystems by Single-Cell Sequencing: Promises and Limitations. *Genome Biol.* **2018**, *19* (1), 211. https://doi.org/10.1186/s13059-018-1593-z.
(46) NIH. Department of Health and Human Services Part 1 . Overview Information. *Natl. Inst. Health RFA-AI-14-047* **2014**, *10*, 1–3.
(47) Graf, J. F.; Zavodszky, M. I. Characterizing the Heterogeneity of Tumor Tissues from Spatially Resolved Molecular Measures. *PLoS ONE* **2017**, *12* (11), 1–20. https://doi.org/10.1371/journal.pone.0188878.
(48) Alizadeh, A. A.; Aranda, V.; Bardelli, A.; Blanpain, C.; Bock, C.; Borowski, C.; Caldas, C.; Califano, A.; Doherty, M.; Elsner, M.; Esteller, M.; Fitzgerald, R.; Korbel, J. O.; Lichter, P.; Mason, C. E.; Navin, N.; Pe'er, D.; Polyak, K.; Roberts, C. W. M.; Siu, L.; Snyder, A.; Stower, H.; Swanton, C.; Verhaak, R. G. W.; Zenklusen, J. C.; Zuber, J.; Zucman-Rossi, J. Toward Understanding and Exploiting Tumor Heterogeneity. *Nat. Med.* **2015**, *21*, 846.
(49) O'Connor, J. P. B.; Rose, C. J.; Waterton, J. C.; Carano, R. A. D.; Parker, G. J. M.; Jackson, A. Imaging Intratumor Heterogeneity: Role in Therapy

Response, Resistance, and Clinical Outcome. *Clin. Cancer Res.* **2015**, *21* (2), 249–257. https://doi.org/10.1158/1078-0432.CCR-14-0990.
(50) Sottoriva, A.; Spiteri, I.; Piccirillo, S. G. M.; Touloumis, A.; Collins, V. P.; Marioni, J. C.; Curtis, C.; Watts, C.; Tavaré, S. Intratumor Heterogeneity in Human Glioblastoma Reflects Cancer Evolutionary Dynamics. *Proc. Natl. Acad. Sci. U. S. A.* **2013**, *110* (10), 4009–4014. https://doi.org/10.1073/pnas.1219747110.
(51) Gerlinger, M.; Rowan, A. J.; Horswell, S.; Math, M.; Larkin, J.; Endesfelder, D.; Gronroos, E.; Martinez, P.; Matthews, N.; Stewart, A.; Tarpey, P.; Varela, I.; Phillimore, B.; Begum, S.; McDonald, N. Q.; Butler, A.; Jones, D.; Raine, K.; Latimer, C.; Santos, C. R.; Nohadani, M.; Eklund, A. C.; Spencer-Dene, B.; Clark, G.; Pickering, L.; Stamp, G.; Gore, M.; Szallasi, Z.; Downward, J.; Futreal, P. A.; Swanton, C. Intratumor Heterogeneity and Branched Evolution Revealed by Multiregion Sequencing. *N. Engl. J. Med.* **2012**, *366* (10), 883–892. https://doi.org/10.1056/NEJMoa1113205.
(52) Landau, D. A.; Carter, S. L.; Stojanov, P.; McKenna, A.; Stevenson, K.; Lawrence, M. S.; Sougnez, C.; Stewart, C.; Sivachenko, A.; Wang, L.; Wan, Y.; Zhang, W.; Shukla, S. A.; Vartanov, A.; Fernandes, S. M.; Saksena, G.; Cibulskis, K.; Tesar, B.; Gabriel, S.; Hacohen, N.; Meyerson, M.; Lander, E. S.; Neuberg, D.; Brown, J. R.; Getz, G.; Wu, C. J. Evolution and Impact of Subclonal Mutations in Chronic Lymphocytic Leukemia. *Cell* **2013**, *152* (4), 714–726. https://doi.org/10.1016/j.cell.2013.01.019.
(53) Gerdes, M. J.; Gökmen-Polar, Y.; Sui, Y.; Pang, A. S.; Laplante, N.; Harris, A. L.; Tan, P. H.; Ginty, F.; Badve, S. S. Single-Cell Heterogeneity in Ductal Carcinoma in Situ of Breast. *Mod. Pathol.* **2018**, *31* (3), 406–417. https://doi.org/10.1038/modpathol.2017.143.
(54) Marusyk, A.; Polyak, K. Tumor Heterogeneity: Causes and Consequences. *Biochim. Biophys. Acta* **2010**, *1805* (1), 105–117. https://doi.org/10.1016/j.bbcan.2009.11.002.
(55) Tsujikawa, T.; Kumar, S.; Borkar, R. N.; Azimi, V.; Thibault, G.; Chang, Y. H.; Balter, A.; Kawashima, R.; Choe, G.; Sauer, D.; El Rassi, E.; Clayburgh, D. R.; Kulesz-Martin, M. F.; Lutz, E. R.; Zheng, L.; Jaffee, E. M.; Leyshock, P.; Margolin, A. A.; Mori, M.; Gray, J. W.; Flint, P. W.; Coussens, L. M. Quantitative Multiplex Immunohistochemistry Reveals Myeloid-Inflamed Tumor-Immune Complexity Associated with Poor Prognosis. *Cell Rep.* **2017**, *19* (1), 203–217. https://doi.org/10.1016/j.celrep.2017.03.037.
(56) Kobayashi, H.; Longmire, M. R.; Ogawa, M.; Choyke, P. L.; Kawamoto, S. Multiplexed Imaging in Cancer Diagnosis: Applications and Future Advances. *Lancet Oncol.* **2010**, *11* (6), 589–595. https://doi.org/10.1016/S1470-2045(10)70009-7.
(57) Lee, H.; Langham, M. C.; Rodriguez-Soto, A. E.; Wehrli, F. W. Multiplexed MRI Methods for Rapid Estimation of Global Cerebral Metabolic Rate of Oxygen Consumption. *NeuroImage* **2017**, *149*, 393–403. https://doi.org/10.1016/j.neuroimage.2017.02.011.

(58) Yang, M.; Gao, H.; Sun, X.; Yan, Y.; Quan, Q.; Zhang, W.; Mohamedali, K. A.; Rosenblum, M. G.; Niu, G.; Chen, X. Multiplexed PET Probes for Imaging Breast Cancer Early Response to $VEGF_{121}$/RGel Treatment. *Mol. Pharm.* **2011**, *8* (2), 621–628. https://doi.org/10.1021/mp100446t.
(59) Dobrucki, J. W.; Kubitscheck, U. Fluorescence Microscopy. *Fluoresc. Microsc. Princ. Biol. Appl. Second Ed.* **2017**, *2* (12), 85–132. https://doi.org/10.1002/9783527687732.ch3.
(60) Gao, L.; Hagen, N.; Tkaczyk, T. S. Quantitative Comparison between Full-Spectrum and Filter-Based Imaging in Hyperspectral Fluorescence Microscopy. *J. Microsc.* **2012**, *246* (2), 113–123. https://doi.org/10.1111/j.1365-2818.2012.03596.x.
(61) Lu, G.; Fei, B. Medical Hyperspectral Imaging: A Review. *J. Biomed. Opt.* **2014**, *19* (1), 010901. https://doi.org/10.1117/1.jbo.19.1.010901.
(62) Leavesley, S. J.; Annamdevula, N.; Boni, J.; Stocker, S.; Grant, K.; Troyanovsky, B.; Rich, T. C.; Alvarez, D. F. Hyperspectral Imaging Microscopy for Identification and Quantitative Analysis of Fluorescently-Labeled Cells in Highly Autofluorescent Tissue. *J. Biophotonics* **2012**, *5* (1), 67–84. https://doi.org/10.1002/jbio.201100066.
(63) Terai, T.; Nagano, T. Small-Molecule Fluorophores and Fluorescent Probes for Bioimaging. *Pflüg. Arch. - Eur. J. Physiol.* **2013**, *465* (3), 347–359. https://doi.org/10.1007/s00424-013-1234-z.
(64) Wysocki, L. M.; Lavis, L. D. Advances in the Chemistry of Small Molecule Fluorescent Probes. *Curr. Opin. Chem. Biol.* **2011**, *15* (6), 752–759. https://doi.org/10.1016/j.cbpa.2011.10.013.
(65) Luo, S.; Tan, X.; Fang, S.; Wang, Y.; Liu, T.; Wang, X.; Yuan, Y.; Sun, H.; Qi, Q.; Shi, C. Mitochondria-Targeted Small-Molecule Fluorophores for Dual Modal Cancer Phototherapy. *Adv. Funct. Mater.* **2016**, *26* (17), 2826–2835. https://doi.org/10.1002/adfm.201600159.
(66) Chudakov, D. M.; Matz, M. V; Lukyanov, S.; Lukyanov, K. A. Fluorescent Proteins and Their Applications in Imaging Living Cells and Tissues. *Physiol. Rev.* **2010**, *90* (3), 1103–1163. https://doi.org/10.1152/physrev.00038.2009.
(67) Shaner, N. C.; Steinbach, P. A.; Tsien, R. Y. A Guide to Choosing Fluorescent Proteins. *Nat. Methods* **2005**, *2* (12), 905–909. https://doi.org/10.1038/nmeth819.
(68) Hoffman, R. M. The Multiple Uses of Fluorescent Proteins to Visualize Cancer in Vivo. *Nat. Rev. Cancer* **2005**, *5* (10), 796–806. https://doi.org/10.1038/nrc1717.
(69) Bates, M.; Huang, B.; Dempsey, G. T.; Zhuang, X. Multicolor Super-Resolution Imaging with Photo-Switchable Fluorescent Probes. *Science* **2007**, *317* (5845), 1749 LP – 1753. https://doi.org/10.1126/science.1146598.

(70) Habuchi, S.; Tsutsui, H.; Kochaniak, A. B.; Miyawaki, A.; van Oijen, A. M. MKikGR, a Monomeric Photoswitchable Fluorescent Protein. *PLoS ONE* **2008**, *3* (12), e3944. https://doi.org/10.1371/journal.pone.0003944.
(71) Bates, M.; Huang, B.; Zhuang, X. Super-Resolution Microscopy by Nanoscale Localization of Photo-Switchable Fluorescent Probes. *Curr. Opin. Chem. Biol.* **2008**, *12* (5), 505–514. https://doi.org/10.1016/j.cbpa.2008.08.008.
(72) Ma, Q.; Su, X. Recent Advances and Applications in QDs-Based Sensors. *Analyst* **2011**, *136* (23), 4883–4893. https://doi.org/10.1039/C1AN15741H.
(73) Michalet, X.; Pinaud, F. F.; Bentolila, L. A.; Tsay, J. M.; Doose, S.; Li, J. J.; Sundaresan, G.; Wu, A. M.; Gambhir, S. S.; Weiss, S. Quantum Dots for Live Cells, in Vivo Imaging, and Diagnostics. *Science* **2005**, *307* (5709), 538 LP – 544. https://doi.org/10.1126/science.1104274.
(74) Medintz, I. L.; Uyeda, H. T.; Goldman, E. R.; Mattoussi, H. Quantum Dot Bioconjugates for Imaging, Labelling and Sensing. *Nat. Mater.* **2005**, *4* (6), 435–446. https://doi.org/10.1038/nmat1390.
(75) Wu, C.; Chiu, D. T. Highly Fluorescent Semiconducting Polymer Dots for Biology and Medicine. *Angew. Chem. Int. Ed.* **2013**, *52* (11), 3086–3109. https://doi.org/10.1002/anie.201205133.
(76) Liu, H.-Y.; Wu, P.-J.; Kuo, S.-Y.; Chen, C.-P.; Chang, E.-H.; Wu, C.-Y.; Chan, Y.-H. Quinoxaline-Based Polymer Dots with Ultrabright Red to Near-Infrared Fluorescence for In Vivo Biological Imaging. *J. Am. Chem. Soc.* **2015**, *137* (32), 10420–10429. https://doi.org/10.1021/jacs.5b06710.
(77) Brancaleon, L.; Durkin, A. J.; Tu, J. H.; Menaker, G.; Fallon, J. D.; Kollias, N. In Vivo Fluorescence Spectroscopy of Nonmelanoma Skin Cancer¶. *Photochem. Photobiol.* **2001**, *73* (2), 178–183. https://doi.org/10.1562/0031-8655(2001)0730178IVFSON2.0.CO2.
(78) Reinert, K. C.; Dunbar, R. L.; Gao, W.; Chen, G.; Ebner, T. J. Flavoprotein Autofluorescence Imaging of Neuronal Activation in the Cerebellar Cortex In Vivo. *J. Neurophysiol.* **2004**, *92* (1), 199–211. https://doi.org/10.1152/jn.01275.2003.
(79) Brookner, C. K.; Follen, M.; Boiko, I.; Galvan, J.; Thomsen, S.; Malpica, A.; Suzuki, S.; Lotan, R.; Richards-Kortum, R. Autofluorescence Patterns in Short-Term Cultures of Normal Cervical Tissue. *Photochem. Photobiol.* **2000**, *71* (6), 730–736. https://doi.org/10.1562/0031-8655(2000)0710730APISTC2.0.CO2.
(80) *Confocal Microscopy: Methods and Protocols*, 1st ed.; Paddock, S., Ed.; Humana Press, 1999. https://doi.org/Softcover ISBN 978-1-61737-062-5 Series ISSN 1064-3745 Edition Number 1 Number of Pages XII, 446 Topics.
(81) *Advanced Fluorescence Microscopy*; Verveer, P. J., Ed.; Methods in Molecular Biology; Springer New York: New York, NY, 2015; Vol. 1251. https://doi.org/10.1007/978-1-4939-2080-8.

(82) Gerdes, M. J.; Sevinsky, C. J.; Sood, A.; Adak, S.; Bello, M. O.; Bordwell, A.; Can, A.; Corwin, A.; Dinn, S.; Filkins, R. J.; Hollman, D.; Kamath, V.; Kaanumalle, S.; Kenny, K.; Larsen, M.; Lazare, M.; Li, Q.; Lowes, C.; McCulloch, C. C.; McDonough, E.; Montalto, M. C.; Pang, Z.; Rittscher, J.; Santamaria-Pang, A.; Sarachan, B. D.; Seel, M. L.; Seppo, A.; Shaikh, K.; Sui, Y.; Zhang, J.; Ginty, F. Highly Multiplexed Single-Cell Analysis of Formalin-Fixed, Paraffin-Embedded Cancer Tissue. *Proc. Natl. Acad. Sci.* **2013**, *110* (29), 11982–11987. https://doi.org/10.1073/pnas.1300136110.

(83) Gut, G.; Herrmann, M. D.; Pelkmans, L. Multiplexed Protein Maps Link Subcellular Organization to Cellular States. *Science* **2018**, *361* (6401). https://doi.org/10.1126/science.aar7042.

(84) Lin, J. R.; Fallahi-Sichani, M.; Chen, J. Y.; Sorger, P. K. Cyclic Immunofluorescence (CycIF), A Highly Multiplexed Method for Single-Cell Imaging. *Curr. Protoc. Chem. Biol.* **2016**, *8* (4), 251–264. https://doi.org/10.1002/cpch.14.

(85) Lin, J. R.; Izar, B.; Wang, S.; Yapp, C.; Mei, S.; Shah, P. M.; Santagata, S.; Sorger, P. K. Highly Multiplexed Immunofluorescence Imaging of Human Tissues and Tumors Using T-CyCIF and Conventional Optical Microscopes. *eLife* **2018**, *7*, 1–46. https://doi.org/10.7554/eLife.31657.

(86) Goltsev, Y.; Samusik, N.; Kennedy-Darling, J.; Bhate, S.; Hale, M.; Vazquez, G.; Black, S.; Nolan, G. P. Deep Profiling of Mouse Splenic Architecture with CODEX Multiplexed Imaging. *Cell* **2018**, *174* (4), 968-981.e15. https://doi.org/10.1016/j.cell.2018.07.010.

(87) Jobin, C.; Sui, Y.; McKinley, E. T.; Al-Kofahi, Y.; Lau, K. S.; Coffey, R. J.; Franklin, J. L.; Roland, J. T.; Ohland, C. L.; Santamaria-Pang, A.; Gerdes, M. J.; Millis, B. A.; Tyska, M. J. Optimized Multiplex Immunofluorescence Single-Cell Analysis Reveals Tuft Cell Heterogeneity. *JCI Insight* **2017**, *2* (11). https://doi.org/10.1172/jci.insight.93487.

(88) Nadarajan, G.; Hope, T.; Wang, D.; Cheung, A.; Ginty, F.; Yaffe, M. J.; Doyle, S. Automated Multi-Class Ground-Truth Labeling of H&E Images for Deep Learning Using Multiplexed Fluorescence Microscopy. In *Proc.SPIE*; 2019; Vol. 10956.

(89) Lin, J. R.; Fallahi-Sichani, M.; Sorger, P. K. Highly Multiplexed Imaging of Single Cells Using a High-Throughput Cyclic Immunofluorescence Method. *Nat. Commun.* **2015**, *6*, 1–7. https://doi.org/10.1038/ncomms9390.

(90) Lin, J.-R. Multiplexed Single-Cell Imaging: Past, Present, and Future. *ASSAY Drug Dev. Technol.* **2016**, *15* (1), 8–10. https://doi.org/10.1089/adt.2016.765.

(91) Todorovic, V. A Tissue-to-Organelle View of Cellular Proteins. *Nat. Methods* **2018**, *15* (10), 760. https://doi.org/10.1038/s41592-018-0163-3.

(92) Lubeck, E.; Cai, L. Single-Cell Systems Biology by Super-Resolution Imaging and Combinatorial Labeling. *Nat. Methods* **2012**, *9* (7), 743–748. https://doi.org/10.1038/nmeth.2069.

(93) Bartman, C. R.; Hamagami, N.; Keller, C. A.; Giardine, B.; Hardison, R. C.; Blobel, G. A.; Raj, A. Transcriptional Burst Initiation and Polymerase Pause Release Are Key Control Points of Transcriptional Regulation. *Mol. Cell* **2019**, *73* (3), 519-532.e4. https://doi.org/10.1016/j.molcel.2018.11.004.
(94) Rouhanifard, S. H.; Mellis, I. A.; Dunagin, M.; Bayatpour, S.; Jiang, C. L.; Dardani, I.; Symmons, O.; Emert, B.; Torre, E.; Cote, A.; Sullivan, A.; Stamatoyannopoulos, J. A.; Raj, A. ClampFISH Detects Individual Nucleic Acid Molecules Using Click Chemistry–Based Amplification. *Nat. Biotechnol.* **2018**, *37*, 84.
(95) Bridger, J. M.; Morris, K. *Fluorescence in Situ Hybridization (FISH): Protocols and Applications*; Methods in Molecular Biology; Humana Press, 2010.
(96) Cai, L. Turning Single Cells into Microarrays by Super-Resolution Barcoding. *Brief. Funct. Genomics* **2013**, *12* (2), 75–80. https://doi.org/10.1093/bfgp/els054.
(97) Eng, C.-H. L.; Lawson, M.; Zhu, Q.; Dries, R.; Koulena, N.; Takei, Y.; Yun, J.; Cronin, C.; Karp, C.; Yuan, G.-C.; Cai, L. Transcriptome-Scale Super-Resolved Imaging in Tissues by RNA SeqFISH+. *Nature* **2019**. https://doi.org/10.1038/s41586-019-1049-y.
(98) Gratton, E. Fluorescence Lifetime Imaging for the Two-Photon Microscope: Time-Domain and Frequency-Domain Methods. *J. Biomed. Opt.* **2003**, *8* (3), 381. https://doi.org/10.1117/1.1586704.
(99) Funane, T.; Hou, S. S.; Zoltowska, K. M.; van Veluw, S. J.; Berezovska, O.; Kumar, A. T. N.; Bacskai, B. J. Selective Plane Illumination Microscopy (SPIM) with Time-Domain Fluorescence Lifetime Imaging Microscopy (FLIM) for Volumetric Measurement of Cleared Mouse Brain Samples. *Rev. Sci. Instrum.* **2018**, *89* (5), 53705. https://doi.org/10.1063/1.5018846.
(100) Digman, M. A.; Caiolfa, V. R.; Zamai, M.; Gratton, E. The Phasor Approach to Fluorescence Lifetime Imaging Analysis. *Biophys. J.* **2008**, *94* (2), L14–L16. https://doi.org/10.1529/biophysj.107.120154.
(101) Cole, M. J.; Siegel, J.; Webb, S. E. D.; Jones, R.; Dowling, K.; Dayel, M. J.; Parsons-Karavassilis, D.; French, P. M. W.; Lever, M. J.; Sucharov, L. O. D.; Neil, M. A. A.; Juškaitis, R.; Wilson, T. Time-Domain Whole-Field Fluorescence Lifetime Imaging with Optical Sectioning. *J. Microsc.* **2001**, *203* (3), 246–257. https://doi.org/10.1046/j.1365-2818.2001.00894.x.
(102) Redford, G. I.; Clegg, R. M. Polar Plot Representation for Frequency-Domain Analysis of Fluorescence Lifetimes. *J. Fluoresc.* **2005**, *15* (5), 805. https://doi.org/10.1007/s10895-005-2990-8.
(103) Tsurui, H.; Nishimura, H.; Hattori, S.; Hirose, S.; Okumura, K.; Shirai, T. Seven-Color Fluorescence Imaging of Tissue Samples Based on Fourier Spectroscopy and Singular Value Decomposition. *J. Histochem. Cytochem.* **2000**, *48* (5), 653–662. https://doi.org/10.1177/002215540004800509.
(104) Martin, M. E.; Wabuyele, M. B.; Chen, K.; Kasili, P.; Panjehpour, M.; Phan, M.; Overholt, B.; Cunningham, G.; Wilson, D.; DeNovo, R. C.; Vo-Dinh, T.

Development of an Advanced Hyperspectral Imaging (HSI) System with Applications for Cancer Detection. *Ann. Biomed. Eng.* **2006**, *34* (6), 1061–1068. https://doi.org/10.1007/s10439-006-9121-9.
(105) Akbari, H.; Halig, L.; Schuster, D. M.; Fei, B.; Osunkoya, A.; Master, V.; Nieh, P.; Chen, G. Hyperspectral Imaging and Quantitative Analysis for Prostate Cancer Detection. *J. Biomed. Opt.* **2012**, *17* (7), 1–11.
(106) Haraguchi, T.; Shimi, T.; Koujin, T.; Hashiguchi, N.; Hiraoka, Y. Spectral Imaging Fluorescence Microscopy. *Genes Cells* **2002**, *7* (9), 881–887. https://doi.org/10.1046/j.1365-2443.2002.00575.x.
(107) Cohen, S.; Valm, A. M.; Lippincott-Schwartz, J. Multispectral Live-Cell Imaging. *Curr. Protoc. Cell Biol.* **2018**, *79* (1), e46. https://doi.org/10.1002/cpcb.46.
(108) Neher, R.; Neher, E. Optimizing Imaging Parameters for the Separation of Multiple Labels in a Fluorescence Image. *J. Microsc.* **2004**, *213* (1), 46–62. https://doi.org/10.1111/j.1365-2818.2004.01262.x.
(109) Pareja, F.; Brandes, A. H.; Basili, T.; Selenica, P.; Geyer, F. C.; Fan, D.; Da Cruz Paula, A.; Kumar, R.; Brown, D. N.; Gularte-Mérida, R.; Alemar, B.; Bi, R.; Lim, R. S.; de Bruijn, I.; Fujisawa, S.; Gardner, R.; Feng, E.; Li, A.; da Silva, E. M.; Lozada, J. R.; Blecua, P.; Cohen-Gould, L.; Jungbluth, A. A.; Rakha, E. A.; Ellis, I. O.; Edelweiss, M. I. A.; Palazzo, J.; Norton, L.; Hollmann, T.; Edelweiss, M.; Rubin, B. P.; Weigelt, B.; Reis-Filho, J. S. Loss-of-Function Mutations in ATP6AP1 and ATP6AP2 in Granular Cell Tumors. *Nat. Commun.* **2018**, *9* (1), 3533. https://doi.org/10.1038/s41467-018-05886-y.
(110) Holzapfel, H. Y.; Stern, A. D.; Bouhaddou, M.; Anglin, C. M.; Putur, D.; Comer, S.; Birtwistle, M. R. Fluorescence Multiplexing with Spectral Imaging and Combinatorics. *ACS Comb. Sci.* **2018**, *20* (11), 653–659. https://doi.org/10.1021/acscombsci.8b00101.
(111) Niehörster, T.; Löschberger, A.; Gregor, I.; Krämer, B.; Rahn, H.-J.; Patting, M.; Koberling, F.; Enderlein, J.; Sauer, M. Multi-Target Spectrally Resolved Fluorescence Lifetime Imaging Microscopy. *Nat. Methods* **2016**, *13*, 257.
(112) Angelo, M.; Bendall, S. C.; Finck, R.; Hale, M. B.; Hitzman, C.; Borowsky, A. D.; Levenson, R. M.; Lowe, J. B.; Liu, S. D.; Natkunam, Y.; Nolan, G. P. Multiplexed Ion Beam Imaing (MIBI) of Human Breast Tumors. *Nat. Med.* **2014**, *20* (4), 436–442. https://doi.org/10.1038/nm.3488.Multiplexed.
(113) Giesen, C.; Wang, H. A. O.; Schapiro, D.; Zivanovic, N.; Jacobs, A.; Hattendorf, B.; Schüffler, P. J.; Grolimund, D.; Buhmann, J. M.; Brandt, S.; Varga, Z.; Wild, P. J.; Günther, D.; Bodenmiller, B. Highly Multiplexed Imaging of Tumor Tissues with Subcellular Resolution by Mass Cytometry. *Nat. Methods* **2014**, *11* (4), 417–422. https://doi.org/10.1038/nmeth.2869.
(114) Bendall, S. C.; Simonds, E. F.; Qiu, P.; Amir, E. D.; Krutzik, P. O.; Finck, R.; Bruggner, R. V; Melamed, R.; Trejo, A.; Ornatsky, O. I.; Balderas, R. S.; Plevritis, S. K.; Sachs, K.; Pe\textquoterighter, D.; Tanner, S. D.; Nolan, G. P. Single-Cell Mass Cytometry of Differential Immune and Drug Responses

Across a Human Hematopoietic Continuum. *Science* **2011**, *332* (6030), 687–696. https://doi.org/10.1126/science.1198704.
(115) Bodenmiller, B. Multiplexed Epitope-Based Tissue Imaging for Discovery and Healthcare Applications. *Cell Syst.* **2016**, *2* (4), 225–238. https://doi.org/10.1016/j.cels.2016.03.008.
(116) Carvajal-Hausdorf, D. E.; Patsenker, J.; Stanton, K. P.; Villarroel-Espindola, F.; Esch, A.; Montgomery, R. R.; Psyrri, A.; Kalogeras, K. T.; Kotoula, V.; Foutzilas, G.; Schalper, K. A.; Kluger, Y.; Rimm, D. L. Multiplexed Measurement of Signaling Targets and Cytotoxic T Cells in Trastuzumab-Treated Patients Using Imaging Mass Cytometry. *Clin. Cancer Res.* **2019**, No. 203, clincanres.2599.2018. https://doi.org/10.1158/1078-0432.CCR-18-2599.
(117) Spitzer, M. H.; Nolan, G. P. Mass Cytometry: Single Cells, Many Features. *Cell* **2016**, *165* (4), 780–791. https://doi.org/10.1016/j.cell.2016.04.019.
(118) Rodriques, S. G.; Stickels, R. R.; Goeva, A.; Martin, C. A.; Murray, E.; Vanderburg, C. R.; Welch, J.; Chen, L. M.; Chen, F.; Macosko, E. Z. Slide-Seq: A Scalable Technology for Measuring Genome-Wide Expression at High Spatial Resolution. *Science* **2019**, *363* (6434), 1463–1467. https://doi.org/10.1126/science.aaw1219.
(119) Amir, el-ad david; Davis, kara l; Tadmor, M. d; Simonds, E. F.; Levine, J. H.; Bendall, S. C.; Shenfeld, D. K.; Krishnaswamy, S.; Nolan, G. P.; Pe'er, D. ViSNE Enables Visualization of High Dimensional Single-Cell Data and Reveals Phenotypic Heterogeneity of Leukemia. *Nat. Biotechnol.* **2013**, *31* (6), 545–552. https://doi.org/10.1038/nbt.2594.
(120) Schapiro, D.; Jackson, H. W.; Raghuraman, S.; Fischer, J. R.; Vito, R.; Zanotelli, T.; Schulz, D.; Giesen, C.; Catena, R.; Varga, Z. Europe PMC Funders Group MiCAT : A Toolbox for Analysis of Cell Phenotypes and Interactions in Multiplex Image Cytometry Data. **2018**, *14* (9), 873–876. https://doi.org/10.1038/nmeth.4391.miCAT.
(121) Schapiro, D.; Jackson, H. W.; Raghuraman, S.; Fischer, J. R.; Zanotelli, V. R. T.; Schulz, D.; Giesen, C.; Catena, R.; Varga, Z.; Bodenmiller, B. HistoCAT: Analysis of Cell Phenotypes and Interactions in Multiplex Image Cytometry Data. *Nat. Methods* **2017**, *14* (9), 873–876. https://doi.org/10.1038/nmeth.4391.
(122) Laurens van der Maaten; Hinton, G. Visualizing Data Using T-SNE Laurens. *J. Mach. Learn. Res.* **2008**, *9*, 2579–2605. https://doi.org/10.1007/s10479-011-0841-3.
(123) Allan, C.; Burel, J.-M.; Moore, J.; Blackburn, C.; Linkert, M.; Loynton, S.; Macdonald, D.; Moore, W. J.; Neves, C.; Patterson, A.; Porter, M.; Tarkowska, A.; Loranger, B.; Avondo, J.; Lagerstedt, I.; Lianas, L.; Leo, S.; Hands, K.; Hay, R. T.; Patwardhan, A.; Best, C.; Kleywegt, G. J.; Zanetti, G.; Swedlow, J. R. OMERO: Flexible, Model-Driven Data Management for Experimental Biology. *Nat. Methods* **2012**, *9* (3), 245–253. https://doi.org/10.1038/nmeth.1896.

(124) Al-Rasheed, N. M.; Attia, H. A.; Mohamad, R. A.; Al-Rasheed, N. M.; Al-Amin, M. A.; AL-Onazi, A. Aqueous Date Flesh or Pits Extract Attenuates Liver Fibrosis via Suppression of Hepatic Stellate Cell Activation and Reduction of Inflammatory Cytokines, Transforming Growth Factor- β 1 and Angiogenic Markers in Carbon Tetrachloride-Intoxicated Rats. *Evid. Based Complement. Alternat. Med.* **2015**, *2015*, 1–19. https://doi.org/10.1155/2015/247357.
(125) Zimmermann, T. Spectral Imaging and Linear Unmixing in Light Microscopy. In *Microscopy Techniques: -/-*; Rietdorf, J., Ed.; Springer Berlin Heidelberg: Berlin, Heidelberg, 2005; pp 245–265. https://doi.org/10.1007/b102216.
(126) Paolo P. Provenzano; Curtis T. Rueden; Steven M. Trier; Long Yan; Suzanne M. Ponik; David R. Inman; Patricia J. Keely; Kevin W. Eliceiri. Nonlinear Optical Imaging and Spectral-Lifetime Computational Analysis of Endogenous and Exogenous Fluorophores in Breast Cancer. *J. Biomed. Opt.* **2008**, *13* (3), 1–11. https://doi.org/10.1117/1.2940365.
(127) Tsurui, H.; Nishimura, H.; Hattori, S.; Hirose, S.; Okumura, K.; Shirai, T. Seven-Color Fluorescence Imaging of Tissue Samples Based on Fourier Spectroscopy and Singular Value Decomposition. *J. Histochem. Cytochem.* **2000**, *48* (5), 653–662. https://doi.org/10.1177/002215540004800509.
(128) Chenying Yang; Vivian W. Hou; Leonard Y. Nelson; Eric J. Seibel. Mitigating Fluorescence Spectral Overlap in Wide-Field Endoscopic Imaging. *J. Biomed. Opt.* **2013**, *18* (8), 1–14. https://doi.org/10.1117/1.JBO.18.8.086012.
(129) Graf, J. F.; Zavodszky, M. I. Characterizing the Heterogeneity of Tumor Tissues from Spatially Resolved Molecular Measures. *PLoS ONE* **2017**, *12* (11), 1–20. https://doi.org/10.1371/journal.pone.0188878.
(130) Alizadeh, A. A.; Aranda, V.; Bardelli, A.; Blanpain, C.; Bock, C.; Borowski, C.; Caldas, C.; Califano, A.; Doherty, M.; Elsner, M.; Esteller, M.; Fitzgerald, R.; Korbel, J. O.; Lichter, P.; Mason, C. E.; Navin, N.; Pe'er, D.; Polyak, K.; Roberts, C. W. M.; Siu, L.; Snyder, A.; Stower, H.; Swanton, C.; Verhaak, R. G. W.; Zenklusen, J. C.; Zuber, J.; Zucman-Rossi, J. Toward Understanding and Exploiting Tumor Heterogeneity. *Nat. Med.* **2015**, *21*, 846–846.
(131) O'Connor, J. P. B.; Rose, C. J.; Waterton, J. C.; Carano, R. A. D.; Parker, G. J. M.; Jackson, A. Imaging Intratumor Heterogeneity: Role in Therapy Response, Resistance, and Clinical Outcome. *Clin. Cancer Res.* **2015**, *21* (2), 249–257. https://doi.org/10.1158/1078-0432.CCR-14-0990.
(132) Sottoriva, A.; Spiteri, I.; Piccirillo, S. G. M.; Touloumis, A.; Collins, V. P.; Marioni, J. C.; Curtis, C.; Watts, C.; Tavaré, S. Intratumor Heterogeneity in Human Glioblastoma Reflects Cancer Evolutionary Dynamics. *Proc. Natl. Acad. Sci. U. S. A.* **2013**, *110* (10), 4009–4014. https://doi.org/10.1073/pnas.1219747110.

(133) Gerlinger, M.; Rowan, A. J.; Horswell, S.; Math, M.; Larkin, J.; Endesfelder, D.; Gronroos, E.; Martinez, P.; Matthews, N.; Stewart, A.; Tarpey, P.; Varela, I.; Phillimore, B.; Begum, S.; McDonald, N. Q.; Butler, A.; Jones, D.; Raine, K.; Latimer, C.; Santos, C. R.; Nohadani, M.; Eklund, A. C.; Spencer-Dene, B.; Clark, G.; Pickering, L.; Stamp, G.; Gore, M.; Szallasi, Z.; Downward, J.; Futreal, P. A.; Swanton, C. Intratumor Heterogeneity and Branched Evolution Revealed by Multiregion Sequencing. *N. Engl. J. Med.* **2012**, *366* (10), 883–892. https://doi.org/10.1056/NEJMoa1113205.
(134) Landau, D. A.; Carter, S. L.; Stojanov, P.; McKenna, A.; Stevenson, K.; Lawrence, M. S.; Sougnez, C.; Stewart, C.; Sivachenko, A.; Wang, L.; Wan, Y.; Zhang, W.; Shukla, S. A.; Vartanov, A.; Fernandes, S. M.; Saksena, G.; Cibulskis, K.; Tesar, B.; Gabriel, S.; Hacohen, N.; Meyerson, M.; Lander, E. S.; Neuberg, D.; Brown, J. R.; Getz, G.; Wu, C. J. Evolution and Impact of Subclonal Mutations in Chronic Lymphocytic Leukemia. *Cell* **2013**, *152* (4), 714–726. https://doi.org/10.1016/j.cell.2013.01.019.
(135) Esposito, A.; Criscitiello, C.; Locatelli, M.; Milano, M.; Curigliano, G. Liquid Biopsies for Solid Tumors: Understanding Tumor Heterogeneity and Real Time Monitoring of Early Resistance to Targeted Therapies. *Pharmacol. Ther.* **2016**, *157*, 120–124. https://doi.org/10.1016/j.pharmthera.2015.11.007.
(136) Meldrum, C.; Doyle, M. A.; Tothill, R. W. Next-Generation Sequencing for Cancer Diagnostics: A Practical Perspective. *Clin. Biochem. Rev.* **2011**, *32* (4), 177–195.
(137) Bagger, F. O.; Probst, V. Single Cell Sequencing in Cancer Diagnostics. In *Single-cell Sequencing and Methylation: Methods and Clinical Applications*; Yu, B., Zhang, J., Zeng, Y., Li, L., Wang, X., Eds.; Springer Singapore: Singapore, 2020; pp 175–193. https://doi.org/10.1007/978-981-15-4494-1_15.
(138) Müllauer, L. Next Generation Sequencing: Clinical Applications in Solid Tumours. *Memo - Mag. Eur. Med. Oncol.* **2017**, *10* (4), 244–247. https://doi.org/10.1007/s12254-017-0361-1.
(139) Alemany, A.; Florescu, M.; Baron, C. S.; Peterson-Maduro, J.; van Oudenaarden, A. Whole-Organism Clone Tracing Using Single-Cell Sequencing. *Nature* **2018**, *556* (7699), 108–112. https://doi.org/10.1038/nature25969.
(140) Wen, W.; Su, W.; Tang, H.; Le, W.; Zhang, X.; Zheng, Y.; Liu, X.; Xie, L.; Li, J.; Ye, J.; Dong, L.; Cui, X.; Miao, Y.; Wang, D.; Dong, J.; Xiao, C.; Chen, W.; Wang, H. Immune Cell Profiling of COVID-19 Patients in the Recovery Stageby Single-Cell Sequencing. *Cell Discov.* **2020**, *6* (1), 31. https://doi.org/10.1038/s41421-020-0168-9.
(141) Gomes, T.; Teichmann, S. A.; Talavera-López, C. Immunology Driven by Large-Scale Single-Cell Sequencing. *Trends Immunol.* **2019**, *40* (11), 1011–1021. https://doi.org/10.1016/j.it.2019.09.004.

(142) Mader, S.; Pantel, K. Liquid Biopsy: Current Status and Future Perspectives. *Oncol. Res. Treat.* **2017**, *40* (7–8), 404–408. https://doi.org/10.1159/000478018.
(143) Chen, M.; Zhao, H. Next-Generation Sequencing in Liquid Biopsy: Cancer Screening and Early Detection. *Hum. Genomics* **2019**, *13* (1), 34. https://doi.org/10.1186/s40246-019-0220-8.
(144) Iwahashi, N.; Sakai, K.; Noguchi, T.; Yahata, T.; Matsukawa, H.; Toujima, S.; Nishio, K.; Ino, K. Liquid Biopsy-Based Comprehensive Gene Mutation Profiling for Gynecological Cancer Using CAncer Personalized Profiling by Deep Sequencing. *Sci. Rep.* **2019**, *9* (1), 10426. https://doi.org/10.1038/s41598-019-47030-w.
(145) Eng, C.-H. L.; Lawson, M.; Zhu, Q.; Dries, R.; Koulena, N.; Takei, Y.; Yun, J.; Cronin, C.; Karp, C.; Yuan, G.-C.; Cai, L. Transcriptome-Scale Super-Resolved Imaging in Tissues by RNA SeqFISH+. *Nature* **2019**, *568* (7751), 235–239. https://doi.org/10.1038/s41586-019-1049-y.
(146) Rodriques, S. G.; Stickels, R. R.; Goeva, A.; Martin, C. A.; Murray, E.; Vanderburg, C. R.; Welch, J.; Chen, L. M.; Chen, F.; Macosko, E. Z. Slide-Seq: A Scalable Technology for Measuring Genome-Wide Expression at High Spatial Resolution. *Science* **2019**, *363* (6434), 1463–1467. https://doi.org/10.1126/science.aaw1219.
(147) Gerdes, M. J.; Sevinsky, C. J.; Sood, A.; Adak, S.; Bello, M. O.; Bordwell, A.; Can, A.; Corwin, A.; Dinn, S.; Filkins, R. J.; Hollman, D.; Kamath, V.; Kaanumalle, S.; Kenny, K.; Larsen, M.; Lazare, M.; Li, Q.; Lowes, C.; McCulloch, C. C.; McDonough, E.; Montalto, M. C.; Pang, Z.; Rittscher, J.; Santamaria-Pang, A.; Sarachan, B. D.; Seel, M. L.; Seppo, A.; Shaikh, K.; Sui, Y.; Zhang, J.; Ginty, F. Highly Multiplexed Single-Cell Analysis of Formalin-Fixed, Paraffin-Embedded Cancer Tissue. *Proc. Natl. Acad. Sci.* **2013**, *110* (29), 11982–11987. https://doi.org/10.1073/pnas.1300136110.
(148) Gut, G.; Herrmann, M. D.; Pelkmans, L. Multiplexed Protein Maps Link Subcellular Organization to Cellular States. *Science* **2018**, *361* (6401), eaar7042–eaar7042. https://doi.org/10.1126/science.aar7042.
(149) Lin, J. R.; Fallahi-Sichani, M.; Chen, J. Y.; Sorger, P. K. Cyclic Immunofluorescence (CycIF), A Highly Multiplexed Method for Single-Cell Imaging. *Curr. Protoc. Chem. Biol.* **2016**, *8* (4), 251–264. https://doi.org/10.1002/cpch.14.
(150) Goltsev, Y.; Samusik, N.; Kennedy-Darling, J.; Bhate, S.; Hale, M.; Vazquez, G.; Black, S.; Nolan, G. P. Deep Profiling of Mouse Splenic Architecture with CODEX Multiplexed Imaging. *Cell* **2018**, *174* (4), 968-981.e15. https://doi.org/10.1016/j.cell.2018.07.010.
(151) Lin, J. R.; Izar, B.; Wang, S.; Yapp, C.; Mei, S.; Shah, P. M.; Santagata, S.; Sorger, P. K. Highly Multiplexed Immunofluorescence Imaging of Human Tissues and Tumors Using T-CyCIF and Conventional Optical Microscopes. *eLife* **2018**, *7*, 1–46. https://doi.org/10.7554/eLife.31657.

(152) Giesen, C.; Wang, H. A. O.; Schapiro, D.; Zivanovic, N.; Jacobs, A.; Hattendorf, B.; Schüffler, P. J.; Grolimund, D.; Buhmann, J. M.; Brandt, S.; Varga, Z.; Wild, P. J.; Günther, D.; Bodenmiller, B. Highly Multiplexed Imaging of Tumor Tissues with Subcellular Resolution by Mass Cytometry. *Nat. Methods* **2014**, *11* (4), 417–422. https://doi.org/10.1038/nmeth.2869.
(153) Angelo, M.; Bendall, S. C.; Finck, R.; Hale, M. B.; Hitzman, C.; Borowsky, A. D.; Levenson, R. M.; Lowe, J. B.; Liu, S. D.; Natkunam, Y.; Nolan, G. P. Multiplexed Ion Beam Imaing (MIBI) of Human Breast Tumors. *Nat. Med.* **2014**, *20* (4), 436–442. https://doi.org/10.1038/nm.3488.Multiplexed.
(154) Haraguchi, T.; Shimi, T.; Koujin, T.; Hashiguchi, N.; Hiraoka, Y. Spectral Imaging Fluorescence Microscopy. *Genes Cells* **2002**, *7* (9), 881–887. https://doi.org/10.1046/j.1365-2443.2002.00575.x.
(155) Lu, G.; Fei, B. Medical Hyperspectral Imaging: A Review. *J. Biomed. Opt.* **2014**, *19* (1), 010901–010901. https://doi.org/10.1117/1.jbo.19.1.010901.
(156) Martin, M. E.; Wabuyele, M. B.; Chen, K.; Kasili, P.; Panjehpour, M.; Phan, M.; Overholt, B.; Cunningham, G.; Wilson, D.; DeNovo, R. C.; Vo-Dinh, T. Development of an Advanced Hyperspectral Imaging (HSI) System with Applications for Cancer Detection. *Ann. Biomed. Eng.* **2006**, *34* (6), 1061–1068. https://doi.org/10.1007/s10439-006-9121-9.
(157) Akbari, H.; Halig, L.; Schuster, D. M.; Fei, B.; Osunkoya, A.; Master, V.; Nieh, P.; Chen, G. Hyperspectral Imaging and Quantitative Analysis for Prostate Cancer Detection. *J. Biomed. Opt.* **2012**, *17* (7), 1–11.
(158) Valm, A. M.; Mark Welch, J. L.; Borisy, G. G. CLASI-FISH: Principles of Combinatorial Labeling and Spectral Imaging. *Spec. Issue Fluoresc. Situ Hybrid. FISH* **2012**, *35* (8), 496–502. https://doi.org/10.1016/j.syapm.2012.03.004.
(159) Niehörster, T.; Löschberger, A.; Gregor, I.; Krämer, B.; Rahn, H.-J.; Patting, M.; Koberling, F.; Enderlein, J.; Sauer, M. Multi-Target Spectrally Resolved Fluorescence Lifetime Imaging Microscopy. *Nat. Methods* **2016**, *13*, 257–257.
(160) Holzapfel, H. Y.; Birtwistle, M. R. Creating Complex Fluorophore Spectra on Antibodies Through Combinatorial Labeling. *Transl. Sci.* **2016**, *2* (3), e03.
(161) Gong, H.; Holcomb, I.; Ooi, A.; Wang, X.; Majonis, D.; Unger, M. A.; Ramakrishnan, R. Simple Method To Prepare Oligonucleotide-Conjugated Antibodies and Its Application in Multiplex Protein Detection in Single Cells. *Bioconjug. Chem.* **2016**, *27* (1), 217–225. https://doi.org/10.1021/acs.bioconjchem.5b00613.
(162) Varn, F. S.; Tafe, L. J.; Amos, C. I.; Cheng, C. Computational Immune Profiling in Lung Adenocarcinoma Reveals Reproducible Prognostic Associations with Implications for Immunotherapy. *OncoImmunology* **2018**, *7* (6), e1431084. https://doi.org/10.1080/2162402X.2018.1431084.
(163) Goswami, S.; Walle, T.; Cornish, A. E.; Basu, S.; Anandhan, S.; Fernandez, I.; Vence, L.; Blando, J.; Zhao, H.; Yadav, S. S.; Ott, M.; Kong,

L. Y.; Heimberger, A. B.; de Groot, J.; Sepesi, B.; Overman, M.; Kopetz, S.; Allison, J. P.; Pe'er, D.; Sharma, P. Immune Profiling of Human Tumors Identifies CD73 as a Combinatorial Target in Glioblastoma. *Nat. Med.* **2020**, *26* (1), 39–46. https://doi.org/10.1038/s41591-019-0694-x.

(164) Trindade, C. J.; McDonough, E.; Hanson, J.; Walter Rodriguez, B.; Roper, N.; Gasmi, B.; Roque, C.; Gebregziabher, M.; Ylaya, K.; Fetsch, P.; Abdul Sater, H.; GINTY, F.; Hewitt, S. M.; Thomas, A. Utilization of Novel Highly Multiplexed Immunofluorescence Microscopy Technology to Understand Immunological Tumor Microenvironments in Small Cell Lung Carcinoma Patients Receiving Combination PD-L1 and PARP Inhibition Therapy. *J. Clin. Oncol.* **2019**, *37* (15_suppl), e14289–e14289. https://doi.org/10.1200/JCO.2019.37.15_suppl.e14289.

(165) Yu, K.; Liu, Y.; Yin, J.; Bao, J. A Novel Angle-Tuned Thin Film Filter with Low Angle Sensitivity. *Opt. Laser Technol.* **2015**, *68*, 141–145. https://doi.org/10.1016/j.optlastec.2014.11.022.

(166) Daud, A. I.; Loo, K.; Pauli, M. L.; Sanchez-Rodriguez, R.; Sandoval, P. M.; Taravati, K.; Tsai, K.; Nosrati, A.; Nardo, L.; Alvarado, M. D.; Algazi, A. P.; Pampaloni, M. H.; Lobach, I. V.; Hwang, J.; Pierce, R. H.; Gratz, I. K.; Krummel, M. F.; Rosenblum, M. D. Tumor Immune Profiling Predicts Response to Anti–PD-1 Therapy in Human Melanoma. *J. Clin. Invest.* **2016**, *126* (9), 3447–3452. https://doi.org/10.1172/JCI87324.

(167) Koutsakos, M.; Sekiya, T.; Chua, B. Y.; Nguyen, T. H. O.; Wheatley, A. K.; Juno, J. A.; Ohno, M.; Nomura, N.; Ohara, Y.; Nishimura, T.; Endo, M.; Suzuki, S.; Ishigaki, H.; Nakayama, M.; Nguyen, C. T.; Itoh, Y.; Shingai, M.; Ogasawara, K.; Kino, Y.; Kent, S. J.; Jackson, D. C.; Brown, L. E.; Kida, H.; Kedzierska, K. Immune Profiling of Influenza-Specific B- and T-Cell Responses in Macaques Using Flow Cytometry-Based Assays. *Immunol. Cell Biol.* **2020**, *n/a* (n/a). https://doi.org/10.1111/imcb.12383.

(168) Vacchi, E.; Burrello, J.; Di Silvestre, D.; Burrello, A.; Bolis, S.; Mauri, P.; Vassalli, G.; Cereda, C. W.; Farina, C.; Barile, L.; Kaelin-Lang, A.; Melli, G. Immune Profiling of Plasma-Derived Extracellular Vesicles Identifies Parkinson Disease. *Neurol. - Neuroimmunol. Neuroinflammation* **2020**, *7* (6), e866. https://doi.org/10.1212/NXI.0000000000000866.

(169) Landhuis, E. S Ingle-Cell Approaches to Immune Profiling. *Nature* **2018**, *557* (7706), 595—597. https://doi.org/10.1038/d41586-018-05214-w.

(170) Bengsch, B.; Ohtani, T.; Herati, R. S.; Bovenschen, N.; Chang, K.-M.; Wherry, E. J. Deep Immune Profiling by Mass Cytometry Links Human T and NK Cell Differentiation and Cytotoxic Molecule Expression Patterns. *Mass Cytom. Methods Appl.* **2018**, *453*, 3–10. https://doi.org/10.1016/j.jim.2017.03.009.

(171) Böttcher, C.; Fernández-Zapata, C.; Schlickeiser, S.; Kunkel, D.; Schulz, A. R.; Mei, H. E.; Weidinger, C.; Gieß, R. M.; Asseyer, S.; Siegmund, B.; Paul, F.; Ruprecht, K.; Priller, J. Multi-Parameter Immune Profiling of Peripheral Blood Mononuclear Cells by Multiplexed Single-Cell Mass Cytometry in

Patients with Early Multiple Sclerosis. *Sci. Rep.* **2019**, *9* (1), 19471. https://doi.org/10.1038/s41598-019-55852-x.
(172) Wang, W.; Su, B.; Pang, L.; Qiao, L.; Feng, Y.; Ouyang, Y.; Guo, X.; Shi, H.; Wei, F.; Su, X.; Yin, J.; Jin, R.; Chen, D. High-Dimensional Immune Profiling by Mass Cytometry Revealed Immunosuppression and Dysfunction of Immunity in COVID-19 Patients. *Cell. Mol. Immunol.* **2020**, *17* (6), 650–652. https://doi.org/10.1038/s41423-020-0447-2.
(173) Li, L.; Yan, S.; Lin, B.; Shi, Q.; Lu, Y. Chapter Eight - Single-Cell Proteomics for Cancer Immunotherapy. In *Advances in Cancer Research*; Broome, A.-M., Ed.; Academic Press, 2018; Vol. 139, pp 185–207. https://doi.org/10.1016/bs.acr.2018.04.006.
(174) Amann, R.; Fuchs, B. M. Single-Cell Identification in Microbial Communities by Improved Fluorescence in Situ Hybridization Techniques. *Nat. Rev. Microbiol.* **2008**, *6* (5), 339–348. https://doi.org/10.1038/nrmicro1888.
(175) Tropini, C.; Earle, K. A.; Huang, K. C.; Sonnenburg, J. L. The Gut Microbiome: Connecting Spatial Organization to Function. *Cell Host Microbe* **2017**, *21* (4), 433–442. https://doi.org/10.1016/j.chom.2017.03.010.
(176) Brandwein, M.; Steinberg, D.; Meshner, S. Microbial Biofilms and the Human Skin Microbiome. *Npj Biofilms Microbiomes* **2016**, *2* (1), 3. https://doi.org/10.1038/s41522-016-0004-z.
(177) Brummelman, J.; Haftmann, C.; Núñez, N. G.; Alvisi, G.; Mazza, E. M. C.; Becher, B.; Lugli, E. Development, Application and Computational Analysis of High-Dimensional Fluorescent Antibody Panels for Single-Cell Flow Cytometry. *Nat. Protoc.* **2019**, *14* (7), 1946–1969. https://doi.org/10.1038/s41596-019-0166-2.
(178) Niewold, P.; Ashhurst, T. M.; Smith, A. L.; King, N. J. C. Evaluating Spectral Cytometry for Immune Profiling in Viral Disease. *Cytometry A* **2020**, *97* (11), 1165–1179. https://doi.org/10.1002/cyto.a.24211.
(179) McKinnon, K. M. Flow Cytometry: An Overview. *Curr. Protoc. Immunol.* **2018**, *120* (1), 5.1.1-5.1.11. https://doi.org/10.1002/cpim.40.
(180) Jaimes, M. C.; Leipold, M.; Kraker, G.; Amir, E.; Maecker, H.; Lannigan, J. Full Spectrum Flow Cytometry and Mass Cytometry: A 32-Marker Panel Comparison. *Cytometry A* **2022**, *101* (11), 942–959. https://doi.org/10.1002/cyto.a.24565.
(181) Papalexi, E.; Satija, R. Single-Cell RNA Sequencing to Explore Immune Cell Heterogeneity. *Nat. Rev. Immunol.* **2018**, *18* (1), 35–45. https://doi.org/10.1038/nri.2017.76.
(182) Stuart, T.; Satija, R. Integrative Single-Cell Analysis. *Nat. Rev. Genet.* **2019**, *20* (5), 257–272. https://doi.org/10.1038/s41576-019-0093-7.
(183) McCarthy, M. E.; Anglin, C. M.; Peer, H. A.; Boleman, S. A.; Klaubert, S. R.; Birtwistle, M. R. Protocol for Creating Antibodies with Complex Fluorescence Spectra. *Bioconjug. Chem.* **2021**, *32* (6), 1156–1166. https://doi.org/10.1021/acs.bioconjchem.1c00220.

(184) Janols, H.; Bredberg, A.; Thuvesson, I.; Janciauskiene, S.; Grip, O.; Wullt, M. Lymphocyte and Monocyte Flow Cytometry Immunophenotyping as a Diagnostic Tool in Uncharacteristic Inflammatory Disorders. *BMC Infect. Dis.* **2010**, *10* (1), 205. https://doi.org/10.1186/1471-2334-10-205.
(185) Biotium, Inc. CF Dyes, 2020. https://biotium.com/wp-content/uploads/2013/07/CF-Dye-Brochure.pdf.
(186) Panchuk-Voloshina, N.; Haugland, R. P.; Bishop-Stewart, J.; Bhalgat, M. K.; Millard, P. J.; Mao, F.; Leung, W.-Y.; Haugland, R. P. Alexa Dyes, a Series of New Fluorescent Dyes That Yield Exceptionally Bright, Photostable Conjugates. *J. Histochem. Cytochem.* **1999**, *47* (9), 1179–1188. https://doi.org/10.1177/002215549904700910.
(187) Nazarenko, I.; Pires, R.; Lowe, B.; Obaidy, M.; Rashtchian, A. Effect of Primary and Secondary Structure of Oligodeoxyribonucleotides on the Fluorescent Properties of Conjugated Dyes. *Nucleic Acids Res.* **2002**, *30* (9), 2089–2195. https://doi.org/10.1093/nar/30.9.2089.
(188) Ermann, J.; Rao, D. A.; Teslovich, N. C.; Brenner, M. B.; Raychaudhuri, S. Immune Cell Profiling to Guide Therapeutic Decisions in Rheumatic Diseases. *Nat. Rev. Rheumatol.* **2015**, *11* (9), 541–551. https://doi.org/10.1038/nrrheum.2015.71.
(189) Ng, H. H. M.; Lee, R. Y.; Goh, S.; Tay, I. S. Y.; Lim, X.; Lee, B.; Chew, V.; Li, H.; Tan, B.; Lim, S.; Lim, J. C. T.; Au, B.; Loh, J. J. H.; Saraf, S.; Connolly, J. E.; Loh, T.; Leow, W. Q.; Lee, J. J. X.; Toh, H. C.; Malavasi, F.; Lee, S. Y.; Chow, P.; Newell, E. W.; Choo, S. P.; Tai, D.; Yeong, J.; Lim, T. K. H. Immunohistochemical Scoring of CD38 in the Tumor Microenvironment Predicts Responsiveness to Anti-PD-1/PD-L1 Immunotherapy in Hepatocellular Carcinoma. *J. Immunother. Cancer* **2020**, *8* (2), e000987. https://doi.org/10.1136/jitc-2020-000987.
(190) Andreou, C.; Weissleder, R.; Kircher, M. F. Multiplexed Imaging in Oncology. *Nat. Biomed. Eng.* **2022**, *6* (5), 527–540. https://doi.org/10.1038/s41551-022-00891-5.
(191) Wang Tim; Wei Jenny J.; Sabatini David M.; Lander Eric S. Genetic Screens in Human Cells Using the CRISPR-Cas9 System. *Science* **2014**, *343* (6166), 80–84. https://doi.org/10.1126/science.1246981.
(192) Xue, H.-Y.; Ji, L.-J.; Gao, A.-M.; Liu, P.; He, J.-D.; Lu, X.-J. CRISPR-Cas9 for Medical Genetic Screens: Applications and Future Perspectives. *J. Med. Genet.* **2016**, *53* (2), 91. https://doi.org/10.1136/jmedgenet-2015-103409.
(193) Wei, L.; Lee, D.; Law, C.-T.; Zhang, M. S.; Shen, J.; Chin, D. W.-C.; Zhang, A.; Tsang, F. H.-C.; Wong, C. L.-S.; Ng, I. O.-L.; Wong, C. C.-L.; Wong, C.-M. Genome-Wide CRISPR/Cas9 Library Screening Identified PHGDH as a Critical Driver for Sorafenib Resistance in HCC. *Nat. Commun.* **2019**, *10* (1), 4681. https://doi.org/10.1038/s41467-019-12606-7.
(194) Giaever, G.; Chu, A. M.; Ni, L.; Connelly, C.; Riles, L.; Véronneau, S.; Dow, S.; Lucau-Danila, A.; Anderson, K.; André, B.; Arkin, A. P.; Astromoff, A.; El

Bakkoury, M.; Bangham, R.; Benito, R.; Brachat, S.; Campanaro, S.; Curtiss, M.; Davis, K.; Deutschbauer, A.; Entian, K.-D.; Flaherty, P.; Foury, F.; Garfinkel, D. J.; Gerstein, M.; Gotte, D.; Güldener, U.; Hegemann, J. H.; Hempel, S.; Herman, Z.; Jaramillo, D. F.; Kelly, D. E.; Kelly, S. L.; Kötter, P.; LaBonte, D.; Lamb, D. C.; Lan, N.; Liang, H.; Liao, H.; Liu, L.; Luo, C.; Lussier, M.; Mao, R.; Menard, P.; Ooi, S. L.; Revuelta, J. L.; Roberts, C. J.; Rose, M.; Ross-Macdonald, P.; Scherens, B.; Schimmack, G.; Shafer, B.; Shoemaker, D. D.; Sookhai-Mahadeo, S.; Storms, R. K.; Strathern, J. N.; Valle, G.; Voet, M.; Volckaert, G.; Wang, C.; Ward, T. R.; Wilhelmy, J.; Winzeler, E. A.; Yang, Y.; Yen, G.; Youngman, E.; Yu, K.; Bussey, H.; Boeke, J. D.; Snyder, M.; Philippsen, P.; Davis, R. W.; Johnston, M. Functional Profiling of the Saccharomyces Cerevisiae Genome. *Nature* **2002**, *418* (6896), 387–391. https://doi.org/10.1038/nature00935.

(195) Trigos, A. S.; Pearson, R. B.; Papenfuss, A. T.; Goode, D. L. Altered Interactions between Unicellular and Multicellular Genes Drive Hallmarks of Transformation in a Diverse Range of Solid Tumors. *Proc. Natl. Acad. Sci. U. S. A.* **2017**, *114* (24), 6406–6411. https://doi.org/10.1073/pnas.1617743114.

(196) Forsburg, S. L. The Art and Design of Genetic Screens: Yeast. *Nat. Rev. Genet.* **2001**, *2* (9), 659–668. https://doi.org/10.1038/35088500.

(197) Mager, W. H.; Winderickx, J. Yeast as a Model for Medical and Medicinal Research. *Trends Pharmacol. Sci.* **2005**, *26* (5), 265–273. https://doi.org/10.1016/j.tips.2005.03.004.

(198) Chen, L.; Wang, Z.; Ghosh-Roy, A.; Hubert, T.; Yan, D.; O'Rourke, S.; Bowerman, B.; Wu, Z.; Jin, Y.; Chisholm, A. D. Axon Regeneration Pathways Identified by Systematic Genetic Screening in C. Elegans. *Neuron* **2011**, *71* (6), 1043–1057. https://doi.org/10.1016/j.neuron.2011.07.009.

(199) Urnov, F. D.; Rebar, E. J.; Holmes, M. C.; Zhang, H. S.; Gregory, P. D. Genome Editing with Engineered Zinc Finger Nucleases. *Nat. Rev. Genet.* **2010**, *11* (9), 636–646. https://doi.org/10.1038/nrg2842.

(200) Joung, J. K.; Sander, J. D. TALENs: A Widely Applicable Technology for Targeted Genome Editing. *Nat. Rev. Mol. Cell Biol.* **2013**, *14* (1), 49–55. https://doi.org/10.1038/nrm3486.

(201) Novina, C. D.; Sharp, P. A. The RNAi Revolution. *Nature* **2004**, *430* (6996), 161–164. https://doi.org/10.1038/430161a.

(202) Shalem Ophir; Sanjana Neville E.; Hartenian Ella; Shi Xi; Scott David A.; Mikkelsen Tarjei S.; Heckl Dirk; Ebert Benjamin L.; Root David E.; Doench John G.; Zhang Feng. Genome-Scale CRISPR-Cas9 Knockout Screening in Human Cells. *Science* **2014**, *343* (6166), 84–87. https://doi.org/10.1126/science.1247005.

(203) Mali Prashant; Yang Luhan; Esvelt Kevin M.; Aach John; Guell Marc; DiCarlo James E.; Norville Julie E.; Church George M. RNA-Guided

Human Genome Engineering via Cas9. *Science* **2013**, *339* (6121), 823–826. https://doi.org/10.1126/science.1232033.
(204) Schmid-Burgk, J. L. Disruptive Non-Disruptive Applications of CRISPR/Cas9. *Chem. Biotechnol. • Pharm. Biotechnol.* **2017**, *48*, 203–209. https://doi.org/10.1016/j.copbio.2017.06.001.
(205) Kampmann, M. CRISPRi and CRISPRa Screens in Mammalian Cells for Precision Biology and Medicine. *ACS Chem. Biol.* **2018**, *13* (2), 406–416. https://doi.org/10.1021/acschembio.7b00657.
(206) Baryshnikova, A.; Costanzo, M.; Kim, Y.; Ding, H.; Koh, J.; Toufighi, K.; Youn, J.-Y.; Ou, J.; San Luis, B.-J.; Bandyopadhyay, S.; Hibbs, M.; Hess, D.; Gingras, A.-C.; Bader, G. D.; Troyanskaya, O. G.; Brown, G. W.; Andrews, B.; Boone, C.; Myers, C. L. Quantitative Analysis of Fitness and Genetic Interactions in Yeast on a Genome Scale. *Nat. Methods* **2010**, *7* (12), 1017–1024. https://doi.org/10.1038/nmeth.1534.
(207) Behan, F. M.; Iorio, F.; Picco, G.; Gonçalves, E.; Beaver, C. M.; Migliardi, G.; Santos, R.; Rao, Y.; Sassi, F.; Pinnelli, M.; Ansari, R.; Harper, S.; Jackson, D. A.; McRae, R.; Pooley, R.; Wilkinson, P.; van der Meer, D.; Dow, D.; Buser-Doepner, C.; Bertotti, A.; Trusolino, L.; Stronach, E. A.; Saez-Rodriguez, J.; Yusa, K.; Garnett, M. J. Prioritization of Cancer Therapeutic Targets Using CRISPR–Cas9 Screens. *Nature* **2019**, *568* (7753), 511–516. https://doi.org/10.1038/s41586-019-1103-9.
(208) Costanzo, M.; Baryshnikova, A.; Myers, C. L.; Andrews, B.; Boone, C. Charting the Genetic Interaction Map of a Cell. *Anal. Biotechnol.* **2011**, *22* (1), 66–74. https://doi.org/10.1016/j.copbio.2010.11.001.
(209) Shen, J. P.; Zhao, D.; Sasik, R.; Luebeck, J.; Birmingham, A.; Bojorquez-Gomez, A.; Licon, K.; Klepper, K.; Pekin, D.; Beckett, A. N.; Sanchez, K. S.; Thomas, A.; Kuo, C.-C.; Du, D.; Roguev, A.; Lewis, N. E.; Chang, A. N.; Kreisberg, J. F.; Krogan, N.; Qi, L.; Ideker, T.; Mali, P. Combinatorial CRISPR–Cas9 Screens for de Novo Mapping of Genetic Interactions. *Nat. Methods* **2017**, *14* (6), 573–576. https://doi.org/10.1038/nmeth.4225.
(210) Kuzmin Elena; VanderSluis Benjamin; Wang Wen; Tan Guihong; Deshpande Raamesh; Chen Yiqun; Usaj Matej; Balint Attila; Mattiazzi Usaj Mojca; van Leeuwen Jolanda; Koch Elizabeth N.; Pons Carles; Dagilis Andrius J.; Pryszlak Michael; Wang Jason Zi Yang; Hanchard Julia; Riggi Margot; Xu Kaicong; Heydari Hamed; San Luis Bryan-Joseph; Shuteriqi Ermira; Zhu Hongwei; Van Dyk Nydia; Sharifpoor Sara; Costanzo Michael; Loewith Robbie; Caudy Amy; Bolnick Daniel; Brown Grant W.; Andrews Brenda J.; Boone Charles; Myers Chad L. Systematic Analysis of Complex Genetic Interactions. *Science* **2018**, *360* (6386), eaao1729. https://doi.org/10.1126/science.aao1729.
(211) Mani, R.; St.Onge, R. P.; Hartman, J. L.; Giaever, G.; Roth, F. P. Defining Genetic Interaction. *Proc. Natl. Acad. Sci.* **2008**, *105* (9), 3461. https://doi.org/10.1073/pnas.0712255105.

(212) Dixon, S. J.; Costanzo, M.; Baryshnikova, A.; Andrews, B.; Boone, C. Systematic Mapping of Genetic Interaction Networks. *Annu. Rev. Genet.* **2009**, *43* (1), 601–625. https://doi.org/10.1146/annurev.genet.39.073003.114751.
(213) Puddu, F.; Herzog, M.; Selivanova, A.; Wang, S.; Zhu, J.; Klein-Lavi, S.; Gordon, M.; Meirman, R.; Millan-Zambrano, G.; Ayestaran, I.; Salguero, I.; Sharan, R.; Li, R.; Kupiec, M.; Jackson, S. P. Genome Architecture and Stability in the Saccharomyces Cerevisiae Knockout Collection. *Nature* **2019**, *573* (7774), 416–420. https://doi.org/10.1038/s41586-019-1549-9.
(214) Hedges, S. B. The Origin and Evolution of Model Organisms. *Nat. Rev. Genet.* **2002**, *3* (11), 838–849. https://doi.org/10.1038/nrg929.
(215) Du, D.; Roguev, A.; Gordon, D. E.; Chen, M.; Chen, S.-H.; Shales, M.; Shen, J. P.; Ideker, T.; Mali, P.; Qi, L. S.; Krogan, N. J. Genetic Interaction Mapping in Mammalian Cells Using CRISPR Interference. *Nat. Methods* **2017**, *14* (6), 577–580. https://doi.org/10.1038/nmeth.4286.
(216) Wong, A. S. L.; Choi, G. C. G.; Cui, C. H.; Pregernig, G.; Milani, P.; Adam, M.; Perli, S. D.; Kazer, S. W.; Gaillard, A.; Hermann, M.; Shalek, A. K.; Fraenkel, E.; Lu, T. K. Multiplexed Barcoded CRISPR-Cas9 Screening Enabled by CombiGEM. *Proc. Natl. Acad. Sci.* **2016**, *113* (9), 2544. https://doi.org/10.1073/pnas.1517883113.
(217) Han, K.; Jeng, E. E.; Hess, G. T.; Morgens, D. W.; Li, A.; Bassik, M. C. Synergistic Drug Combinations for Cancer Identified in a CRISPR Screen for Pairwise Genetic Interactions. *Nat. Biotechnol.* **2017**, *35* (5), 463–474. https://doi.org/10.1038/nbt.3834.
(218) Kim, G. B.; Dutra-Clarke, M.; Levy, R.; Park, H.; Sabet, S.; Molina, J.; Akhtar, A. A.; Danielpour, M.; Breunig, J. TMOD-08. INVESTIGATING PEDIATRIC GBM USING IN VIVO SOMATIC MOUSE MOSAICS WITH LOCUS-SPECIFIC, STABLY-INTEGRATED TRANSGENIC ELEMENTS. *Neuro-Oncol.* **2017**, *19* (Suppl 4), iv50–iv50. https://doi.org/10.1093/neuonc/nox083.207.
(219) Wroblewska, A.; Dhainaut, M.; Ben-Zvi, B.; Rose, S. A.; Park, E. S.; Amir, E.-A. D.; Bektesevic, A.; Baccarini, A.; Merad, M.; Rahman, A. H.; Brown, B. D. Protein Barcodes Enable High-Dimensional Single-Cell CRISPR Screens. *Cell* **2018**, *175* (4), 1141-1155.e16. https://doi.org/10.1016/j.cell.2018.09.022.
(220) Schraivogel, D.; Gschwind, A. R.; Milbank, J. H.; Leonce, D. R.; Jakob, P.; Mathur, L.; Korbel, J. O.; Merten, C. A.; Velten, L.; Steinmetz, L. M. Targeted Perturb-Seq Enables Genome-Scale Genetic Screens in Single Cells. *Nat. Methods* **2020**, *17* (6), 629–635. https://doi.org/10.1038/s41592-020-0837-5.
(221) Dixit, A.; Parnas, O.; Li, B.; Chen, J.; Fulco, C. P.; Jerby-Arnon, L.; Marjanovic, N. D.; Dionne, D.; Burks, T.; Raychowdhury, R.; Adamson, B.; Norman, T. M.; Lander, E. S.; Weissman, J. S.; Friedman, N.; Regev, A. Perturb-Seq: Dissecting Molecular Circuits with Scalable Single-Cell RNA

Profiling of Pooled Genetic Screens. *Cell* **2016**, *167* (7), 1853-1866.e17. https://doi.org/10.1016/j.cell.2016.11.038.
(222) Ursu, O.; Neal, J. T.; Shea, E.; Thakore, P. I.; Jerby-Arnon, L.; Nguyen, L.; Dionne, D.; Diaz, C.; Bauman, J.; Mosaad, M. M.; Fagre, C.; Lo, A.; McSharry, M.; Giacomelli, A. O.; Ly, S. H.; Rozenblatt-Rosen, O.; Hahn, W. C.; Aguirre, A. J.; Berger, A. H.; Regev, A.; Boehm, J. S. Massively Parallel Phenotyping of Coding Variants in Cancer with Perturb-Seq. *Nat. Biotechnol.* **2022**, *40* (6), 896–905. https://doi.org/10.1038/s41587-021-01160-7.
(223) Kremers, G.-J.; Goedhart, J.; van Munster, E. B.; Gadella, T. W. J. Cyan and Yellow Super Fluorescent Proteins with Improved Brightness, Protein Folding, and FRET Förster Radius,. *Biochemistry* **2006**, *45* (21), 6570–6580. https://doi.org/10.1021/bi0516273.
(224) Piston, D. W.; Kremers, G.-J. Fluorescent Protein FRET: The Good, the Bad and the Ugly. *Trends Biochem. Sci.* **2007**, *32* (9), 407–414. https://doi.org/10.1016/j.tibs.2007.08.003.
(225) Vogel, S. S.; van der Meer, B. W.; Blank, P. S. Estimating the Distance Separating Fluorescent Protein FRET Pairs. *Adv. Light Microsc.* **2014**, *66* (2), 131–138. https://doi.org/10.1016/j.ymeth.2013.06.021.
(226) Basak, S.; Saikia, N.; Dougherty, L.; Guo, Z.; Wu, F.; Mindlin, F.; Lary, J. W.; Cole, J. L.; Ding, F.; Bowen, M. E. Probing Interdomain Linkers and Protein Supertertiary Structure In Vitro and in Live Cells with Fluorescent Protein Resonance Energy Transfer. *J. Mol. Biol.* **2021**, *433* (5), 166793. https://doi.org/10.1016/j.jmb.2020.166793.
(227) Day, R. N.; Booker, C. F.; Periasamy, A. Characterization of an Improved Donor Fluorescent Protein for Forster Resonance Energy Transfer Microscopy. *J. Biomed. Opt.* **2008**, *13* (3), 031203–031203. https://doi.org/10.1117/1.2939094.
(228) George Abraham, B.; Sarkisyan, K. S.; Mishin, A. S.; Santala, V.; Tkachenko, N. V.; Karp, M. Fluorescent Protein Based FRET Pairs with Improved Dynamic Range for Fluorescence Lifetime Measurements. *PloS One* **2015**, *10* (8), e0134436–e0134436. https://doi.org/10.1371/journal.pone.0134436.
(229) Bajar, B. T.; Wang, E. S.; Zhang, S.; Lin, M. Z.; Chu, J. A Guide to Fluorescent Protein FRET Pairs. *Sensors* **2016**, *16* (9), 1488. https://doi.org/10.3390/s16091488.
(230) Schwartz, A.; Wang, L.; Early, E.; Gaigalas, A.; Zhang, Y.-Z.; Marti, G. E.; Vogt, R. F. Quantitating Fluorescence Intensity from Fluorophore: The Definition of MESF Assignment. *J. Res. Natl. Inst. Stand. Technol.* **2002**, *107* (1), 83–91. https://doi.org/10.6028/jres.107.009.
(231) Boughorbel, S.; Jarray, F.; El-Anbari, M. Optimal Classifier for Imbalanced Data Using Matthews Correlation Coefficient Metric. *PloS One* **2017**, *12* (6), e0177678–e0177678. https://doi.org/10.1371/journal.pone.0177678.

(232) Norman Thomas M.; Horlbeck Max A.; Replogle Joseph M.; Ge Alex Y.; Xu Albert; Jost Marco; Gilbert Luke A.; Weissman Jonathan S. Exploring Genetic Interaction Manifolds Constructed from Rich Single-Cell Phenotypes. *Science* **2019**, *365* (6455), 786–793. https://doi.org/10.1126/science.aax4438.
(233) Gilbert Luke A. Mapping Cancer Genetics at Single-Cell Resolution. *Sci. Transl. Med.* **2020**, *12* (558), eabd3049. https://doi.org/10.1126/scitranslmed.abd3049.
(234) Liberali, P.; Snijder, B.; Pelkmans, L. Single-Cell and Multivariate Approaches in Genetic Perturbation Screens. *Nat. Rev. Genet.* **2015**, *16* (1), 18–32. https://doi.org/10.1038/nrg3768.
(235) Adamson, B.; Norman, T. M.; Jost, M.; Cho, M. Y.; Nuñez, J. K.; Chen, Y.; Villalta, J. E.; Gilbert, L. A.; Horlbeck, M. A.; Hein, M. Y.; Pak, R. A.; Gray, A. N.; Gross, C. A.; Dixit, A.; Parnas, O.; Regev, A.; Weissman, J. S. A Multiplexed Single-Cell CRISPR Screening Platform Enables Systematic Dissection of the Unfolded Protein Response. *Cell* **2016**, *167* (7), 1867-1882.e21. https://doi.org/10.1016/j.cell.2016.11.048.
(236) Jaitin, D. A.; Weiner, A.; Yofe, I.; Lara-Astiaso, D.; Keren-Shaul, H.; David, E.; Salame, T. M.; Tanay, A.; van Oudenaarden, A.; Amit, I. Dissecting Immune Circuits by Linking CRISPR-Pooled Screens with Single-Cell RNA-Seq. *Cell* **2016**, *167* (7), 1883-1896.e15. https://doi.org/10.1016/j.cell.2016.11.039.
(237) Datlinger, P.; Rendeiro, A. F.; Schmidl, C.; Krausgruber, T.; Traxler, P.; Klughammer, J.; Schuster, L. C.; Kuchler, A.; Alpar, D.; Bock, C. Pooled CRISPR Screening with Single-Cell Transcriptome Readout. *Nat. Methods* **2017**, *14* (3), 297–301. https://doi.org/10.1038/nmeth.4177.
(238) Duan, B.; Zhou, C.; Zhu, C.; Yu, Y.; Li, G.; Zhang, S.; Zhang, C.; Ye, X.; Ma, H.; Qu, S.; Zhang, Z.; Wang, P.; Sun, S.; Liu, Q. Model-Based Understanding of Single-Cell CRISPR Screening. *Nat. Commun.* **2019**, *10* (1), 2233. https://doi.org/10.1038/s41467-019-10216-x.
(239) Ziegenhain, C.; Vieth, B.; Parekh, S.; Reinius, B.; Guillaumet-Adkins, A.; Smets, M.; Leonhardt, H.; Heyn, H.; Hellmann, I.; Enard, W. Comparative Analysis of Single-Cell RNA Sequencing Methods. *Mol. Cell* **2017**, *65* (4), 631-643.e4. https://doi.org/10.1016/j.molcel.2017.01.023.
(240) McGinnis, C. S.; Patterson, D. M.; Winkler, J.; Conrad, D. N.; Hein, M. Y.; Srivastava, V.; Hu, J. L.; Murrow, L. M.; Weissman, J. S.; Werb, Z.; Chow, E. D.; Gartner, Z. J. MULTI-Seq: Sample Multiplexing for Single-Cell RNA Sequencing Using Lipid-Tagged Indices. *Nat. Methods* **2019**, *16* (7), 619–626. https://doi.org/10.1038/s41592-019-0433-8.
(241) Ashworth, A.; Lord, C. J. Synthetic Lethal Therapies for Cancer: What's next after PARP Inhibitors? *Nat. Rev. Clin. Oncol.* **2018**, *15* (9), 564–576. https://doi.org/10.1038/s41571-018-0055-6.

(242) Castells-Roca, L.; Tejero, E.; Rodríguez-Santiago, B.; Surrallés, J. CRISPR Screens in Synthetic Lethality and Combinatorial Therapies for Cancer. *Cancers* **2021**, *13* (7). https://doi.org/10.3390/cancers13071591.
(243) Komatsubara, A. T.; Matsuda, M.; Aoki, K. Quantitative Analysis of Recombination between YFP and CFP Genes of FRET Biosensors Introduced by Lentiviral or Retroviral Gene Transfer. *Sci. Rep.* **2015**, *5* (1), 13283. https://doi.org/10.1038/srep13283.
(244) Weissman, T. A.; Pan, Y. A. Brainbow: New Resources and Emerging Biological Applications for Multicolor Genetic Labeling and Analysis. *Genetics* **2015**, *199* (2), 293–306. https://doi.org/10.1534/genetics.114.172510.
(245) Szu-Hsien (Sam) Wu; Ji-Hyun Lee; and Bon-Kyoung Koo. Lineage Tracing: Computational Reconstruction Goes Beyond the Limit of Imaging. *Mol. Cells* **2019**, *42* (2), 104–112. https://doi.org/10.14348/molcells.2019.0006.
(246) He, S.; Wang, L.-H.; Liu, Y.; Li, Y.-Q.; Chen, H.-T.; Xu, J.-H.; Peng, W.; Lin, G.-W.; Wei, P.-P.; Li, B.; Xia, X.; Wang, D.; Bei, J.-X.; He, X.; Guo, Z. Single-Cell Transcriptome Profiling of an Adult Human Cell Atlas of 15 Major Organs. *Genome Biol.* **2020**, *21* (1), 294. https://doi.org/10.1186/s13059-020-02210-0.
(247) Rozenblatt-Rosen, O.; Stubbington, M. J. T.; Regev, A.; Teichmann, S. A. The Human Cell Atlas: From Vision to Reality. *Nature* **2017**, *550* (7677), 451–453. https://doi.org/10.1038/550451a.
(248) Rozenblatt-Rosen, O.; Shin, J. W.; Rood, J. E.; Hupalowska, A.; Ardlie, K.; Clatworthy, M.; Carninci, P.; Enard, W.; Greenleaf, W.; Heyn, H.; Lein, E.; Levin, J. Z.; Linnarsson, S.; Lundberg, E.; Meyer, K.; Navin, N.; Nolan, G.; Teichmann, S.; Voet, T.; Zhuang, X.; Regev, A.; Heyn, H.; Human Cell Atlas Standards and Technology Working Group. Building a High-Quality Human Cell Atlas. *Nat. Biotechnol.* **2021**, *39* (2), 149–153. https://doi.org/10.1038/s41587-020-00812-4.
(249) Gadalla, R.; Noamani, B.; MacLeod, B. L.; Dickson, R. J.; Guo, M.; Xu, W.; Lukhele, S.; Elsaesser, H. J.; Razak, A. R. A.; Hirano, N.; McGaha, T. L.; Wang, B.; Butler, M.; Guidos, C. J.; Ohashi, P. S.; Siu, L. L.; Brooks, D. G. Validation of CyTOF Against Flow Cytometry for Immunological Studies and Monitoring of Human Cancer Clinical Trials. *Front. Oncol.* **2019**, *9*.
(250) Ding, S.; Chen, X.; Shen, K. Single-Cell RNA Sequencing in Breast Cancer: Understanding Tumor Heterogeneity and Paving Roads to Individualized Therapy. *Cancer Commun.* **2020**, *40* (8), 329–344. https://doi.org/10.1002/cac2.12078.
(251) McCarthy, M. E.; Dodd, W. B.; Lu, X.; Patel, N. D.; Haskell, C. V.; Sanabria, H.; Blenner, M. A.; Birtwistle, M. R. A Theory for High-Throughput Genetic Interaction Screening. *bioRxiv* **2022**, 2022.10.05.510977. https://doi.org/10.1101/2022.10.05.510977.